Imaging Spatial Correlations of Rydberg Excitations in Cold Atom Clouds

by

Andrew D. Schwarzkopf

A dissertation submitted in partial fulfillment
of the requirements for the degree of
Doctor of Philosophy
(Physics)
in The University of Michigan
2013

Doctoral Committee:

Professor Georg A. Raithel, Chair
Professor Paul R. Berman
Associate Professor Kevin J. Kubarych
Professor Çagliyan Kurdak
Associate Professor Jennifer P. Ogilvie

Shadow image of the TIP[1], and above it an optical dipole trap.

[1] My favorite recursive acronym, standing for "tip imaging probe"; see Section 2.3.3.

ACKNOWLEDGEMENTS

Thanks to everybody who kept me going.

First, to Georg, for his encouragement, his insight, and his enthusiasm. He provided both direction and deep theoretical understanding on this project, as well as a number of key experimental breakthroughs. Without him, none of this would have been possible.

To my committee, for being supportive and for agreeing to be on my committee.

To Rachel Sapiro, for being a mentor, a friend, a confidante, and a gadfly.

To Aaron Reinhard, for laying the groundwork for so much of this thesis.

To Dave Anderson, for bouncing ideas back and forth and for being a workout buddy during the long, cold winter months.

To the other inhabitants of SB149 (and the rest of the Raithel lab) for keeping up the good spirits and making the lab a nice place to work. And to so many of them for their feedback and copy-editing, at crucial points in my grad school tenure.

To Duane in "Computing and Technology Support" (aka OCS) who spent over a month recovering data from my experiment's corrupted hard drive. "You have MILLIONS of tiny little files!!"

To my parents, for all kinds of things, but especially for their good advice.

To the rugby team, for giving me a much-needed outlet beyond the world of optics and computer programs.

To Katherine Crocker, for sharing lunch.

To the many other people who have helped me, who I can't begin to enumerate without risk of missing still others.

And to Adam Becker!

TABLE OF CONTENTS

LIST OF TABLES

Table

LIST OF FIGURES

Figure

LIST OF APPENDICES

Appendix

LIST OF ABBREVIATIONS

AOM Acousto-optic modulator

BEC Bose Einstein Condensate

CCD Charge-coupled device

EIT Electromagnetically Induced Transparency

FWHM full-width half-max

MCP Microchannel Plate

MOT Magneto-Optical Trap

ODT Optical Dipole Trap

SSFI state-selective field ionization

TIP Tip Imaging Probe

vdW van der Waals

ABSTRACT

When cold atoms are laser-excited to Rydberg states, the strong interactions between Rydberg excitations can lead to complex many-body entanglement in the system. The excitation process results in spatial correlations between excitations in the system. In most cases, Rydberg excitation positions are anticorrelated such that no two excitations are within a "blockade radius" of each other. Such systems are well-suited for studying basic many-body physics, as well as for future technological applications such as quantum computation.

This thesis describes an experimental apparatus we constructed to perform spatially-sensitive detection of Rydberg atoms. We use the apparatus to perform measurements of the Rydberg-Rydberg pair-correlation function. This results in the first direct spatial images of the Rydberg blockade effect. We measure the blockade radius for a variety of S and D Rydberg states in rubidium. We investigate the dependence of the blockade radius on laser detunings and energy level shifts induced by optical potentials due to trapping lasers. Our results have some implications for atom traps used for neutral atom quantum computation. We also present simulations results used to characterize the performance of the imaging system.

CHAPTER I

Introduction

1.1 Rydberg atoms

Rydberg atoms are atoms in highly excited electronic states, having high principal quantum number n. Rydberg atoms have played a role in atomic physics since the early days of atomic spectroscopy, when they were used to measure the Balmer lines and other spectral series [1]. More recently, Rydberg atoms have been of interest due to their exaggerated properties. Most of these properties stem from a Rydberg atom's extremely large size, approaching a micron in radius (see Table 1.1 for reference). These properties have enabled and inspired research on a rich variety of physics. A Rydberg atom's long lifetime allows the study of coherent quantum dynamics over timescales ranging from 100 ns to as long as 100 μs or 1 ms, which are easy to access experimentally. The effect of blackbody radiation on Rydberg atom lifetimes shows their extreme sensitivity to microwave photons. The combination of long lifetimes and microwave sensitivity has enabled the study of basic quantum optics phenomena, including nondestructive detection of single microwave photons in a superconducting cavity [2, 3]. Serge Haroche shared the 2012 Nobel Prize for this work. These properties also enable precision measurements of the Rydberg contant [4, 5], the most precisely known physical constant; a recent proposal has been made to improve this

Property		n-dependence	Rb (60s)
orbital radius, $\langle r \rangle$		n^2	$5399a_0 = 0.29$ μm
radiative lifetimes			
	low-ℓ	n^3	~ 250 μs at 0 K
			~ 150 μs with 300 K blackbody
	high-ℓ, m_l	n^5	~ 700 ms at 0 K
			~ 350 μs with 300 K blackbody
polarizability		n^7	~ -200 MHz/[V/cm]^2
dipole moments $\langle n(\ell \pm 1)\|er\|n\ell \rangle$		n^2	
vdW interaction strength		n^{11}/R^6	8.9 MHz at $R = 5$ μm

Table 1.1: Dependence of Rydberg atom properties on n. The properties of the $60S_{1/2}$ state are listed at right; they are quite extreme compared to typical ground state atomic properties. Lifetimes are reduced by blackbody-radiation-induced transitions, but are still quite long compared to typical nanosecond atomic decay times. For calculating the interaction strength, R is the separation distance between the two Rydberg atoms.

measurement [6, 7]. Of more direct relevance to my work, the strong polarizabilities of Rydberg states make them excellent electric field detectors (see Chapter III). Their strong interactions with other Rydberg atoms allow the study of excitation transport [8–11] (analogous in spirit to excitation transport in photosynthetic systems [12]), many-body quantum dynamics [13–15], quantum entanglement [16, 17], and potential quantum information applications.

1.2 Excitation blockade

1.2.1 Applications in quantum information

The strength of Rydberg-Rydberg interactions has led to proposals for using Rydberg atoms in quantum computation schemes [18, 19]. There are many proposed platforms for quantum computation, including trapped ions (the currently-leading technology) [20], superconducting quantum qubits [21, 22], linear quantum optics [23], quantum dots in semiconductors [24–26], and neutral atoms [27]. The reason for the interest in Rydberg atoms for quantum computation is that the atom-atom interaction can be turned on and off, in that Rydberg-Rydberg interactions have a strength $\sim 10^{12}$ greater than ground-ground interactions [28]. We can compare this with

trapped ion schemes. In both trapped ion and neutral atom schemes, a qubit is typically composed of two hyperfine ground state levels of a single ion/atom. The entanglement operation for ions typically involves coupling the two ions via exciting a vibrational mode of the ions in an ion trap. The ions are coupled to each other through their Coulomb interaction. Unfortunately, the Coulomb interaction can also couple the ions to external perturbations, leading to possible decoherence. This decoherence source exists even after the entanglement operation is over. In contrast, the coupling in a Rydberg atom computing scheme involves only temporary excitation of atoms to Rydberg states, and after the entanglement operation is over all atoms will be back in their hyperfine levels with small interaction strengths. This would, one hopes, avoid that source of decoherence during information storage.

Although not as strong as the Coulomb interactions of ions, Rydberg-Rydberg interactions are still strong enough to perform fast gate operations (~ 1 μs timescales or faster). In the Rydberg atom quantum computation proposals, the Rydberg-Rydberg interactions are key to efficiently producing entangled states, via an effect called an excitation blockade.

1.2.2 Excitation blockade

Most simply explained, in an excitation blockade the excitation of one atom prevents the excitation of its neighbors [29]. However, it is actually a many-body process that happens all at once, rather than a step-wise process as this would imply. (This will become clearer in Section 2.2.3.) The Rydberg excitation blockade is the subject of study in this thesis, so it is worth introducing in some detail here.

I begin by considering a pair of ground state atoms, at fixed positions, which are to be excited to Rydberg states. The system has energy levels denoted by the number of Rydberg atoms excited, k. (See Figure 1.1.) In the absence of interactions,

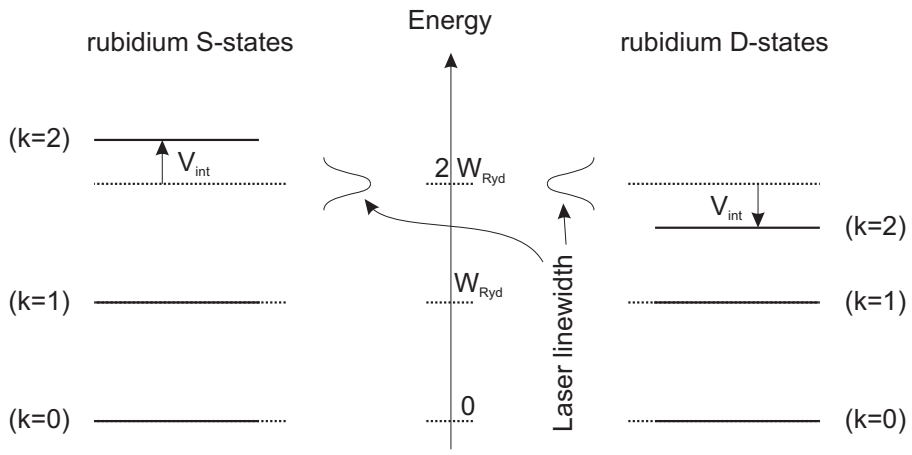

Figure 1.1: Rydberg excitation ladder for a two interacting atoms, showing zero, one, or two excitations ($k = 0, 1, 2$). The energy to excite a single Rydberg is W_{Ryd}. Dotted lines indicate energy levels without interactions. Solid lines are energy levels accounting for interactions. The energy shift of the second excited states are caused by van der Waals interactions, which in Rb have opposite sign for S and D states. If the energy shift is more than the laser linewidth, the $k = 2$ level cannot be excited.

these levels are evenly spaced by the energy required to excite one Rydberg atom. However, interactions cause energy level shifts due to the interaction energy, of order 10's of MHz for an atom-atom spacing of a few μm (see Table 1.1). If one resonantly excites the $(k = 0) \rightarrow (k = 1)$ transition of the system with a narrow bandwidth laser (of order 1 MHz or less), the laser will be out of resonance with all further steps on the energy ladder. Thus, only one Rydberg atom will be produced.

This blockade effect has a range, however. As noted, the interaction strength of Rydberg atoms depends on their separation distance. With sufficiently large separation, the energy level shift is small enough to be within the laser bandwidth. Thus, another Rydberg atom can be excited outside the "blockade radius" of the first.

This excitation process creates entanglement between atoms within a "blockade radius" because it involves a coherent interaction among the atoms where the state of one atom depends on the state of the other. The ability to entangle atoms at large physical separation (> 1 μm, based on the blockade radius) is a primary reason for the interest in this entanglement scheme. If the atoms are used for qubits, this

separation allows individual qubit addressability, e.g. by focused laser beams.

1.2.3 Experimental work toward neutral atom quantum information

Urban et al. [30] and Gaetan et al. [31] have shown the excitation blockade to be effective between atoms in spatially-separated optical traps. Each group used a pair of dipole traps separated by 5 to 10 microns, with one atom in each trap. Since then, these groups have demonstrated entanglement of atoms in such spatially-separated traps [16, 17]. This is a significant step toward the implementation of a quantum computation architecture using neutral atoms [28, 32].

The implementation of quantum gates is one important aspect of quantum computation. Another piece is the ability to couple the information out to photons for long-distance quantum-information transfer. Rydberg atom systems can also be used for this purpose, again using the Rydberg blockade as part of the key enabling physics. Saffman and Walker [33] have proposed a single-photon source with controllable emission direction, using four-wave mixing in a blockaded system. Dudin and Kuzmich [34] have implemented essentially this protocol to create a single-photon source, with the output photon coupled into an optical fiber.

1.3 Thesis outline

As mentioned, a principal reason for the interest in the Rydberg blockade is the ability to entangle spatially separated qubits. At the outset of my work in 2008 there were already several experimental demonstrations of the efficacy of the blockade, but few that studied the spatial aspects of it. I will review a few of these experiments in Chapter II.

The primary objective of my experiment is to investigate the spatial characteristics of the blockade. To enable this, a method was developed to image the positions of

Rydberg atoms. I describe the apparatus and calibration in Chapter III. I present initial experiments on imaging the Rydberg blockade in Chapter IV.

After these initial experiments, I continued optimizing the performance of my imaging apparatus. In Chapter V, I present ion trajectory simulations that helped me determine the expected magnification in my imaging and what improvements could be made. The results suggest that the greatest improvement can be achieved by increasing our atom density near the ionization electrode (see Figure 3.1). Chapter VI describes the implementation of an optical dipole trap (ODT) for this purpose. I also discuss how the imaging system affects the Rydberg excitation spectrum when exciting from the ODT.

In Chapter VII, I experimentally investigate the effect of laser detuning and background potentials on the blockade. The background potential from the ODT causes spatially-dependent energy level shifts in the Rydberg excitation spectrum. This, combined with certain laser detunings, can cause enhanced probabilities to excite Rydberg atoms at particular separation distances.

In Chapter VIII, I give a summary and conclusions about my work as a whole. I discuss future work that could build off what is presented in this thesis, focusing in particular on studies that can be done with my Rydberg-imaging apparatus.

CHAPTER II

Background Theory and Experimental Methods

In this chapter I review the basics of Rydberg-Rydberg interactions which can lead to an excitation blockade, and give a more thorough introduction to the Rydberg blockade. I present theoretical predictions for the blockade which are relevant to the experiments of Chapters IV and VII. Finally, in Section 2.3 I explain our choice of experimental methods for observing the predicted effects.

2.1 Rydberg-Rydberg interaction strengths

Rydberg atoms interact with each other primarily through electrostatic potentials. To calculate this interaction energy, each can be considered as a charge distribution given by the ionic core and the Rydberg electron wavefunction.

To calculate the interaction energy of two charge distributions, one can use the multipole moments of each charge distribution. To lowest order, the interaction of two neutral charge distributions with nonzero dipole moments will be given by the dipole-dipole term:

$$V_{dd} = \frac{\mathbf{p}_1 \cdot \mathbf{p}_2 - 3(\mathbf{n} \cdot \mathbf{p}_1)(\mathbf{n} \cdot \mathbf{p}_2)}{R^3} \tag{2.1}$$

where $\mathbf{p}_1$ and $\mathbf{p}_2$ are the dipole moments, $\mathbf{R}$ is the separation vector between the dipoles, and $\mathbf{n}$ is a unit vector pointing along $\mathbf{R}$, as shown in Figure 2.1. Note the

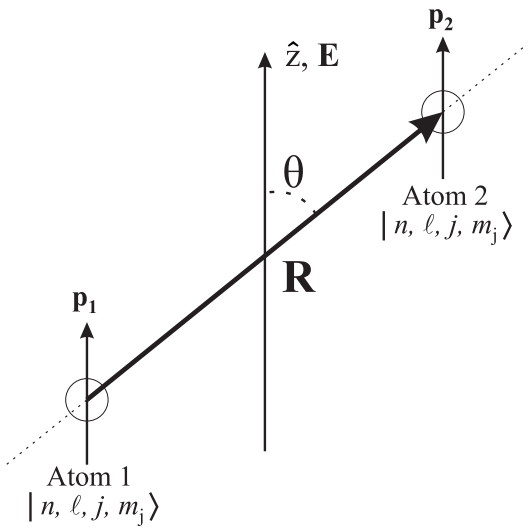

Figure 2.1: Geometry of the dipole-dipole interaction. The electric field $\mathbf{E}$ is along the $\hat{z}$ axis. The dipole moments $\mathbf{p}_1$ and $\mathbf{p}_2$ are oriented along the quantization axis defined by $\mathbf{E}$. (In the absence of an external electric field, the quantization axis $\hat{z}$ is defined by the polarization of light used to excite the Rydberg states $|n, \ell, j, m_j\rangle$.) The dipole separation vector is $\mathbf{R}$. The angle between $\mathbf{R}$ and $\hat{z}$ is θ. Reproduced with permission from [36].

above equation is given in atomic units[1].

In quantum mechanics we can take V_{dd} as an operator $\hat{V}_{dd}$, where $\mathbf{p}_1$ and $\mathbf{p}_2$ become dipole moment operators, $\hat{\mathbf{p}}_1$ and $\hat{\mathbf{p}}_2$. We can then calculate the interaction energy by perturbation theory. One generally performs laser excitation of a gas such that each atom is coupled to a Rydberg state $|A\rangle$. If there are multiple excitations in the gas, each will be in state $|A\rangle$. Multiple Rydberg atoms in state $|A\rangle$ can interact. The initial two-atom state used in the perturbative energy calculation is then $|A\rangle \otimes |A\rangle$.

2.1.1 First- and second-order shifts

The effect of V_{dd} can be evaluated in first order and higher orders. This is discussed in the following paragraphs. An electric field applied to the Rydberg atoms will change the nature of the Rydberg-Rydberg interactions, and therefore how the interactions

[1] In atomic units, the electron charge, electron mass, reduced Planck's constant ($\hbar$), and $4\pi\epsilon_0$ are set to unity. This in turn sets other units. Length is measured in units of the Bohr radius ($a_0 = \hbar^2/m_e e^2$), and energies in terms of the Hartree ($E_{hartree} = \frac{\hbar^2}{m_e a_0^2}$). See Wikipedia and also [35], but note that the latter converts between atomic units and cgs and thus neglects to mention $4\pi\epsilon_0 = 1$. I will use atomic units for the remainder of this chapter, unless otherwise noted.

are calculated from perturbation theory [36, 37].

Electric fields will usually cause the Rydberg states $|A\rangle$ to have permanent electric dipole moments. In this case, the interaction energy between the Rydberg atoms can be calculated with first-order perturbation theory:

$$\Delta W^{(1)} = \langle A| \otimes \langle A|\hat{V}_{dd}|A\rangle \otimes |A\rangle \quad . \tag{2.2}$$

If the electric field is absent or not strong enough to induce permanent electric dipole moments, the above will not be the leading term in calculating the Rydberg-Rydberg interaction. A weak electric field may still cause a first-order shift if it tunes a two-atom Rydberg state $|B\rangle \otimes |C\rangle$ to have the same energy as state $|A\rangle \otimes |A\rangle$.[2] This is called a Förster resonance. In this case we use degenerate perturbation theory with the three degenerate states $|A\rangle \otimes |A\rangle$, $|B\rangle \otimes |C\rangle$, and $|C\rangle \otimes |B\rangle$, and find

$$\Delta W^{(1)} = \pm\sqrt{2}\langle C| \otimes \langle B|\hat{V}_{dd}|A\rangle \otimes |A\rangle \tag{2.3}$$

where the $\sqrt{2}$ factor is due to the indistinguishability of $|B\rangle \otimes |C\rangle$ and $|C\rangle \otimes |B\rangle$.

If the Rydberg states have negligible permanent dipole moments and there are no electric-field induced Förster resonances, then the first-order shifts vanish and the energy shift of state $|A\rangle \otimes |A\rangle$ is calculated using second order perturbation theory:

$$\Delta W^{(2)} = -\sum_{B,C;\Delta\neq 0} \frac{|\langle C| \otimes \langle B|\hat{V}_{dd}|A\rangle \otimes |A\rangle|^2}{\Delta} \tag{2.4}$$

where Δ is the energy difference between the $|B\rangle \otimes |C\rangle$ and $|A\rangle \otimes |A\rangle$ states. This will hold for weak electric fields and zero electric field. We will see in the next section that Equation 2.4 represents a van der Waals type of interaction.

[2] Here, $|B\rangle$ and $|C\rangle$ are each also single-excitation Rydberg states, different from $|A\rangle$.

2.1.2 Scaling laws and results

We can determine the scaling laws for these interactions by using the scaling laws of Rydberg atom properties.[3] The dipole moment $\hat{\mathbf{p}}$ between nearby states scales as n^{*2}, and the energy splitting (Δ) between nearby states in zero electric field scales as n^{*-3} (due to the state energies $W = -\frac{1}{2n^{*2}}$). Therefore first-order shifts will scale as

$$\Delta W^{(1)} \propto n^{*4}/R^3 \tag{2.5}$$

and second-order shifts will scale as

$$\Delta W^{(2)} \propto n^{*11}/R^6 \quad . \tag{2.6}$$

These scalings correspond to those expected for dipole-dipole and van der Waals interactions, respectively.

Calculations of the above interaction strengths were performed by Reinhard et al. [37] (see also [36]) for rubidium. The Rydberg wavefunctions were numerically calculated to evaluate the matrix elements of $\hat{V}_{dd}$ in all of the above scenarios. I present here the results which are relevant to my own work. In the experiments presented in Chapters IV and VII, Rydberg atoms are produced by a two-step excitation from the rubidium $5S_{1/2}$ ground state to $nD_{5/2}$ and $nS_{1/2}$ states, through the intermediate $5P_{3/2}$ state. In all cases excitation is done in the absence of electric fields, so we have van der Waals interactions as given by Equation 2.4.

The interaction strengths $\Delta\tilde{W}^{(2)}$ shown in Figures 2.2 and 2.3 are scaled to remove the expected van der Waals scaling of n^{*11}/R^6:

$$\Delta\tilde{W}^{(2)} = \Delta W^{(2)} \times (R^6/n^{*11}) \tag{2.7}$$

[3] In the following discussion I use the quantity $n^* = n - \delta_\ell$, where n is the principal quantum number and δ_ℓ is the quantum defect [1]. The quantum defect accounts for the interaction of the Rydberg electron with the ionic core and depends on the angular quantum number ℓ. The interaction strengthens the binding energy of the electronic states compared to those of Hydrogen ($W = -\frac{1}{2n^2}$) and causes a phase shift of the electronic wavefunction.

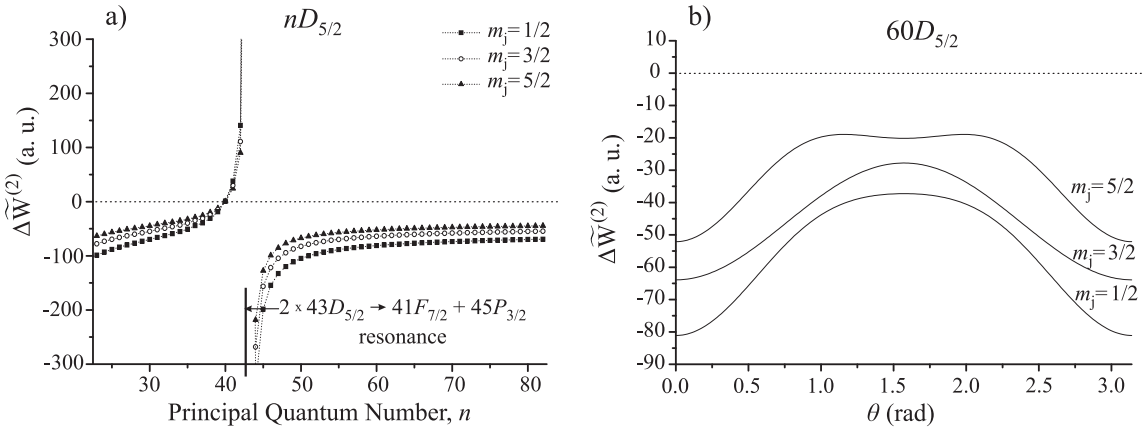

Figure 2.2: a) Scaled level shifts, $\Delta\tilde{W}^{(2)}$, of $2 \times |nD_{5/2}, m_j\rangle$ states as a function of n, for different m_j quantum numbers and $\theta = 0$. b) dependence on θ for $|60D_{5/2}, m_j\rangle$ states. Reproduced with permission from [36].

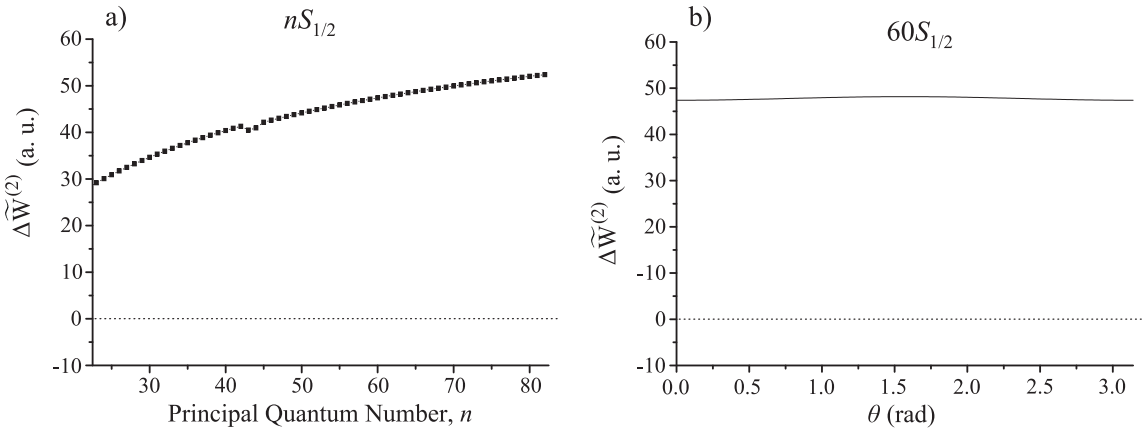

Figure 2.3: a) Scaled level shifts, $\Delta\tilde{W}^{(2)}$, of $2 \times |nS_{1/2}, m_j = 1/2\rangle$ states as a function of n, for $\theta = 0$. b) dependence on θ for $|60S_{1/2}, m_j = 1/2\rangle$. Reproduced with permission from [36].

This leaves a dependence on n^*, ℓ, j, m_j, and θ (where θ is the angle between $\mathbf{R}$ and $\hat{z}$ in Figure 2.1). The remaining variability in $\Delta\tilde{W}^{(2)}$ with n^* is largely due to changes in the energy defects Δ of Equation 2.4. This is demonstrated in Figure 2.2 for state $nD_{5/2}$. In the ranges $n \gtrsim 50$ and $n \lesssim 35$, a single interaction channel

$$2 \times nD_{5/2} \rightarrow (n-1)F_{7/2} + (n+1)P_{3/2} \tag{2.8}$$

constitutes the largest term in the sum in Equation 2.4. The energy detuning Δ is ≈ 1 GHz which limits the magnitude of the shift $\Delta\tilde{W}^{(2)}$. In the region $35 \lesssim n \lesssim 50$ a different channel

$$2 \times nD_{5/2} \rightarrow (n-2)F_{7/2} + (n+2)P_{3/2} \tag{2.9}$$

comes into near-resonance ($\Delta \approx 0$), causing a first-order shift. This causes the dispersive feature in Figure 2.2(a) near $n = 43$, as well as a positive sign of the interaction energy for a few values of n as Δ tunes through 0.

In contrast, state $nS_{1/2}$ in Figure 2.3 has four interaction channels which contribute most of the energy shift $\Delta\tilde{W}^{(2)}$. None of these channels is near resonance, for any value of n^*, and so there is no Förster resonance. The dependence of $\Delta\tilde{W}^{(2)}$ on n^* is therefore relatively mild.

For the purposes of particular experimental goals, either the $nD_{5/2}$ or $nS_{1/2}$ states may be more useful. The $nD_{5/2}$ states have the advantage of higher oscillator strength, assisting their excitation with a low-power laser in the work described in Chapter IV. They also have the advantage of tunable interaction character near $n = 43$ [38, 39]; similar physics in cesium is used by Vogt et al. [40]. For most n-values the $D_{5/2}$ states have attractive interactions, which can cause motion-induced collisions leading to ionization and plasma formation [41–43]. Of more pertinence to this thesis, the $nD_{5/2}$ interactions depend on the angle θ, which could give interesting angular-dependence to

the Rydberg blockade. In contrast, the $nS_{1/2}$ states have nearly-isotropic interactions, i.e. the interactions do not depend on θ. This would be an advantage for quantum information applications requiring angle-insensitive entanglement. The interactions are also uniformly repulsive, which can help avoid ionization due to attractive forces between atoms [42].

2.2 Excitation Blockade

The interactions described in the previous section can be used to implement a Rydberg excitation blockade, as described in Chapter I. Knowing the functional form and strength of the interactions, we can now make a more precise statement about the expected blockade radius. Equating the energy shift to the laser linewidth we have for van der Waals interactions (in SI units)

$$r_b = a_0 \times \left[\frac{E_{hartree} \times \Delta\tilde{W}^{(2)} n^{*11}}{h \times \delta\nu_L} \right]^{1/6} \tag{2.10}$$

where r_b is the blockade radius, and $\delta\nu_L$ is the laser linewidth. For state $60S_{1/2}$ and a laser linewidth of 1 MHz (typical for our experiments) we have $r_b = 7.2$ μm. See also the calculated interaction strength in Table 1.1.

In the following sections, I first introduce how the blockade effect works in mesoscopic atomic systems. I then discuss previous experiments that investigated the blockade effect, as well as the theoretical calculations that set the stage for the experiments of Chapter IV.

2.2.1 Mesoscopic systems

In Section 1.2.2 I presented the basic theory of why there is an excitation blockade, but I presented it as being a two-atom process. This may be a sufficient description for quantum information applications, if qubits are represented by single atoms. However,

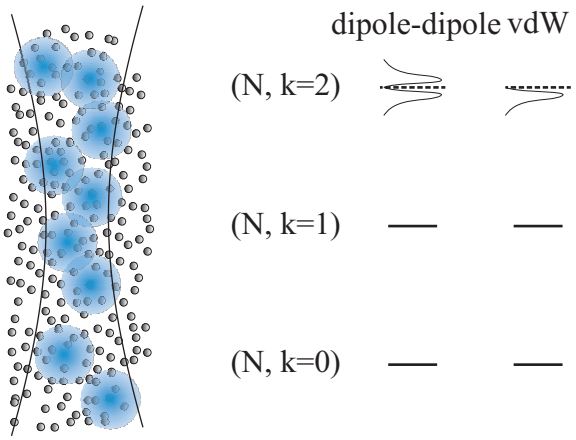

Figure 2.4: *At left*, a depiction of the "bubble" concept: there is a minimum separation between two Rydberg excitations. Only one Rydberg excitation will be found in each "bubble," depicted as a blue halo. The ground state atoms are pictured as small spheres, and a focused excitation laser as black curves. *At right*, the energy levels of the N-atom system are shown. The energy level diagrams show the energy bands that can be laser-excited for D-states, depending on the nature of the Rydberg-Rydberg interactions (van der Waals vs. dipole-dipole). (Figure inspired by [39].)

many experiments use a mesoscopic or macroscopic atomic vapor, several μm to $\sim$ 1 mm in diameter. One must theoretically describe the system as having more than just two interacting atoms.

One can write the state of an N-atom system as e.g. $|g_1, ..., r_i, ..., r_j, ..., g_N\rangle$ where most atoms are in the ground state $|g\rangle$ and some atoms (here, atoms i and j) are in the Rydberg state $|r\rangle$. We label such a state with N atoms and k excitations as a (N, k) state, similar to the notation of Figure 1.1. Note that each (N, k) label applies to a collection of states of the system. The $(N, k = 1)$ states are the N degenerate states with a single excitation. The $(N, k = 2)$ states have a basis size of $\binom{N}{2}$ and have energies which depend on the distance between the Rydberg excitations. The $(N, k = 2)$ states therefore form an energy band, as depicted on the right of Figure 2.4.

When performing laser excitation of the system, tuned to resonance with the $(N, k = 0) \rightarrow (N, k = 1)$ transition, any $k \rightarrow k + 1$ transition will be resonant unless two Rydberg atoms in the $(N, k + 1)$ state are sufficiently close to have strong interactions. The number of produced Rydberg atoms then saturates when no fur-

ther $k \rightarrow k+1$ transitions are resonant. In such a sample, each excitation will occur then some minimum distance from the others, each thus living in its own "bubble". The "bubble" concept is depicted on the left of Figure 2.4, and is commonly used to describe some of the experiments I treat in the next section.[4]

2.2.2 Previous experiments

Several initial demonstrations of the blockade effect were based on counting the number of excitations created in an atomic vapor as a function of the strength of Rydberg-Rydberg interactions [29, 40]. Rydberg-Rydberg interactions can be varied by e.g. changing the excited n state or using an electric field to tune to a Förster resonance. With increased interaction strength, the blockade radius increases and fewer excitations can fit within the fixed excitation volume. There is therefore a suppression of the number of detected excitations. We refer to this as excitation saturation. This first demonstration [29] used a laser with a bandwidth of 100 MHz, exciting several percent of the atoms in a MOT to state $70P$. Hundreds to thousands of Rydbergs were excited in a volume $\sim$ 500 μm long and $\sim$ 200 μm in diameter (FWHM).

In a considerably smaller excitation region, with fewer excited Rydberg atoms ($\sim$ 30), it is possible to measure the effect of the blockade by measuring the statistics of the number of excitations [36, 44, 45]. In the absence of Rydberg-Rydberg interactions one expects the number of excitations per laser shot to follow a Poissonian distribution. With the blockade operative one expects this distribution to narrow. Past a certain laser excitation power one consistently excites the maximum number of

[4] It should be noted that the "bubbles" are not physically real. They do not have fixed positions in the gas, and do not have hard boundaries. The "bubbles" concept is merely a convenient shorthand for the following two facts: 1) When a quantum measurement is made of the positions of the Rydberg excitations, the superposition of numerous excited many-body (N,k) states will be projected onto a particular basis state (N,k) such that there is a minimum distance between the positions of the Rydberg atoms. 2) There is a maximum number of Rydberg atoms that can be excited in a finite volume, based on the blockade radius r_b, which can be estimated by packing the volume with "bubbles" of radius r_b.

Rydberg atoms that can fit in the excitation volume, which is approximately given by the number of "bubbles" that can fit in the excitation volume. Therefore one expects a sub-poissonian distribution. This distribution has been measured by Liebisch et al. [44] as a function of Rydberg-Rydberg interaction strength. Although experimental fluctuations make the distribution super-poissonian in the absence of interactions, the statistics are indeed strongly narrowed with the onset of strong interactions [46].

Rather than counting the number of Rydberg excitations to detect the blockade, Reinhard et al. [39] have directly probed the blockade mechanism. The authors have spectroscopically investigated the interaction-induced energy level shifts described in Figure 2.4. Both the van der Waals interactions and the interactions at the $43D_{5/2}$ Förster resonance were examined. The observed energy shifts of the second excited state were in accordance with the expectations of Equations 2.3 and 2.4 .

As mentioned in Chapter I, the blockade was demonstrated to be effective between spatially-separated atoms in adjacent dipole traps [30, 31]. However, no studies have been done of the distance- and angle-dependence of the blockade effect by using direct spatial observation. This is the subject of study in this thesis.

2.2.3 Theoretical background

Here I present theory used to predict the distance- and angle- dependence of the blockade effect.

Theory for the laser excitation process that leads to the Rydberg blockade is considered by, for example, Lukin et al. [19], Robicheaux and Hernández [47], Ates et al. [48], and Hernández and Robicheaux [49].

Typically one represents the state of the system in terms of basis states that indicate whether each atom is in the ground $|g\rangle$ or Rydberg $|r\rangle$ state. The full state

of the system can then be written

$$|\Psi(t)\rangle = a_{gg...g}|gg...g\rangle \tag{2.11}$$

$$+ a_{rg...g}|rg...g\rangle + (\text{other terms with single excitation}) \tag{2.12}$$

$$+ a_{rr...g}|rr...g\rangle + (\text{other terms with double excitation}) \tag{2.13}$$

$$+ ... \tag{2.14}$$

$$+ a_{rr...r}|rr...r\rangle \tag{2.15}$$

$$= \sum_{\alpha} a_{\alpha}(t)|\alpha\rangle \tag{2.16}$$

Assuming Rydberg atoms interact with each other only through pair-wise van der Waals interactions, the Hamiltonian describing the system is (in the dressed state picture)

$$\hat{H} = \sum_{j} \hat{H}_j^{(1)} + \sum_{j<k} V_{j,k}|r_j r_k\rangle\langle r_j r_k| \tag{2.17}$$

$$\hat{H}_j^{(1)} = -\Delta\omega(t)|r_j\rangle\langle r_j| + \frac{\Omega}{2}\left(|g_j\rangle\langle r_j| + |r_j\rangle\langle g_j|\right) \tag{2.18}$$

where $\hat{H}^{(1)}$ accounts for the interaction of a single atom with the light field and $V_{j,k}$ is the interaction between two excited atoms for an atomic pair (j,k). The term $\Delta\omega$ is the laser detuning from the $|g\rangle \rightarrow |r\rangle$ transition, which could be time-dependent to account for a chirp of the laser pulse. Ω is the single-atom Rabi frequency, which includes the time-dependence of the laser pulse envelope (e.g. see Equation 2.24).

In a fully blockaded system, we expect only a single Rydberg excitation. The excitation is coherently shared among all atoms, with the fully symmetrized wavefunction

$$|\mathbf{r}^1\rangle = \frac{1}{\sqrt{N}} \sum_{i} |g...r_i...g\rangle \quad . \tag{2.19}$$

It is interesting to note that the Rabi frequency for excitation to this state is enhanced compared to the Rabi frequency for a single atom. We can see this by applying the

Hamiltonian between the ground state and $|\mathbf{r}^1\rangle$:

$$\langle \mathbf{r}^1 | \hat{H} | \mathbf{g} \rangle \tag{2.20}$$

$$= \sum_l \frac{1}{\sqrt{N}} \langle r_l | \left(\sum_j \Omega | r_j \rangle \langle g_j | \right) | \mathbf{g} \rangle \tag{2.21}$$

$$= \frac{1}{\sqrt{N}} N\Omega \tag{2.22}$$

$$= \sqrt{N}\Omega \tag{2.23}$$

Robicheaux and Hernández [47] perform simulations of the excitation process in a mesoscopic gas. The number of many-body basis states required in the simulation scales as 2^N, where N is the number of ground state atoms. This quickly becomes an intractable problem for increasing N, so several tricks are used to reduce the state space in order to simulate a mesoscopic (or infinite) atomic gas. These are based on the physics of the problem. First, they reduce an infinite system to a cubic volume, where the Rydberg-Rydberg interactions are calculated with periodic boundary conditions. The volume is chosen large enough to cover the region of Rydberg-Rydberg correlation. Second, they reduce the number of atoms to consider by essentially using the "bubble" concept. Nearby atoms are recursively pooled to form "super-atoms" which have a Rabi frequency given by equation 2.23. This could cause errors by artificially forcing correlations among pooled atoms. This can be controlled by increasing the number of "super-atoms" used, to decrease the number of atoms pooled per "super-atom." Third, they eliminate states with more than some maximum number of Rydberg excitations. One does not expect a large fraction of atoms to be excited to Rydberg states within the volume, due to the blockade.

From such simulations, the authors can calculate a number of properties of the Rydberg gas, including excitation fraction (saturation) and excitation statistics. For the purposes of this thesis, we are interested in their calculations of the Rydberg-

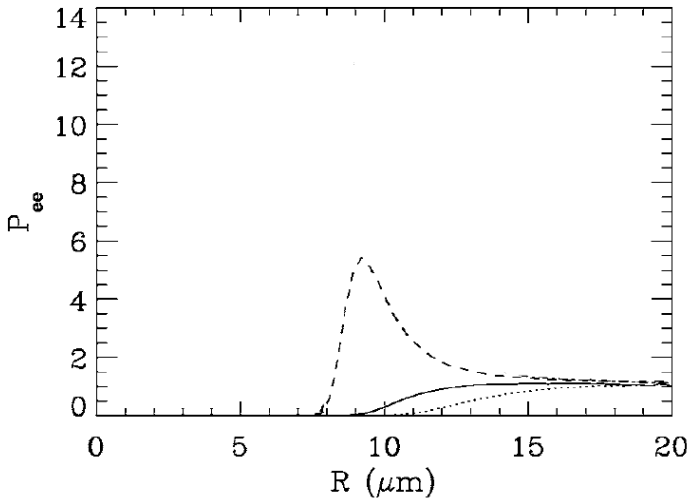

Figure 2.5: Predictions of the Rydberg-Rydberg pair correlation function (P_{ee}) as a function of distance between the atoms. Essentially this is the normalized probability of exciting two Rydbergs at a given separation (see text). For these calculations, $S = 0.2$ (see Equation 2.24). The solid curve is for zero detuning between the excitation laser and the Rydberg transition. The dotted line is for $\Delta\omega = -2/\tau$ and the dashed line for $\Delta\omega = -2/\tau$. Adapted with permission from [47].

Rydberg correlation function. The correlation function is defined as the probability of exciting two Rydberg excitations at a given separation distance divided by the square of the probability of exciting a single Rydberg atom. A value of 1 indicates uncorrelated Rydberg positions, while values of < 1 indicate anticorrelation.

For this calculation the authors used repulsive interactions with an interaction strength approximately equal to that of the $83D_{5/2}$ state of rubidium, based on the interaction strengths calculated by Reinhard et al. [37]. The excitation pulse was taken to be of the form

$$\Omega = \frac{S}{\tau} e^{-t^2/\tau^2} \tag{2.24}$$

where S is the laser amplitude and τ is proportional to the time width of the pulse. Their results are shown in Figure 2.5. The solid curve is for zero detuning between the excitation laser and the Rydberg transition. This shows a blockade radius near 11 μm (where the correlation function crosses through the value 1/2) and uncorrelated Rydberg positions outside this distance, as expected. Also of interest is the effect of

laser detuning on the correlation function. Somewhat surprisingly, a blue detuning ($\Delta\omega > 0$) causes a dramatic increase in the probability of finding Rydberg excitations separated by slightly less than the blockade radius. When the detuning is in the same direction as the van der Waals shift, as here, Rydberg pairs are excited with a separation that tunes the $(N, k = 0) \rightarrow (N, k = 2)$ transition into two-photon resonance (c.f. Figure 1.1 for S-states).[5]

This is the physics that underpins most of the work in this thesis. Measurements of the Rydberg-Rydberg correlation function for on-resonant excitation are discussed in the experiments of Chapter IV. The effects of detuning are investigated in the experiments of Chapter VII.

2.3 Imaging Methods

So far I have reviewed the basics of Rydberg-Rydberg interactions and how this leads to anticorrelations (or correlations) in the positions of Rydberg excitations. In order to measure the Rydberg-Rydberg correlation function described above, I directly image the positions of Rydberg excitations in a cold rubidium gas.

The study of atomic vapors has benefited tremendously from various imaging techniques. Here I present an overview of some techniques used to image atoms, highlighting why the charged particle imaging technique we choose is particularly appealing for our application.

2.3.1 Shadow imaging, and Electromagnetically Induced Transparency

Shadow imaging (see Appendix A) is another name for absorption imaging. A laser beam is shone on an atomic vapor, with a light detector (usually a CCD camera) on the opposite side. The laser is resonant with an atomic transition, so the atoms scatter

[5] Here, Robicheaux and Hernández [47] consider a single Rydberg atom to be excited by a single photon. Experimentally we use two photons to excite a Rydberg atom, as I will explain in Chapter III. So experimentally this is a four-photon transition, as we will see in Chapter VII.

light from the laser beams. A shadow is thereby cast on the CCD based on the spatial distribution of atoms. The imaging time is based on the scattering rate. For imaging ^{85}Rb atoms in the electronic ground state $5S_{1/2}$, a resonant laser beam with 10% of the intensity required to saturate the $5S_{1/2} \rightarrow 5P_{3/2}$ transition (so $I = 0.1I_{sat}$) will scatter photons at a rate

$$\gamma_p = \frac{s_0\gamma/2}{1+s_0} = 1.7 \times 10^6 \quad \text{sec}^{-1} \tag{2.25}$$

where $s_0 = I/I_{sat}$ and $\gamma = 2\pi \times 6$ MHz is the transition linewidth. We typically use imaging times of 20 μs to allow each atom to scatter ≈ 35 photons. Shadow imaging can also be used to indirectly measure velocity distributions in trapped atomic systems by releasing the atoms from the trap and taking a time-delayed image. The achievement of Bose Einstein Condensation (BEC) by [50] was thereby readily identified, showing that at the phase transition the atomic cloud had two components with distinct velocity distributions.

Clearly, the shadow imaging technique is most useful when the system undergoes a closed, cycling transition to scatter multiple photons. There are no such transitions starting from a Rydberg state, so shadow imaging has not been used to date to detect Rydberg atoms. However, a very interesting and inventive recent paper [52] proposes using background atoms to assist in the detection of Rydberg atoms or other impurities in the atomic gas. This would essentially allow the use of shadow imaging to detect Rydberg atoms. Suppose that the Rydberg atom (or impurity) to detect is labeled $|R\rangle$. The probe (background) atoms are sensitive to the presence of $|R\rangle$ because they have Rydberg energy levels $|r\rangle$ that are shifted by interaction with $|R\rangle$. The Rydberg levels $|r\rangle$ do not need to be occupied; one merely needs to probe their energy shifts to detect $|R\rangle$. The energy level shifts are detected by electromagnetically induced transparency (EIT), which I briefly describe here. In the

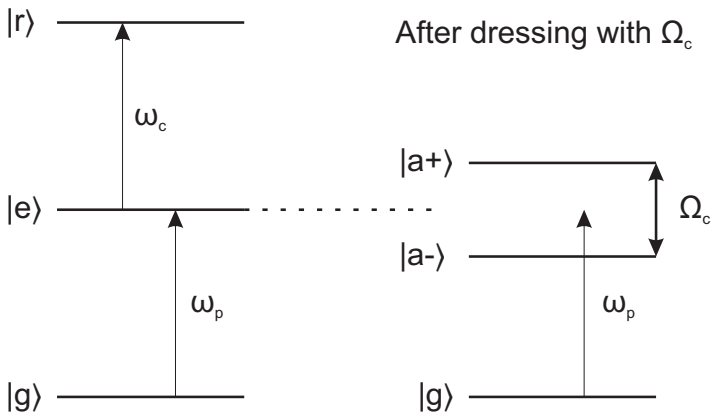

Figure 2.6: Level diagram for background probe atoms used for EIT detection of impurities (Rydberg atoms) in the atomic vapor. The level diagram assumes the absence of impurities; the effect of their presence is considered in the text. This description of EIT draws from [51]. The relevant energy levels are the ground state $|g\rangle$, an excited state $|e\rangle$, and a Rydberg level $|r\rangle$. The states $|e\rangle$ and $|r\rangle$ are coupled by a strong coupling field with Rabi frequency Ω_c and a frequency ω_c resonant with the $|e\rangle \rightarrow |r\rangle$ transition. In the dressed state picture for the Ω_c field, depicted at right, the energy levels $|e\rangle$ and $|r\rangle$ are mixed to become $|a+\rangle$ and $|a-\rangle$, which have an energy splitting of Ω_c. In contrast to the case without a coupling Ω_c, a probe field with frequency ω_p on-resonant with the $|g\rangle \rightarrow |e\rangle$ transition will *not* be absorbed by the medium. The probe absorption amplitudes to the levels $|a+\rangle$ and $|a-\rangle$ cancel due to quantum interference. The medium is transparent for resonant ω_p.

absence of impurities, the probe atoms have an energy level diagram described on the right of Figure 2.6. For resonant ω_c and ω_p, the probe atoms are transparent to the probe laser. However, the presence of impurities shifts the frequency of the $|e\rangle \rightarrow |r\rangle$ transition so that ω_c is no longer resonant. Within a small region (radius ~ 1 μm) around the impurity, the probe atoms are no longer transparent to the probe laser and a shadow is formed. The probe atom density must be large to achieve sufficient absorption from such a small region: in their simulation the authors used a density equivalent to $2.5 \times 10^{14}/\text{cm}^3$. [6] A temperature less than 10 μK was assumed to neglect atomic motion during the imaging. This recent proposal has future promise, and an implementation remains to be seen.

[6] This is quite high, roughly at the upper limit of workable BEC densities. Around this density BEC lifetimes are limited to $\lesssim 1$ sec due to three-body collisions. This density is 4 to 5 orders of magnitude larger than my typical magneto-optic trap (MOT) operating densities.

2.3.2 Fluorescence imaging

2.3.2.1 Alkali atoms

If the optical depth of a sample would not be sufficient to use shadow imaging, one may still be able to use fluorescence imaging. In this case, the light that atoms scatter from the incident laser beam is detected. Fluorescence imaging is routinely used to detect single ions in ion trapping experiments, and can also be used to detect single atoms in a magneto-optic trap (MOT) [53]. Scattering rates and solid angle considerations lead to long illumination times. Recently, experiments have moved to detecting atoms in two-dimensional optical lattices with single-atom, single-site resolution [54, 55]. Objectives include the realization of model Hamiltonians from solid state physics and the study of strongly correlated quantum states.

Again, these methods detect atoms in an electronic ground (or metastable) state by scattering light that is tuned to resonance with a cycling transition. Alkali Rydberg atoms do not have such transitions. In order to detect Rydberg atoms, Schauß et al. [56] have recently prepared a Mott insulator in the lattice, excited Rydberg states, used a beam resonant with $5S \rightarrow 5P$ to push away all the ground state atoms in 10 μs, and then de-excited the Rydberg atoms via stimulated emission for 2 μs. Fluorescence imaging can be used once the atoms are back in the ground state. The fluorescence imaging uses a 0.9 second illumination time; to keep the atoms trapped during this time, the optical lattice is ramped up in power and optical molasses cooling beams are used to produce fluorescence. This length of illumination time is competitive with similar experiments. Bakr et al. [54] use 0.2 sec to 1 sec illumination times in their optical lattice.

The two experiments mentioned above are very impressive in their capabilities. But they are not ideal for imaging Rydberg atoms, due to long illumination times and

the fact that their Rydberg detection requires the removal of all other ground state atoms from the trap. This means that to repeat the experiment one must prepare a new atom sample. This significantly slows down the experimental repetition rate, as a BEC typically takes of order 30 seconds to form and from this BEC one obtains a single image of Rydberg distributions. This will be compared to charged particle imaging methods, below.

2.3.2.2 non-Alkali atoms

Another interesting approach to imaging Rydberg atoms is to add extra internal electronic structure that can be accessed. All experiments I have mentioned thus far use alkali atoms (mostly, rubidium or cesium). Alkali atoms are convenient for laser cooling because their cooling (cycling) transition tends to be in the visible wavelengths, for which lasers are available. They also produce Rydberg states that behave in many respects like atomic hydrogen, due to having only a single valence electron and a nearly point-sized ionic core (in comparison to the Rydberg electron wavefunction). However, it is possible to use other atoms. For example, there are a number of possible advantages to using strontium, an alkaline earth metal [57].

If one does not use an alkali atom, it is possible to have a cycling transition in a Rydberg atom. Rather than de-exciting a Rydberg atom to obtain a cycling transition, as in Section 2.3.2.1, one can then image the Rydberg atom directly. Alkaline earths provide this advantage for studying Rydberg-atom physics [58]. After excitation of the Rydberg electron, the presence of the second valence electron yields an optically active core which can be used for optical trapping or for optical imaging. Fluorescence imaging can be done directly on the Rydberg atom, using a cycling transition of the second valence electron. McQuillen et al. [58] use fluorescence imaging to detect Rydberg atoms of strontium, with a time resolution of 10 ns and an imaging

time of 500 ns. Their spatial resolution is 200 μm, which could be readily improved by optimizing the optical setup. Unfortunately[7], the interaction of the Rydberg electron and second valence electron does not give this fluorescence technique clean Rydberg-state-selective detection. Rather, scattering of the Rydberg electron from an excited second valence electron causes autoionization for low-ℓ Rydberg states on a timescale of ~ 19 ps, causing them to be undetectable by the fluorescence technique. In high-ℓ states, the wavefunction overlap between the Rydberg electron and ionic core diminishes such that the autoionization rate drops below the core radiative decay rate. Atoms in these states can thus be detected with fluorescence imaging.

Rydberg atoms can be forced into high-ℓ states by seeding the Rydberg gas with an ultracold neutral plasma, which induces ℓ-mixing collisions. The Rydberg atoms transition to detectable states over the course of a few μs. This technique is well-suited to studying the evolution of a Rydberg gas to an ultracold neutral plasma, which is a fascinating system in itself [59]. However, it is not a completely general tool for detecting all Rydberg states with spatial sensitivity.

2.3.3 Charged particle imaging

The traditional method for detecting Rydberg atoms is to use an electric field to rip the loosely bound electron from the ionic core, and to detect either the electron or the ion with a charged particle detector [1]. A simple one-dimensional model (which works rather well at low ℓ) estimates the Rydberg atom to ionize at a field of (in atomic units)

$$E = \frac{1}{16(n^*)^4} \quad , \tag{2.26}$$

where $n^* = n - \delta_\ell$, n is the principal quantum number and δ_ℓ is the quantum defect, which accounts for the interaction of the Rydberg electron with the ionic core and

[7] For those of us in the cheering section, hoping for time-resolved optical detection of Rydberg excitation hopping through an atomic vapor.

depends on the angular quantum number ℓ. For the $60S_{1/2}$ state $E = 30$ V/cm, which is a relatively modest field.

Traditionally, such detection methods have had minimal sensitivity to the spatial origin of these particles in the Rydberg gas. Most configurations used for ionization electrodes are not optimized for imaging the positions of Rydberg atoms onto the charged particle detector. As a modification of this technique, we instead use a needle tip as an ionization electrode. We call this the "tip imaging probe" (TIP). When switched to high voltage, the TIP produces a strong, radially divergent electric field. This field ionizes the Rydberg atoms, and the ions are extracted along the divergent field lines. The ions are detected approximately 16 cm away by a microchannel plate detector (MCP) which has a spatial resolution of $\gtrsim 10$ lines/mm. The method resembles field ion microscopy, and leads to magnified ion images of the initial Rydberg atom locations.

The details of the ion trajectories from TIP to MCP will be considered in Chapter V. For an initial estimate, if we assume that the ions follow straight-line trajectories to the MCP we can calculate the magnification ratio m between separations of ions in the MCP plane and separations of Rydbergs in the excitation plane. This ratio should be given by consideration of similar triangles:

$$m \sim \frac{\text{distance from TIP to MCP}}{\text{distance from TIP to object plane}} \tag{2.27}$$

where the "object" in question is the collection of Rydberg excitations. As implemented in the experiments of Chapter VII, I have the excitation plane $\sim 200\mu$m above the TIP. With the MCP approximately 16 cm above the TIP, the estimated magnification is then $m \sim 800$. Our measured magnification is less than this, but still $m \approx 320$. With the spatial resolution of the MCP, even $m \sim 320$ affords us with sub-micron resolution in imaging the Rydberg atom positions. This is highly

competitive with the diffraction-limited optical detection methods described above.

In addition to spatial resolution, the method has good time resolution. In my experiment the Rydberg atoms are ionized in < 50 ns by the rapidly-switched electric field. This gives much better time resolution than the optical methods described above. The relevant comparison here is with the 0.2 to 1 sec imaging time of the optical lattice experiments, and the required several-μs evolution to high-ℓ states for imaging strontium.

In addition to my experiment, the Raithel lab has also designed and implemented several other apparatus with spatially-sensitive Rydberg detection. The use in our BEC-ion experiment showcases another of the advantages of using field ionization to detect Rydberg atoms. As mentioned above, it takes on the order of 30 seconds to produce an ultracold atom cloud. With the ion imaging method, detection of the produced Rydberg atoms does not destroy the ground state atomic cloud. It is therefore possible to produce circular Rydberg states[8] and watch them oscillate in a magnetic trap [60], using the same ground state cloud for 1000 experimental cycles before it is depleted. If our Rydberg imaging method destroyed the ground state cloud, the experimental repetition rate would slow down by a factor of 1000, making the experiment completely infeasible.

[8]These are maximal angular momentum states, with $|m| = \ell = n - 1$ and toroidal wavefunctions. Hence the name "circular" states.

CHAPTER III

Experimental Setup

In this chapter I present the most important aspects of the experimental setup and the initial characterization of the apparatus, including how certain calibration factors were derived. At the end of the chapter I describe one of the largest challenges of the experiment, which is controlling the voltage on the TIP to a precision of one part in 10^6. The experimental conditions quoted here are used for the experiments of Chapter IV.

3.1 TIP and electrodes

The experimental setup is sketched in Fig. 3.1. As mentioned in Section 2.3.3, the key feature enabling spatial resolution of the Rydberg sample is the ionization electrode: a beryllium-copper needle with a rounded tip of diameter 125 μm.[1] This tip imaging probe (TIP) is surrounded by a closed cage of electrodes whose voltages can be controlled to a precision of several millivolts. These electrodes allow independent control of the electric field in three orthogonal directions. To provide temporal and spatial electric-field stability, the apertures in the electrodes are covered with wire mesh[2] which has 0.51 mm grid spacing and 88% transparency.

[1] The needle is from Signatone, model SE-BCB.
[2] The mesh is made by TWP Inc, product number: 050X050T0012W48T.

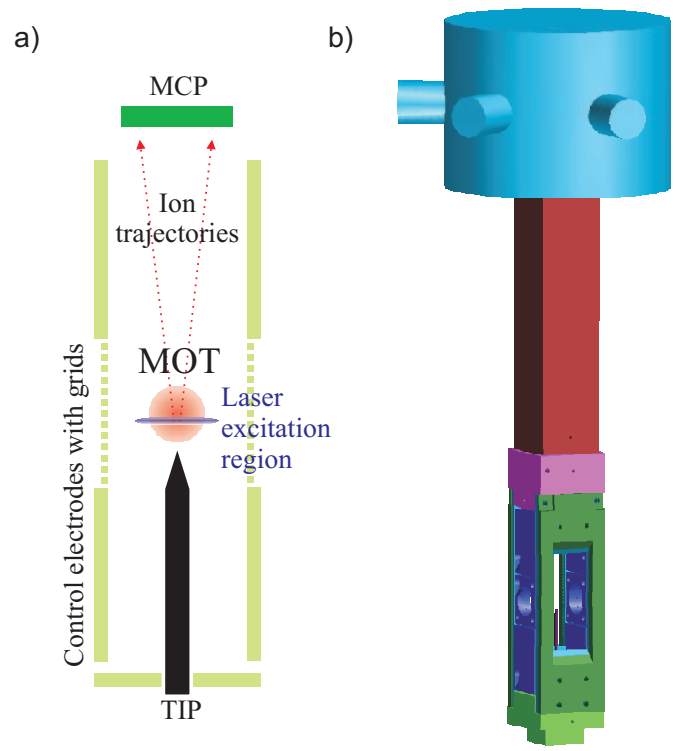

Figure 3.1: (a) Overview of the excitation region and ion detection (not to scale). (b) To-scale drawing of the TIP and surrounding electrode package, as well as the guide tube (red) through which the ions travel to reach the microchannel plate (MCP) ion detector (light blue). The TIP is visible through the aperture in the dark green electrode. See also Figure 5.1 for dimensions.

3.2 Experiment timing

The experiment typically runs at a repetition rate of 30 Hz. I collect ^{85}Rb atoms for about 30 ms in a MOT located ∼500 μm above the TIP. After turning off the MOT light, I optically pump the ground state atoms into the $5S_{1/2}|F = 3, m_{\rm F} = 3\rangle$ state, with the quantization axis along the beam direction. I then excite Rydberg atoms in a two-step process, using counter-propagating 480 nm and 780 nm beams. The excitation region is ∼300 μm above the TIP. The beams are σ^+ polarized and resonantly drive the transitions $5S_{1/2}|F = 3, m_{\rm F} = 3\rangle \rightarrow 5P_{3/2}|F' = 4, m'_{\rm F} = 4\rangle \rightarrow nD_{5/2}|F'' = 5, m''_{\rm F} = 5\rangle$. The red beam has a Gaussian beam parameter of $w = 0.75$ mm, while the

blue beam is focused to $w_0 \lesssim 8$ μm with a theoretical confocal parameter of 0.3 mm.[3] Because of the much larger size of the red beam, the intermediate-state population is uniform across the width of the excitation region. I establish with CCD imaging that the intensity distribution of the blue focus is only weakly altered by diffraction from the mesh. Laser linewidths are of order 1 MHz. Typical Rydberg atom densities are $\sim 10^9$ cm^{-3}, dependent on atomic state and laser power.

After excitation, the TIP is switched to high voltage to produce a strong, radially divergent electric field. This field ionizes the Rydberg atoms, and the ions are extracted along the divergent field lines. The ions are detected approximately 15 cm away by a microchannel plate detector (MCP) which has a spatial resolution of $\gtrsim 10$ lines/mm. The method resembles field ion microscopy, and leads to magnified ion images of the initial Rydberg atom locations. This image is captured by a CCD video camera, synchronized with the experiment.

In most cases I use 100 ns excitation pulses with a subsequent negligible delay before the field ionization pulse. Under these conditions the atoms can be considered "frozen" in space during the experiment. In Chapter IV these parameters are varied to study their effect on the Rydberg-Rydberg correlation function.

3.3 Magnification calibration

The system's physical magnification factor is determined by the combined ion-lensing effects of the TIP, pulsed to about 400 V, and the MCP front plate, held at -750 V. (This is discussed in great detail in Chapter V). To experimentally calibrate the magnification I scan the focused 480 nm beam laterally across the MCP field of

[3]For the benefit of future graduate students: To do this beam profiling, I programmed a 2-d Gaussian fitting routine. It allows an arbitrary rotation of the 2-d Gaussian, and finds the angles of the principal axes as well as the width of the Gaussian along each axis. This is drastically better than using calipers to block the beam, or even a knife-edge on a hand-operated translation stage: the focal spot is easily found, and the beam width as well as roundness can be measured in a single shot. Furthermore, the precision is the pixel-size of the camera, 6.7 μm, which is drastically better than what is achievable with the $\frac{1}{1000}$-inch calipers. This has proven useful for measuring Rayleigh ranges and also checking astigmatism of focused beams. The program is on the group website.

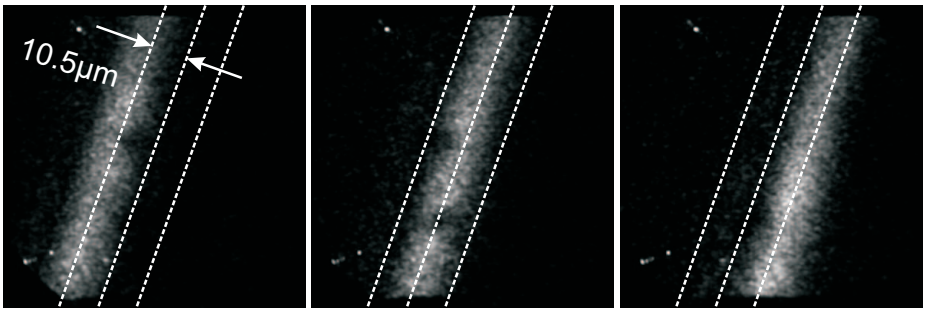

Figure 3.2: To calibrate the imaging system, the excitation region is repeatedly displaced by a known distance. The displacement in pixels on the camera allows us to measure distances from pixels.

view by using a mirror with a piezo actuator on the horizontal axis. This procedure is shown in Figure 3.2. At each position, 500 pictures are averaged to obtain a good sense of the position of the excitation beam. Using the known physical displacement of the beam between images, I determine the scale in the MCP picture. In the experiments of Chapter IV, 1 μm in the excitation region corresponds to 2.2 pixels in the digital CCD images, with an uncertainty of 10%.

The calibration of the piezo-driven mirror is done by focusing the laser beam onto a CCD camera and measuring the beam displacement across the CCD surface. The beam was also checked for beam focus asymmetries due to displacement across the focusing lens; asymmetries were minimal. Figure 3.3 shows the calibration of voltage on the piezo to displacement of the 480 nm beam focus. There is significant hysteresis. When calibrating the magnification with the method of Figure 3.2, I therefore always scan from 50 V *up* to 140 V in 30 V increments. The fit lines shown in Figure 3.3 are fitted over the data in this range only. The nonlinearity shown is an important source of error in the magnification calibration.

The above magnification calibration between pixels (on the camera) and microns (in the excitation plane) is sufficient for all data analysis. However, we would like to compare our physical magnification factor m to the estimate given in Equation 2.27.

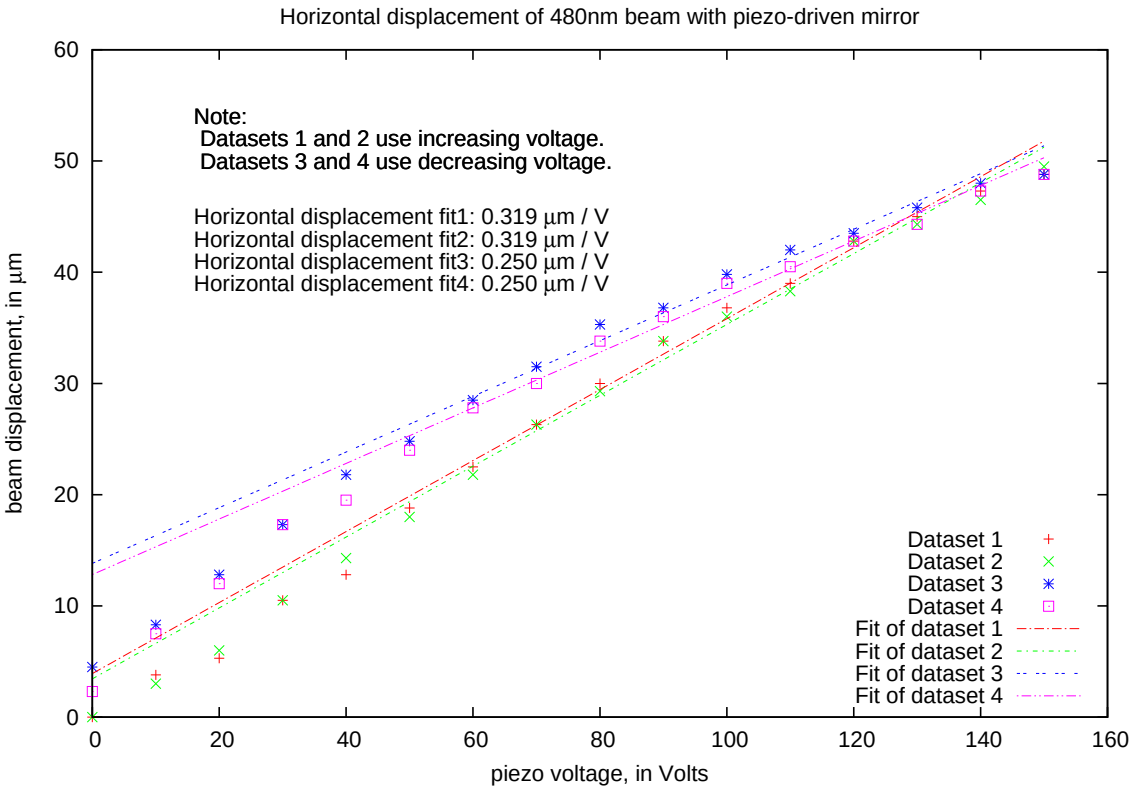

Figure 3.3: Calibration data for displacement of the 480 nm beam using a piezo-driven steering mirror. Datasets 1 and 2 are for increasing voltage; datasets 3 and 4 are for decreasing voltage. The data shows hysteresis. Fit lines for each dataset are calculated using the datapoints in the range 50 V to 140 V, which is the normal operating range used for magnification calibration in the experiment. See text for details.

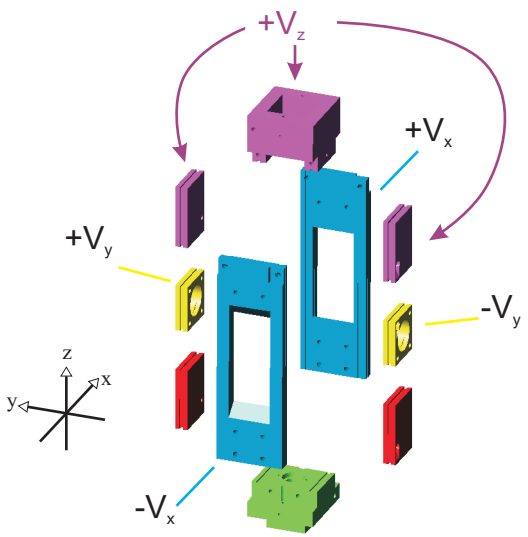

Figure 3.4: Exploded view of electrodes that surround the excitation region, used for electric field control. The purple, blue, and yellow electrodes allow electric-field control in the z, y, and x directions, respectively. Green and red electrodes are grounded.

To do this I have calibrated the pixels on the camera to displacements on the MCP surface. This factor is 40.5 μm on the MCP per pixel on the camera. Based on this factor, for the experiments of Chapter IV I find a linear magnification factor of 90$\times$ between the excitation region and the MCP front surface. (Later experiments have higher magnification, as already mentioned under Equation 2.27.)

3.4 Electric field control

To observe an excitation blockade, it is essential to avoid electric fields during the excitation pulse. Electric fields would cause undesired modifications of the Rydberg-Rydberg interaction potentials, as discussed in Section 2.1.1. Furthermore, electric field inhomogeneity would induce inhomogeneous line broadening and alter the many-body energy level spectrum, potentially breaking the excitation blockade.

Figure 3.4 shows an exploded view of the electrodes used for electric field control. Each of the 10 electrodes is individually addressable in the experiment, but voltages

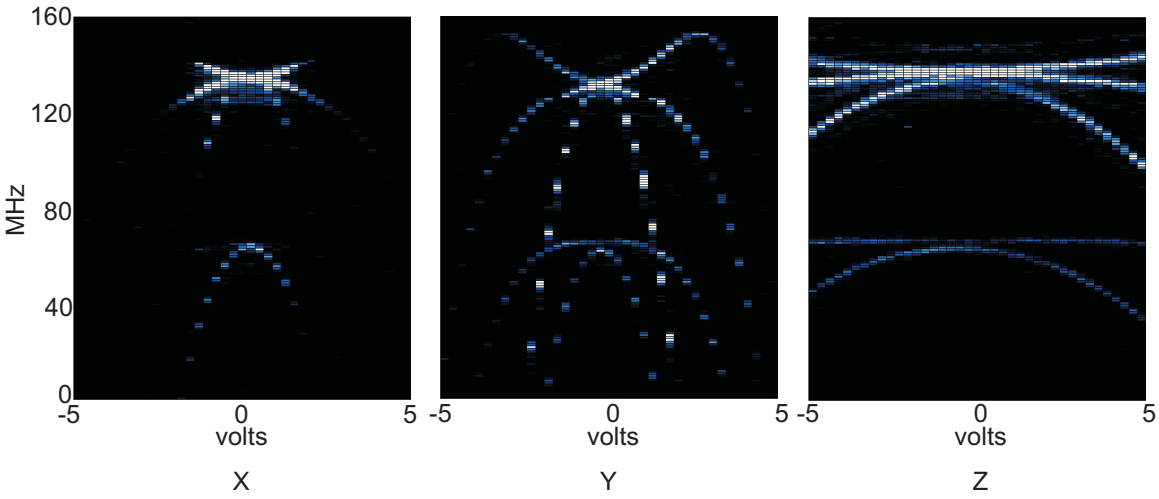

Figure 3.5: Stark maps for excitation to $44D$. Electric field scans are done with the x, y, and z electrode groups, as labeled. White is high count rate, blue is intermediate, and black is zero.

of certain electrodes are linked to each other in the controlling software.[4] The pair of x electrodes have equal and opposite voltages applied to them; likewise for the y electrodes. The z electrodes all have the same voltage applied, and they pull against the red and green electrodes which are set to ground. These electrode groups give control of the electric field in three orthogonal directions (x, y, z).

By measuring the Stark spectra of nD-manifolds as a function of the potentials on the TIP and the electrodes shown in Fig 3.4, I zero the electric field to below $\sim$100 mV/cm. This is low enough to avoid the aforementioned problems of modifications to the Rydberg-Rydberg interactions [37]. A few sample Stark spectra for state $44D$ are shown in Figure 3.5. In the scans, the $44D_{5/2}$ and $44D_{3/2}$ lines all appear, for 5 lines in total. (Positive and negative m_j states are degenerate [1].) The vertical axis is a scan of the 480 nm laser frequency, while the horizontal axis is a scan of the voltage on the x, y, and z electrodes (as labeled in Figure 3.4). The excitation position for these scans is $\lesssim 1$ mm above the TIP.

[4]For reference: the guide tube, shown in red in Figure 3.1, is *physically* electrically connected to the uppermost z electrode in Figure 3.4.

We determine the condition for zero electric field from a Stark spectrum by finding the symmetry axis of the Stark spectrum. The electrode voltage around which the Stark spectrum is symmetric is the electrode voltage that minimizes the electric field. In general, multiple electrodes may need to be scanned in an iterated scheme to get the electric field to be zero, rather than a local minimum. In my experimental setup, the electric fields produced by the x, y, and z electrodes shown in Figure 3.4 are fortunately in orthogonal directions, so we only need to acquire Stark scans once for each set of electrodes to obtain zero electric field.

In addition to the x, y, and z electrodes, the TIP also has a strong effect on the electric field. As mentioned in Section 3.2, for the experiments of Chapter IV the excitation position is ≈ 300 μm above the TIP. In the later experiments of Chapter VII, the excitation position is closer to the TIP at only ≈ 200 μm above. Under these conditions the TIP is then the electrode with *by far* the most significant effect on the electric field sensed by the atoms. It is necessary to set the voltage on the TIP to a value controlled at the 1 mV level during the laser excitation pulses. This is difficult to do, as there are a number of sources of noise. I list a few here so that future graduate students will not have to find them again.

For the ion imaging scheme to work, the TIP must be switched to a high voltage (1600 V in the experiments of Chapter VII) in about 50 ns.[5] [6] To accomplish this fast switching, we use a high voltage switch (model PVX-4140) from Directed Energy Incorporated (DEI), which allows voltages of $\pm$3500 V. This instrument also, unfortunately, has a very noisy output, of order 200 mV. We therefore connect the

[5]The "one part in 10^6" precision quoted in the introduction to this chapter is from the 1 mV control precision and this switched value of 1600 V.

[6]Slower electric field ramps, with timescales of 1 to 100 μs, are are often used for field ionization of Rydberg atoms. These slow ramps are not useful for ion imaging applications because the ions produced at the ionization electric field value have low kinetic energy; they leave the excitation region before the ionization field reaches is maximum value. Their trajectories can then be strongly influenced by other electric fields. A fast electric field ramp will deliver maximum kinetic energy to the ion, resulting in better imaging characteristics.

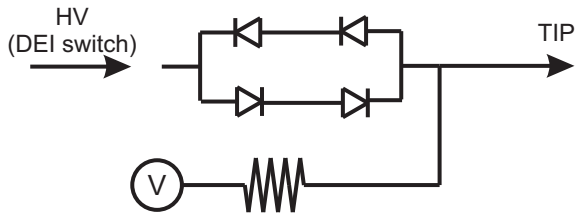

Figure 3.6: Bi-directional diode bridge for the reduction of voltage noise on the TIP. "V" represents a low-noise voltage source used to fix the voltage on the TIP when the HV switch is off. When the HV switch is on, the resistor protects the low-noise voltage source from high voltage. The diodes are 1N4148 small-signal diodes, and the resistor is $R = 100$ kΩ. The schematic given here is the simplest conceptually-correct circuit; a more complicated circuit is used in the experiment due to technical considerations.

switch to the TIP via a bi-directional diode bridge which prevents voltage swings less than about 1 V from passing through (see Figure 3.6). In addition, the DEI switch puts noise out from its *input*, to the low-noise electronics that drive it. This noise can travel through these electronics to a power supply, then to the other low-noise electronics that constitute the voltage source (V) shown in Figure 3.6. The noise can thus travel straight around the clamp switch to the TIP. This discovery led to the introduction of a bi-directional low pass filter on the DEI switch input.

Another source of problems was a slow electric field drift. Over the ~ 10 minutes required to take the Stark scan shown in Figure 3.7, the electric field drifted by about 20 mV/cm. The field continued drifting and settled to a constant value at least an hour after this scan was taken. The eventual determination was that I had turned off the high-voltage pulsing from the DEI switch for an hour while eating dinner, and turned it back on afterwards to resume the experiment. In that hour we believe that rubidium deposited onto the TIP from the background gas in the vacuum chamber, changing the contact potential on the TIP. Once the TIP began switching to high voltage again the equilibrium contact potential changed, leading to the electric field drift. The implication of this is that the repetition rate of the experiment cannot be changed once the electric field has been zeroed. In early experiments (with the

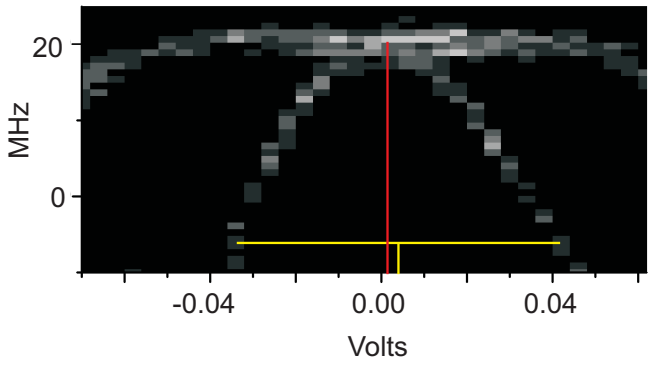

Figure 3.7: Stark map of $57D_{3/2}$, scanning the voltage on the TIP. White is high count rate and black is zero. The Stark map is scanned first in voltage (left to right), then in 480 nm laser frequency (bottom to top). The asymmetry in the slopes of the Stark line show an electric field drift over a timescale of $\sim$ 10 minutes. Yellow lines mark the TIP voltage to zero the electric field at the beginning of the scan, based on left/right symmetry; the red line marks the same at the end of the scan.

excitation region further from the TIP, and thus less affected by the TIP contact potential) it was customary to zero the electric field with Stark scans taken at 120 to 300 Hz repetition rates (such that the scans take on order 10 minutes), and then to slow the experiment down to the normal 30 Hz operation rates required by the camera to perform the blockade experiments. This cannot be done if the electric field begins to drift after the change in timing. In later chapters, all Stark maps and other procedures are done at 30 Hz to avoid this trouble.

3.5 Conclusion

In this chapter I have described the experimental apparatus, as well as the parameters used for the experiments in Chapter IV. I have described some calibration procedures which are necessary for interpreting the data, and also given a flavor of some of the subtler experimental difficulties.

CHAPTER IV

Measuring the Blockade

4.1 Motivation

As has been discussed in previous chapters, the Rydberg blockade could be a valuable tool for quantum computing. It relies on spatially-dependent interactions between Rydberg atoms, and it is this spatial aspect that I am presently interested in. Some spatially-resolved studies have been done; both the distance- [11] and angle-dependence [61] of Rydberg-Rydberg interactions have been examined. The blockade was shown to be effective between spatially separated atom pairs in adjacent dipole traps [30, 31], which is the first step toward practical use in quantum computing. However, no one has previously imaged a system containing multiple Rydberg excitations in order to observe the characteristic minimum spacing between Rydberg excitations indicative of a blockade. In this chapter, I directly image a system containing multiple Rydberg excitations to obtain the Rydberg-Rydberg correlation function. I find evidence of the Rydberg excitation blockade and measure the blockade radius for several principal quantum numbers n.

4.2 Data acquisition and processing

A direct image of the spatial distribution of Rydberg excitations from a single excitation event does not, by itself, provide information about the blockade. While

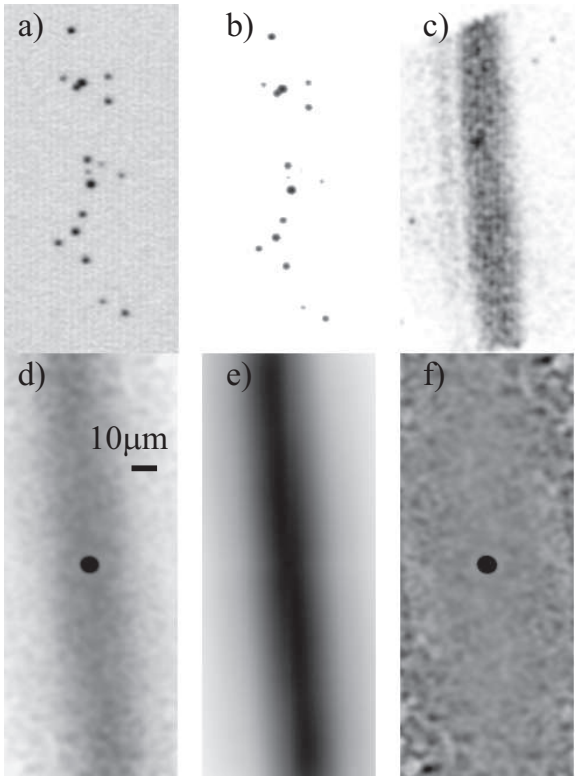

Figure 4.1: Stages in the image analysis process, using state $44D_{5/2}$. All have same scale. (a) Raw image (cropped), (b) filtered image, X, (c) sum of filtered images, (d) sum of autocorrelations, $\bar{A}$, (e) autocorrelation of sum of images, B, (f) normalized autocorrelation, $\bar{A}^1$.

the blockade radius provides a hypothetical minimum spacing between excitations, the excitations might be spaced considerably farther apart. Furthermore, the projection of a 3-dimensional distribution onto a 2-dimensional image means that excitations can appear to be closer together than the blockade would allow. Thus, useful data from each image is in the form of an autocorrelation: a measure of the distances between detected excitations. Because there are only a few Rydberg excitations per image, and because of the range of possible of distances between excitations even with an effective blockade, I must examine and process of thousands of images.

The procedure of data acquisition and processing begins with taking 10000 CCD images of the MCP phosphor screen, each image showing the ion impact positions for a single experimental cycle (as in Figure 4.1(a)). A CCD image consists of these blips

plus background noise from the camera. To eliminate the background, I determine the maximum background level and subtract it from the image, setting all negatives to zero. This procedure yields filtered images, denoted by X (Figure 4.1(b)). The autocorrelation of each filtered image is calculated, and is denoted A. The individual autocorrelations A are then added to construct $\bar{A}$ (Figure 4.1(d)). I can write this as follows, using subscripts for the pixel coordinates and superscript α to enumerate the images:

$$A^{\alpha}_{\mathrm{i,j}} = f(\mathrm{i,j},N,M)\sum_{\mathrm{n,m}} X^{\alpha}_{\mathrm{n,m}} X^{\alpha}_{\mathrm{n-i,m-j}} \tag{4.1}$$

$$\bar{A}_{\mathrm{i,j}} = \sum_{\alpha} A^{\alpha}_{\mathrm{i,j}} \quad , \tag{4.2}$$

where

$$f(\mathrm{i,j},N,M) = \frac{NM}{(N-|i|)(M-|j|)} \quad , \tag{4.3}$$

$N \times M$ is the image size, and (i,j) is the displacement. The normalization factor f eliminates finite-array effects in Equations 4.2 and 4.4, as it causes flat images to have flat autocorrelation functions rather than pyramidal ones.

The signal $\bar{A}$ has three main structures: a central peak due to the correlation of a blip with itself[1], an overall cigar shape due to the geometry of the excitation region, and structure due to correlations between ion positions. It is this third structure that I wish to isolate in my analysis. The raw autocorrelation $\bar{A}$ is useful for qualitative analysis, as it is the easiest to interpret by eye. However, for quantitative analysis I must eliminate the shape of the beam. To do so I first sum the images (Figure 4.1(c)) and take the autocorrelation (Figure 4.1(e)):

$$B_{\mathrm{i,j}} = f(\mathrm{i,j},N,M)\sum_{\mathrm{n,m}} \left(\sum_{\alpha} X^{\alpha}_{\mathrm{n,m}}\right)\left(\sum_{\beta} X^{\beta}_{\mathrm{n-i,m-j}}\right) . \tag{4.4}$$

[1] We call this the "self-term."

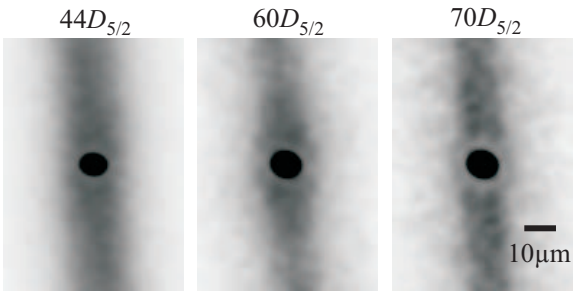

Figure 4.2: Autocorrelations $\bar{A}$ for $44D_{5/2}$, $60D_{5/2}$, and $70D_{5/2}$. In the datasets shown I use a laser intensity of 3.4 I_{sat} for the lower transition, and the lowest intensity setting (nearest the saturation knee) for the upper transition.

The autocorrelation B does not contain any information about Rydberg-Rydberg correlations, but still shows the overall shape of the excitation region. This allows me to divide out the beam shape by defining a normalized $\bar{A}^1$,

$$\bar{A}^1_{\mathrm{i,j}} = \bar{A}_{\mathrm{i,j}}/N_{\mathrm{p}}B_{\mathrm{i,j}} \quad , \tag{4.5}$$

where N_{p} is the number of pictures in the dataset. The normalization of $\bar{A}^1$ is such that a value > 1 (< 1) should indicate a correlation (anticorrelation) of ion positions.

4.3 Autocorrelation data

I take data at several combinations of red and blue laser powers. For the intensity of the lower transition beam I use intensities of 1.7 I_{sat} and 3.4 I_{sat}, where the saturation intensity $I_{\mathrm{sat}} = 1.6\ \mathrm{mW/cm^2}$. For each of these intensities I measure the atom number as a function of the intensity of the upper transition beam and observe saturation behavior as in Ref. [29]. To acquire images for the autocorrelation analysis described above, I select several intensities of the upper transition beam around and beyond the knee of the measured saturation curves. I find that the autocorrelations nearest the knee tend to show the clearest correlation-induced structures.

Figure 4.2 shows $\bar{A}$ measured for states $44D_{5/2}$, $60D_{5/2}$, and $70D_{5/2}$. For all three states, I observe a ring-shaped dip around the central self-correlation peak in the

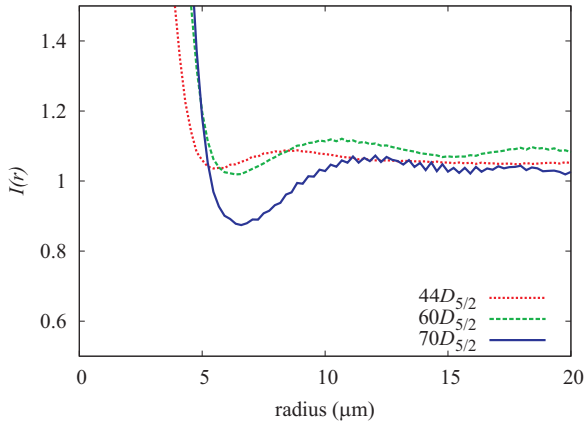

Figure 4.3: Angular average of $\bar{A}^1$, $I(r)$, for $44D_{5/2}$, $60D_{5/2}$, and $70D_{5/2}$. Curves correspond to images in Figure 4.2.

autocorrelation. Such dips are present in most of my data, with the degree of visibility depending on excitation parameters. The absence of dips in some data indicates that they are not artifacts of the imaging or image processing. I find that laser frequency fluctuations can make the dips change in depth and diameter. Furthermore, a variety of other parameters affects the results, as will be discussed in Section 4.4.

4.3.1 Extracting a blockade radius

To quantitatively compare the autocorrelations $\bar{A}^1$ of different states, in Figure 4.3 I plot $I(r)$, defined as the angular average of $\bar{A}^1$. $I(r)$ is analogous to the radial pair-correlation function calculated by Robicheaux and Hernández [47], described in Section 2.2.3.[2] The self-term fills the region $r < 5$ μm. I do not remove the self term due to the risk of producing a false blockade signal. Between 5 and 10 μm, each curve has a dip indicating an anticorrelation in Rydberg atom positions, as was qualitatively observed in Figure 4.2. The minima of $I(r)$ do not approach zero in part because I am projecting a 3-dimensional sample onto the detector plane, which reduces the visibility for even a perfect blockade.

[2]Here I note the difference between the autocorrelation and the pair-correlation function. The pair-correlation is the correlation of the position of each ion with the positions of each *other* ion. The autocorrelation, in contrast, additionally includes the correlation of an ion with *itself*, giving rise to the self-term.

Figure 4.3 shows that the blockade radius increases with principal quantum number n. However, there is no obvious choice for a method to measure a blockade radius from each curve, as the curve's shape is determined by both the blockade-induced dip and the self-term.

To determine a good measure for the blockade radius, I simulate the excitation/blockade process for my geometry and z-projection conditions, using a stochastic, non-quantum model. I find that the inflection point after the minimum of each $I(r)$ curve is close to the input hard-sphere blockade radius. I thus use this inflection point as my measure of the blockade radius. I note that in the simulations the self-term diminishes the dip depth and can shift the dip position. If the input blockade radius is close to the self-term width, the radius indicated by the inflection point is 1–2 μm higher than the blockade radius. When the blockade radius is much larger than the self-term width, the inflection point method underestimates the input blockade radius by $\lesssim$1 μm.

For the states $44D_{5/2}$, $60D_{5/2}$, and $70D_{5/2}$ I measured the radii on nine, six, and nine curves. One additional curve was discarded for $70D_{5/2}$; although its dip minimum was consistent with other data, the position of its inflection point was unclear. Five additional curves for $44D_{5/2}$ were thrown out because there was no dip, as discussed below. The measured blockade radii are shown in Figure 4.4. The error bars indicate the 10% uncertainty from the magnification calibration; this systematic uncertainty dominates the uncertainty due to measurement statistics by a factor of at least two.

In Figure 4.4 I compare the measurements to predictions based on an excitation bandwidth $\delta\nu_{\mathrm{L}}$ ranging from 5 to 12 MHz and interaction strengths as determined from Reinhard et al. [37] (see Section 2.1.2). The blockade radius for the van der

Waals interaction has been calculated to be

$$r_{\mathrm{b}} \approx a_0 \left[\frac{\Delta\tilde{W}^{(2)}(n^*)^{11}}{h(\delta\nu_{\mathrm{L}})} \right]^{1/6}, \tag{4.6}$$

where a_0 is the Bohr radius, $n^* = n - \delta_l$ is the effective principal quantum number, δ_l is the quantum defect, and $\Delta\tilde{W}^{(2)}$ is a scaled, second-order, state-dependent van der Waals coefficient as explained in Section 2.1.2. $\Delta\tilde{W}^{(2)}$ is scaled such that it would be independent of n^* in the absence of resonant level shifts. The assumed value for $\delta\nu_{\mathrm{L}}$ has little effect due to the sixth-root dependence.

Figure 4.4 shows that the measured blockade radii are within a factor of two of the predictions. Further, the amount by which the blockade radius increases between the probed n levels is as expected. The measured blockade radii exceed the calculated radii by 2–3 μm. The difference may be because Equation 4.6 models the interaction between two atoms and excludes many-body effects [15]. Ates *et al.* have previously seen evidence that theory based on pair-wise interactions underestimates the blockade radius [48].

4.4 Characterizing the blockade

To test if atomic motion or the degree of excitation saturation modifies the observed correlation behavior, I vary laser powers, excitation pulse duration, and field extraction delays. In general, increasing the laser power, or the excitation duration at constant power, diminishes the dip depth (defined as the curve asymptote minus the dip minimum). For instance, increasing the excitation duration for state $70D_{5/2}$ from 100 ns to 400 ns causes the dip depth to decrease from 0.24 to 0.04. This behavior could be caused by an increased z-depth of the saturated part of the excitation region. In my simulations the degree to which the dip depth is diminished depends on the assumed beam focus quality. Adding wings to a Gaussian focus, as suggested

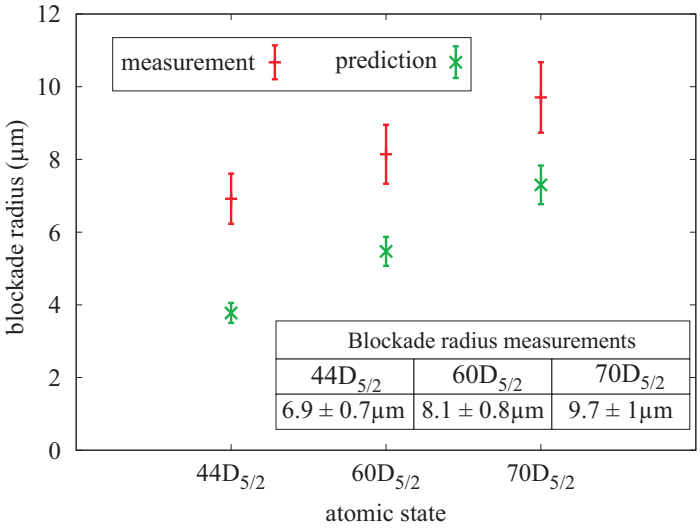

Figure 4.4: Comparison of blockade radius measurements (+) with predictions (×) based on Reinhard et al. [37].

by Figure 4.1(c), yields better qualitative agreement with my data.

Laser power has a greater effect for the case of excitation to $44D_{5/2}$ than for the other states: in five $I(r)$ curves the dip disappeared entirely. I expect this is partly due to saturating the atomic transition for $44D_{5/2}$ more strongly than for $60D_{5/2}$ or $70D_{5/2}$. It is also possible that, of the three states I studied, $44D_{5/2}$ is the most susceptible to laser parameters due to having the shallowest dip, closest to the radius of the self-term. Another possibility is that the blockade efficiency is diminished due to the proximity of the Förster resonance, as suggested by Younge et al. [15] and Walker and Saffman [62].

By varying the delay between excitation and field ionization I test the longevity of the correlations. They are remarkably long-lived. The dip depth decreases by about half over 10 μs, despite possible atomic motion and ionization during this time [42, 63]. This result awaits a future theoretical explanation.

Some of my data, using linear laser polarization and a few MHz of detuning, show additional structures. The autocorrelation in Figure 4.5(a) exhibits multiple rings, indicating long-range Rydberg-Rydberg correlations. The autocorrelation in

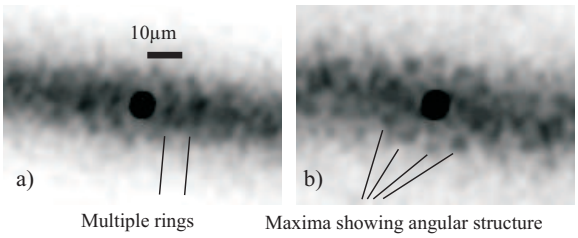

Figure 4.5: Some autocorrelations ($\bar{A}$) showing possible long-range and angular structure for state $44D_{5/2}$.

Figure 4.5(b) hints at multiple maxima in a ring about the center, indicating possible angular dependence of the Rydberg-Rydberg correlation function. There have been predictions of crystal-like structure in Rydberg systems [64], but the detailed excitation conditions are important in generating these structures. The possibility of exciting Rydberg crystals will be discussed further in Chapters VII and VIII.

4.5 Conclusions

In summary, in this chapter I have obtained spatially-resolved images of blockaded Rydberg atom samples and evaluated the Rydberg-Rydberg correlation function. This is the first time the Rydberg blockade has ever been observed through direct spatial imaging. Having observed a blockade, I measured the blockade radius for several quantum states. I have also tested the dependence of the blockade on parameters such as laser power, excitation duration, and detection delay. All of the results are in good qualitative agreement with theory. I have also observed the first hints of higher-order spatial structure due to the blockade. In later chapters, particularly Chapter VII, I will build on this work, re-examining it with greater ion-imaging magnification, and examining the effects of various external potentials on the blockade radius.

CHAPTER V

Ion Trajectory Simulations

5.1 Motivation

It is clear from our previous data that we are limited by spatial resolution. We desire higher magnification to see the blockade more clearly and to resolve smaller structures, such as a Rydberg crystal [2,3] or Coulomb effects (explained in section 5.4). We perform simulations of the ion trajectories in our chamber to see what limits magnification, and what magnification we should expect.

5.2 Hyperrelaxation method for electric field calculation

The ions travel from the TIP to the MCP in a region fully enclosed by electrodes with controlled potentials. To determine the ion trajectories through this region we calculate the electric potential throughout this volume using a hyperrelaxation method. Hyperrelaxation is an adaptation of the relaxation method [65] often used to numerically solve the Poisson or Laplace equation.

In the relaxation method, the system is discretized on a rectangular grid and each grid point (i, j) is assigned a value for the electrostatic potential, $\Phi(i, j)$. Boundary conditions can be set on the electrode surfaces by e.g. fixing the potential for certain grid points. One then solves for the potential in the rest of the interior volume. An initial guess is chosen for the $\Phi(i, j)$ on the interior, e.g. a constant throughout. One

then iterates over the volume to calculate a new potential for each point, $\Phi_{new}(i,j)$. This value $\Phi_{new}(i,j)$ is chosen as a weighted average of the potential at neighboring points on the grid. Iteration over the volume is done until the potential at each point ceases changing between iterations to within some specified accuracy.

We can consider the speed of convergence of the potential at each point on the grid. The points near the boundary benefit from the known boundary values, and so tend to obtain accurate potentials in early iterations. Information (about the boundary values) "flows" across the grid to the interior. If this information flow can be sped up, the algorithm would converge faster. The hyperrelaxation method we use speeds up convergence by several methods:

1. We start with a coarse grid, with grid-cell areas $\sim 16 \times 16$ larger than the final grid. After solving on a coarse grid, we gradually make it finer.
2. On the coarse grids, we have a looser restriction on convergence required for terminating the iteration: 10^{-10}, instead of 10^{-12} difference between steps.
3. We overshoot the change in potential at each point when doing each iteration of the relaxation. This is sometimes referred to as the successive over-relaxation (SOR) method.

In method 3 a "hyperrelaxation parameter" is used to determine how far to overshoot in each step. If this parameter is too large ($\geqslant 2$ in two dimensions) it changes the behavior from a Laplace equation to a wave equation. The potential then oscillates in time rather than converging. We use a hyperrelaxation parameter of ~ 1.95 to give damped waves, and faster convergence. In addition, there is a "hyper-drop" parameter which modifies the hyperrelaxation parameter between steps. Correctly choosing the hyper-drop parameter makes the code run faster at the beginning and converge a bit better at the end.

5.2.1 Simulation geometry

We approximate our experimental geometry as cylindrically symmetric in order to reduce the electric field calculation from 3D to 2D. This helps to fit the hyperrelaxation grid into available computer memory. The two most critical regions of the apparatus (concerning their effect on the ion trajectories) actually do have cylindrical symmetry: the TIP itself, and the volume near the MCP, inside the MCP guard tube. (See Figure 5.1 for the labeled regions.)

The guide tube, which surrounds the region between the TIP and MCP, has a square cross section in the experiment. The simulation's guide tube radius is chosen to give the same cross-sectional area as inside the experiment's square guide tube. For reference, the size of the experimental guard tube is marked in color in Figure 5.1: the square's side in red and the diagonal in blue. We do not expect the cylindrical approximation to have any effect on the ion trajectories inside the guide tube, as the ions start near the central axis at the TIP and most of their initial change in kinetic energy occurs in this region. It is possible that the cylindrical approximation has an effect in the transition between the guide tube and guard tube near the MCP, where there can be a large voltage step and the ions do tend to be far off-axis. We will see these results in Section 5.3.

To perform these simulations of ion trajectories, I calculate the electrostatic potential for a variety of voltages set on the TIP and the front plate of the MCP. The walls of the guide tube (leading from TIP to MCP) are always grounded. The MCP guard tube is electrically connected to the MCP front plate, and both are held at the same voltage.

In the next section, I examine the electrostatic potential calculation for a single voltage setting on TIP and MCP. I return to the ion trajectories in Section 5.3.

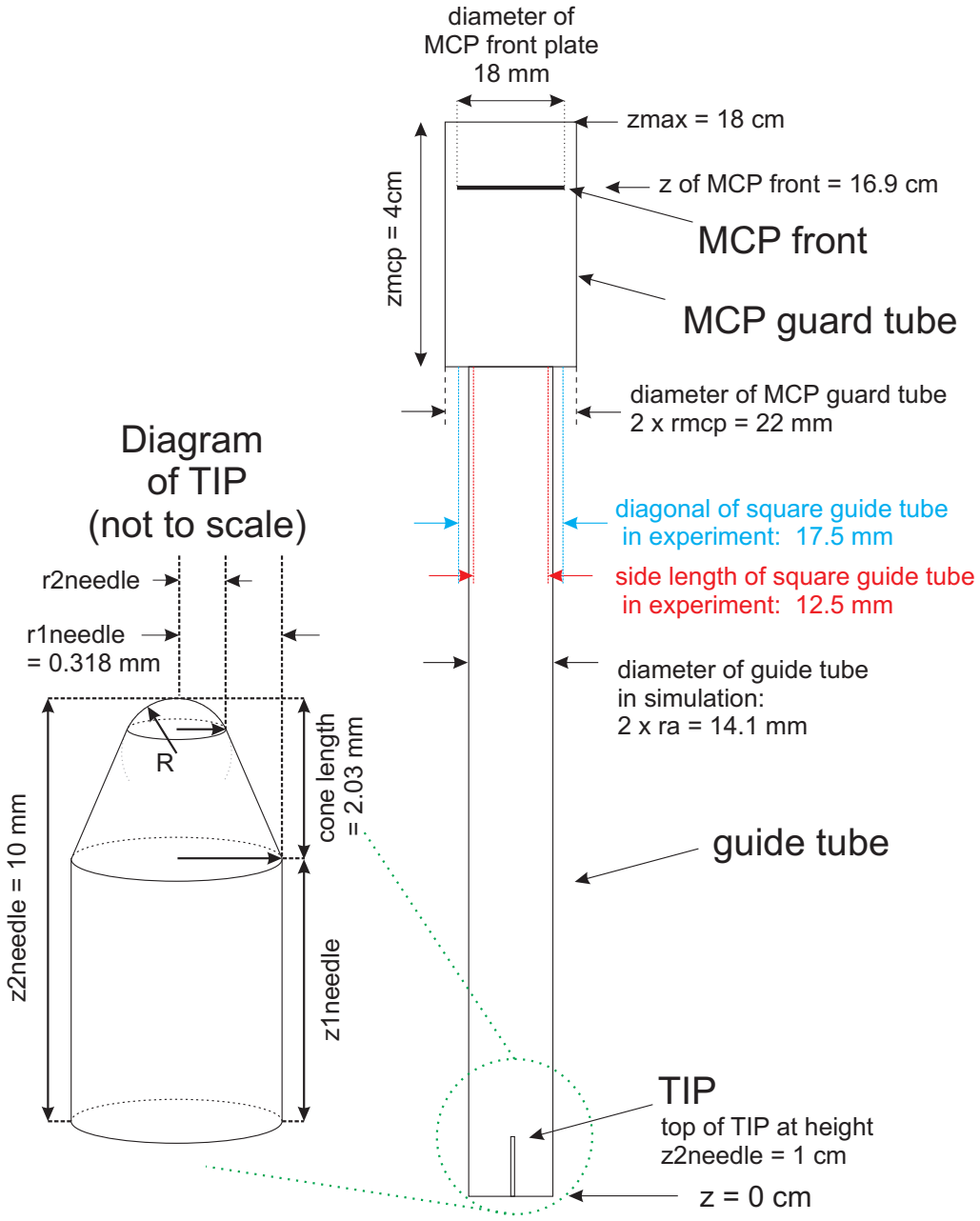

Figure 5.1: *At right*: To-scale drawing of the geometry used in the simulation, showing positions of the electrode surfaces. For reference, I have included some of the variable names used for important dimensions in the simulation. *At left*: A blown-up diagram of the TIP. Near the top of the TIP, the geometry in the simulation has been kept identical to the specifications from the manufacturer. The TIP is a cone on top of a cylinder, where the cone point has been mechanically ground down to a diameter of $2 \times R = 125$ μm (where R is marked in the diagram). The cone height is 2.03 mm, which includes the partial-hemisphere from grinding. If we consider the end of the TIP to be the mathematical union of a sphere with a truncated cone, as drawn, I have recessed the sphere below the surface of the truncated cone to smoothly match their edges around the circle defined by "r2needle".

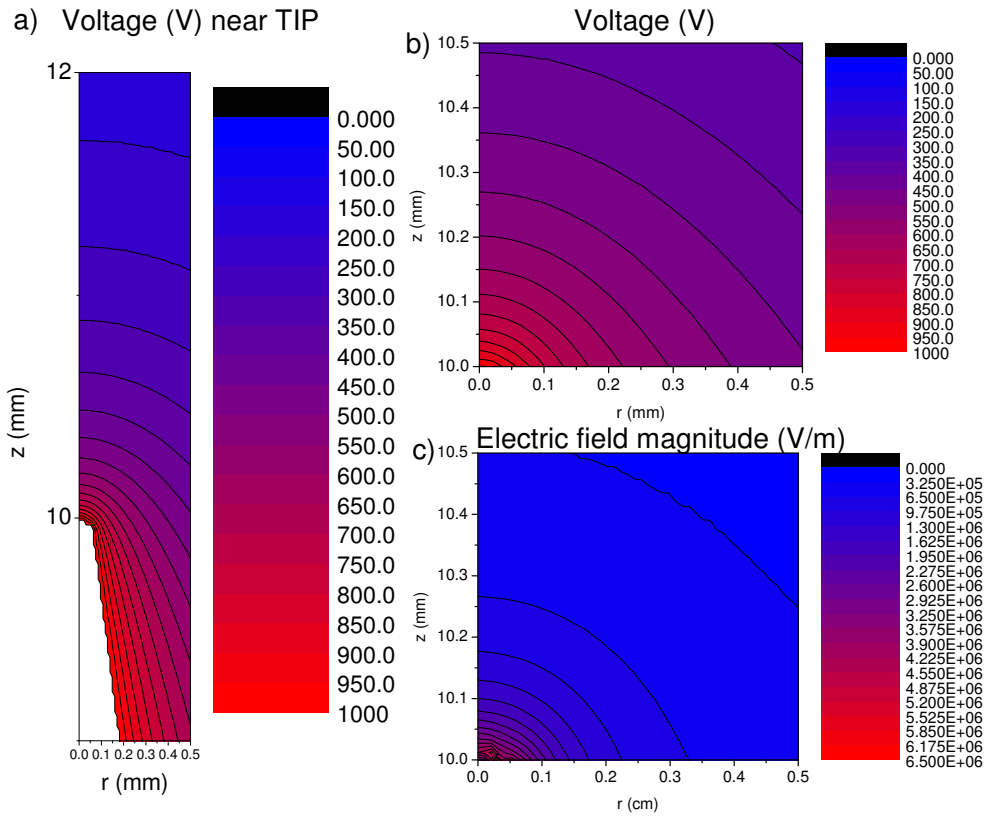

Figure 5.2: Plots of (a,b) the voltage and (c) the electric field magnitude $|E|$ near the TIP surface, from simulation. Plot (a) includes the end of the TIP, in white; (b,c) show a further-zoomed in region just above the tip surface. Note that the top of the TIP is at $z = 10$mm in the simulation volume, for comparison with plot axes. All plots are shown with a 1:1 aspect ratio between z and r. The TIP is set to 1000 V.

5.2.2 Results of simulation

Here I present the results of the electric potential calculation with the TIP at 1000 V and the MCP at 0 V. This allows easy scaling to obtain the results for other TIP voltages, for regions near the TIP. Figure 5.2(a) shows an excerpt from the calculated potential used in trajectory and magnification simulations, showing the region near the TIP. (The rounded end of the TIP can be seen.) Figure 5.2(b) shows a further-zoomed in region just above the TIP surface, in which the laser-excitation region resides. Figure 5.2(c) shows the electric field in the same region as the potential in (b).

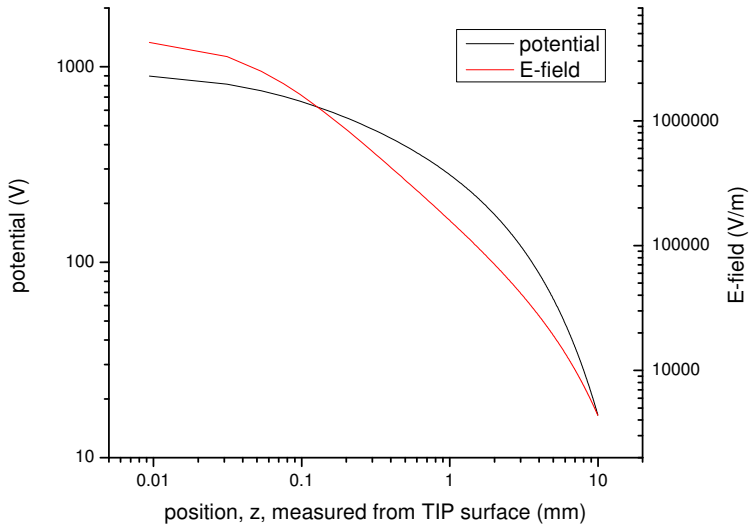

Figure 5.3: Plots of the voltage and electric field vs distance above the TIP. The TIP is at 1000 V. Note: in contrast to Figure 5.2, here the TIP is taken to be at the origin.

z-distance above TIP (μm)	V (Volts)	E (V/cm)
185	562	9170
207	543	8230
Interpolated value:		
200	545	8500

Table 5.1: Simulation results for the voltage and electric field at the grid points nearest 200 μm above the TIP, and an interpolated value at 200 μm. Grid points in the simulation are separated in the vertical direction by 22 μm.

For the experiments of Chapter VII we use an excitation position ~ 200 μm above the TIP, so I quote results for this position. The simulation uses a grid step size in the z-direction of 22 μm, so the values of V and E at the nearest points are displayed in Table 5.1, as well as the interpolation at 200 μm. This interpolation provides a calibration factor between the TIP voltage and the electric field: 1 V on the TIP gives an electric field of 8.5 V/cm at 200 μm above the TIP. This agrees well with an experimental calibration done by taking a Stark map (see Section 3.4) of the $72D$ line at $\sim 215 \pm 10$ μm above the TIP, yielding 8.7 ± 0.3 V/cm per V on the TIP. [1] Electric field zeroing can be done to a precision of about 2 mV on the TIP, which we can thus convert to a residual field of $\lesssim 20$ mV/cm.

Due to the large inhomogeneity of the electric field close to the TIP, we should consider the variation of the electric field over the excitation volume. Field variation can be estimated based on the change between the 185 μm and 207 μm positions in the simulation (Table 5.1). For a voltage of 1 mV on the TIP, the change in electric field across a 5 μm excitation region (defined by the width of the 480nm beam) would be 0.2 mV/cm. From field-zeroing resolution we can then expect a variation of the electric field by 0.4 mV/cm over 5 μm, which is negligible in terms of its impact on spectral linewidths. The 20 mV/cm field itself left over due to field zeroing resolution would lead to a line broadening of the $72D_{5/2}$ line by splitting the $m_j = 1/2$ and $m_j = 5/2$ components by 0.69 MHz. This is also quite small compared to measured Rydberg excitation linewidths of $\sim$5 MHz. We expect, then, that the electric field is not a significant source of line broadening; Rydberg-Rydberg interactions are a much more likely broadening mechanism.

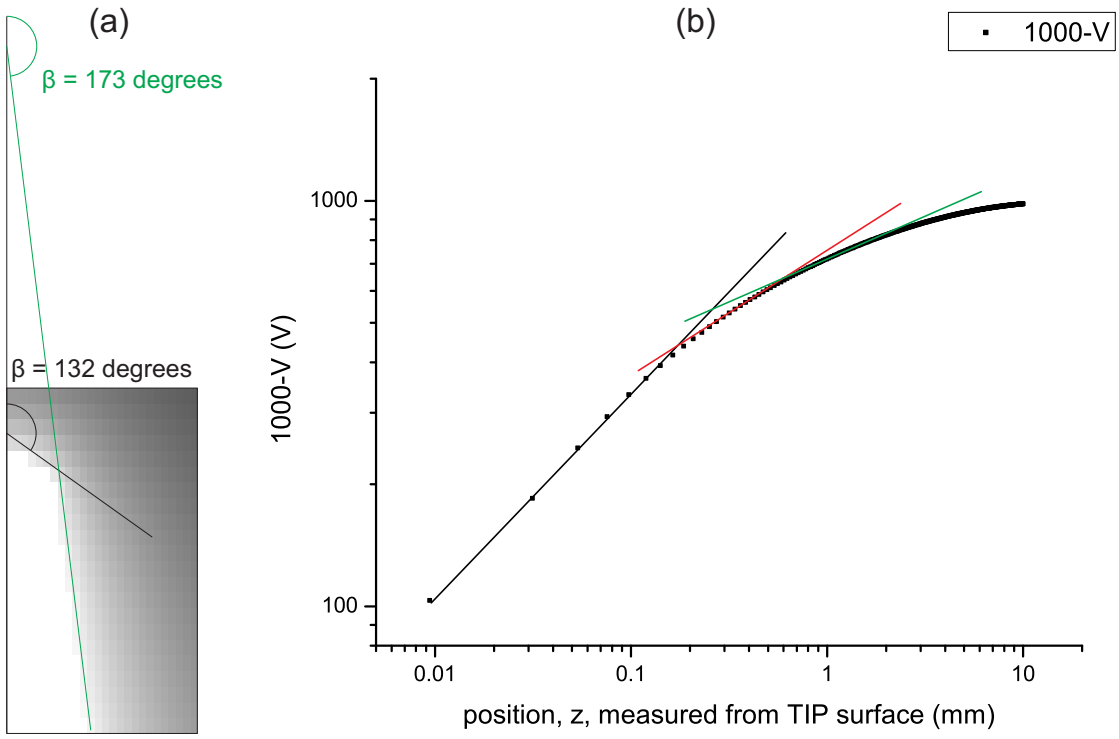

Figure 5.4: *At left:* Geometry of the TIP in the simulation. The image is an excerpt from the hyperrelaxation grid, showing the calculated potential. The pixels are asymmetric according to the grid spacings $dz \approx 22$ μm and $d\rho \approx 11$ μm. The TIP appears in white. The top of the pixelated "hemisphere" has an angle of $\beta = 132$ degrees with the vertical. The angle of the cone away from the rounded top is $\beta = 173$ degrees. *At right:* Voltages from the simulation (points) as a function of distance above the TIP. The TIP voltage has been set to ground, and "far away" to 1000 V, to conform with the convention of Jackson [65]. The slopes of the tangent lines indicate the power-law dependence of V at various positions. The slopes indicate power laws of: black $\Rightarrow z^{0.50}$ nearest the TIP, red $\Rightarrow z^{0.32}$ at 360 μm above the TIP, and green $\Rightarrow z^{0.22}$ at 1 mm above the TIP. See text for comparison to analytical estimates based on Jackson [65].

5.2.3 Comparison with analytical calculations

To check that the results of the simulation are reasonable, before continuing we should compare them to analytical calculations. In this section, l compare the voltage dependence with that given by Jackson [65, pp104-107] from a sharp conical point. The solution involves Legendre functions of non-integer order ν, and gives a potential that depends on the angle β of the conical point. The angle β determines ν, and if we label the radial distance from the point as r (in 3D) then the potential behaves as $\sim r^{\nu}$. Note that $\nu > 0$ so the potential *grows* with distance from the point; the conductor is considered to be ground, and "far away" is some non-zero potential.

This model will only be an approximation for us, since the TIP is not a perfectly sharp cone, as seen in Figures 5.1 and 5.2(a). If sharp, it would extend another 500 μm further in z. This means that, at 200 μm from the TIP, the excitation region is very much in the near field, affected by the bluntness of the tip.

To apply the model, one can look closely at the approximated shape of the TIP in the simulation to see the apparent sharpness of the "hemisphere". This is shown in Figure 5.4(a). The cone angle β is measured down from the z-axis to the surface of the conductor. (So $\beta = \pi/2$ is a plane, $\beta < \pi/2$ is a conical hole bored in a conductor, and $\beta > \pi/2$ is a needle tip.) In the simulation, the angle nearest the top of the TIP (accounting for dz and $d\rho$ stepsizes) is $\beta = 132$ degrees (shown in green, in Figure 5.4a). Using this angle, we can compare the simulated voltage to the analytical results. The angle $\beta = 132$ degrees gives $\nu = 0.6$ [65], so the potential then behaves as $V \sim r^{0.6}$. Plotting the simulated V gives a dependence of $V \sim z^{0.5}$ (shown in green, in Figure 5.4b), which is close to that expected. (Here, I use z as the distance above the TIP, rather than the more-general 3D distance r.)

[1]The agreement between the measured and simulated electric field is thus fairly good considering the accuracy of placement of the excitation region must be within about 20 μm to achieve this.

At larger distances z, the TIP begins to look sharper, when one gets far enough away to see the cone ($\beta = 173$ degrees, shown in black in Figure 5.4a) rather than just the hemisphere. Now it becomes unclear where to measure r from, since it is supposed to be from the surface of the conductor, which is 500 μm below where the TIP cone would come to a point if sharp. If we continue to measure z from the surface in our numerical simulation, the potential rolls off to the expected dependence $\beta = 173^\circ \rightarrow V \sim z^{0.2}$ at around 1 mm from the tip surface (shown in black, in Figure 5.4b). The potential continues to roll off to lower slopes after this point because the cone on top of the TIP shaft is only 2.0 mm tall.

We can now have some confidence in the results of the hyperrelaxation simulation, since they seem to agree with the analytical scaling laws. We can also see that it was important to solve for the potential numerically, because the analytical results are only an approximation due to the blunt shape of the TIP.

5.3 Ion trajectories

Using the voltage and electric field from the hyperrelaxation algorithm, in this section I calculate the trajectories of non-interacting ions. The objective is to find the expected magnification as well as investigate possible distortion in the imaging.

5.3.1 Ion lensing

The ions are initially placed on a grid[2] with variable spacings and extents, at a distance above the TIP corresponding to that of the laser excitation region. After being released from their starting positions in the electric field, the ion positions are then recorded as the ions pass through "detection planes" spaced evenly through the flight path, with the last plane at the MCP surface.

[2]This is unrelated to the hyperrelaxation grid. See Figure 5.5.

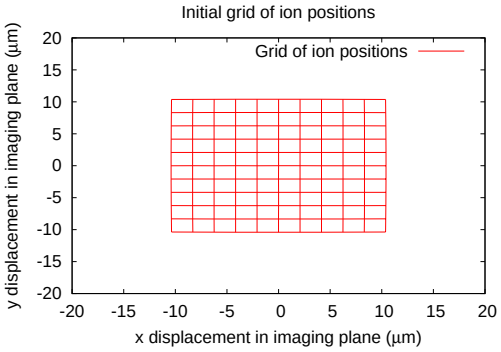

(a) Grid of initial ion positions, starting 300μm above TIP with 2μm spacing between grid points.

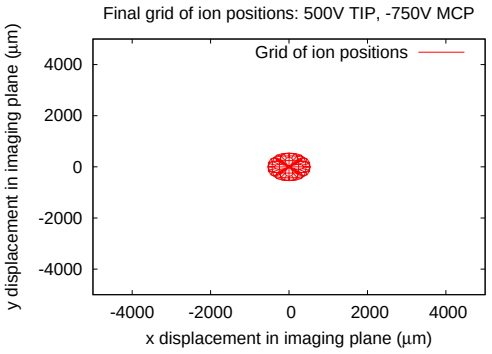

(b) Grid of final ion positions at MCP, for voltage conditions 500 V on TIP and -750 V on MCP.

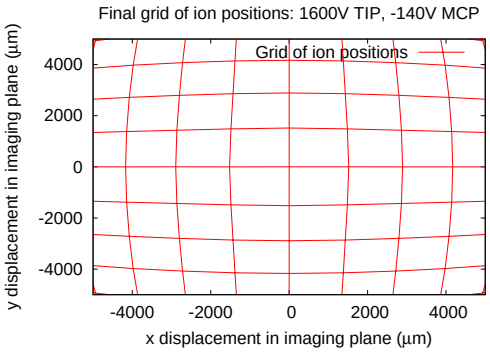

(c) Grid of final ion positions at MCP, for voltage conditions 1600 V on TIP and -140 V on MCP.

Figure 5.5: Results of ion trajectory simulations, showing (a) initial positions of ions above the TIP; (b),(c) final positions of ions on MCP for two voltage conditions used in our experiments. For comparison note that the MCP detector face has a diameter of 18 mm. Figure (c) shows very acceptable imaging conditions, whereas figure (b) is a disaster, with significant distortion and loss of magnification.

Figure 5.5 shows the initial ion distribution at the excitation plane (Figure 5.5a), as well as the resulting distribution on the MCP for two experimentally relevant voltage conditions. Figure 5.5b uses the voltage conditions of the experiments in Chapter IV, while Figure 5.5c uses the voltage conditions from the experiments in Chapter VII. The starting distance of 300 μm above the TIP is chosen to correspond to the experiments of Chapter IV.

For most of the ten voltage conditions simulated (of which only two are shown in Figure 5.5), there is only slight/minimal barrel distortion[3] in the imaging. This

[3]Barrel distortion is a term from geometrical optics which indicates that image magnification decreases with distance from the imaging axis. This is as contrasted with pincushion distortion, where magnification increases with

is the case for Figure 5.5c, which shows very desirable imaging conditions. For only one simulated set of voltages is there significant distortion, which is shown in Figure 5.5b. The distortion causes the edges of the image to fold over slightly for initial displacements of > 6 μm from the imaging axis, which would be a disaster for imaging anything larger than a radius of 6 μm. This occurs for voltages settings of 500 V on the TIP and -750 V on the MCP, which cause strong refocusing of the grid near the MCP (as we will see in Figure 5.6). Because these are the voltage settings used for the work in Chapter IV, it is possible that in that experiment we had some distortion. However, images of the excitation region defined by the 480 nm laser beam (cf. Figure 3.2) do not show barrel distortion even remotely resembling Figure 5.5b. When experimentally measuring the magnification as described in Chapter III, I translated the beam laterally over 40 μm and there was no curvature of the image of the beam. This stands in contrast to the highly curved edges of Figure 5.5b for displacements of only 10 μm off the imaging axis. This is a significant disagreement between the simulation and experimental observations. It is possible that the curvature seen in the simulation is not present in the experiment due to the square (rather than circular) cross section of the guide tube. The fringe fields at the end of the tube may cause ion trajectories to "reflect" from a plane rather than a circle, eliminating curvature. However, when translating the 480 nm excitation beam laterally I still did not see the motion of the ion image reverse direction on the MCP. A possible reason for this discrepancy will be given in Section 5.3.3.

5.3.2 Magnification

To display the ion trajectories in their flight from the TIP to MCP, a representative ion is chosen in Figure 5.6. The ion starts at identical initial positions for several

distance from the imaging axis.

different voltage configurations. The magnification of the ion imaging system can be computed by comparing the ion's distance from the imaging axis before release and after hitting the MCP.

It is clear from Figure 5.6 that a large negative MCP front plate voltage causes significant refocusing of the ion trajectories. The electric fields at the location of the step in potential from the 0 V guide tube to the MCP guard tube causes this focusing. Refocusing can be nearly eliminated either by holding the MCP guard tube closer to ground or by increasing the kinetic energy of the ions so their trajectories are less affected by the refocusing fields. The latter can be achieved by increasing the TIP voltage.

Seeing the dramatic gains in magnification that can be achieved by adjusting voltages, I tried this experimentally. Figure 5.6 shows a comparison of the experimental results with the simulations. The results for (TIP = 500 V, MCP = -750 V) are close, but for other voltages there is a large discrepancy. The discrepancy is investigated in more detail below. One clue may be that the magnification in Figure 5.6 is dominated by the particle trajectories in the vicinity of the MCP. Errors in the geometry used in the simulation could have large effects on the trajectories. Also, the MCP dimensions are not well known; the MCP is very delicate, so we cannot measure it with a ruler or micrometer for fear of damaging its surface. These issues could explain why changing the voltages did not give as much of a magnification gain as expected. However, this cannot be the only issue, as we will see.

In addition to changing voltages, another way of increasing the magnification is to decrease the initial distance from the tip. This is qualitatively in accordance with the argument, based on similar triangles, that the magnification should be roughly the ratio of distances of TIP to MCP and TIP to excitation region. Based on simulations,

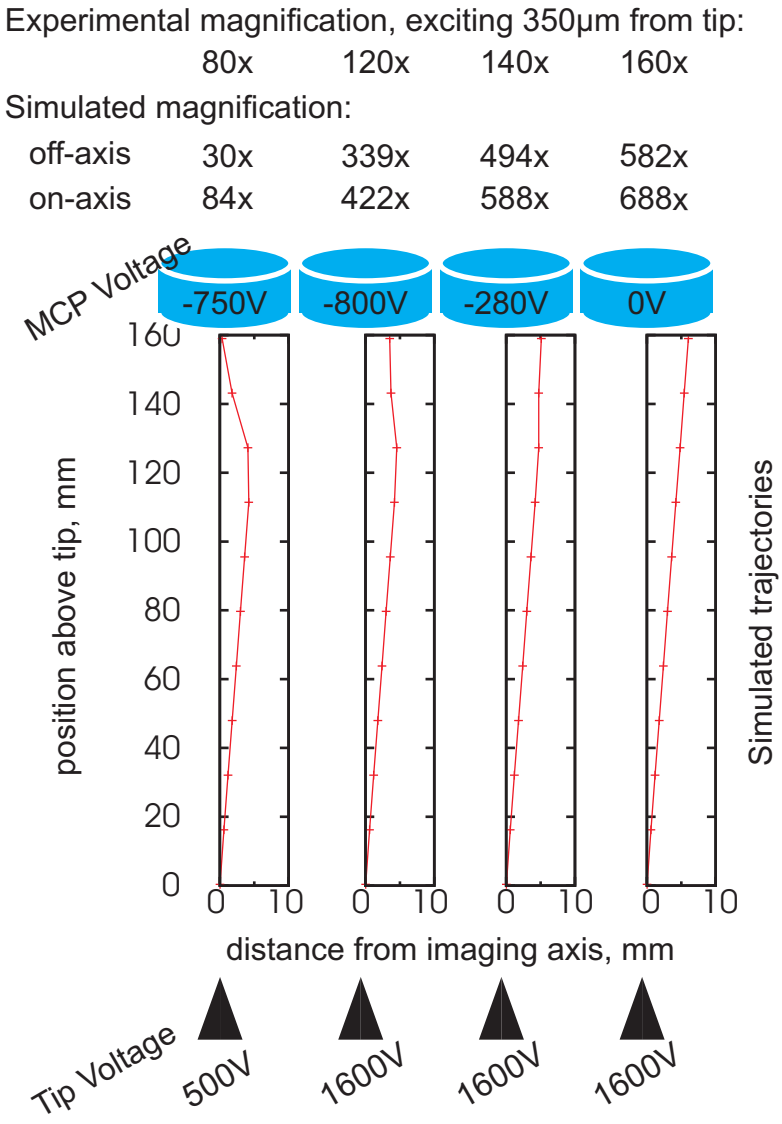

Figure 5.6: *Middle plots:* simulated ion trajectories for four different voltage settings. The voltages on the TIP are labeled below the trajectories, and voltages on the MCP are labeled above. The trajectory shown is for a particle started 10 μm from the imaging axis. *At the top*, I compare experimental and simulated magnifications. The two sets of magnifications given for simulations correspond to two individual-particle trajectories. The high magnification is for a trajectory close to the imaging axis, starting the ion at 2 μm off-axis. The low magnification is for a trajectory further off axis, starting the ion at 10 μm off-axis. The difference in these numbers is due to barrel distortion.

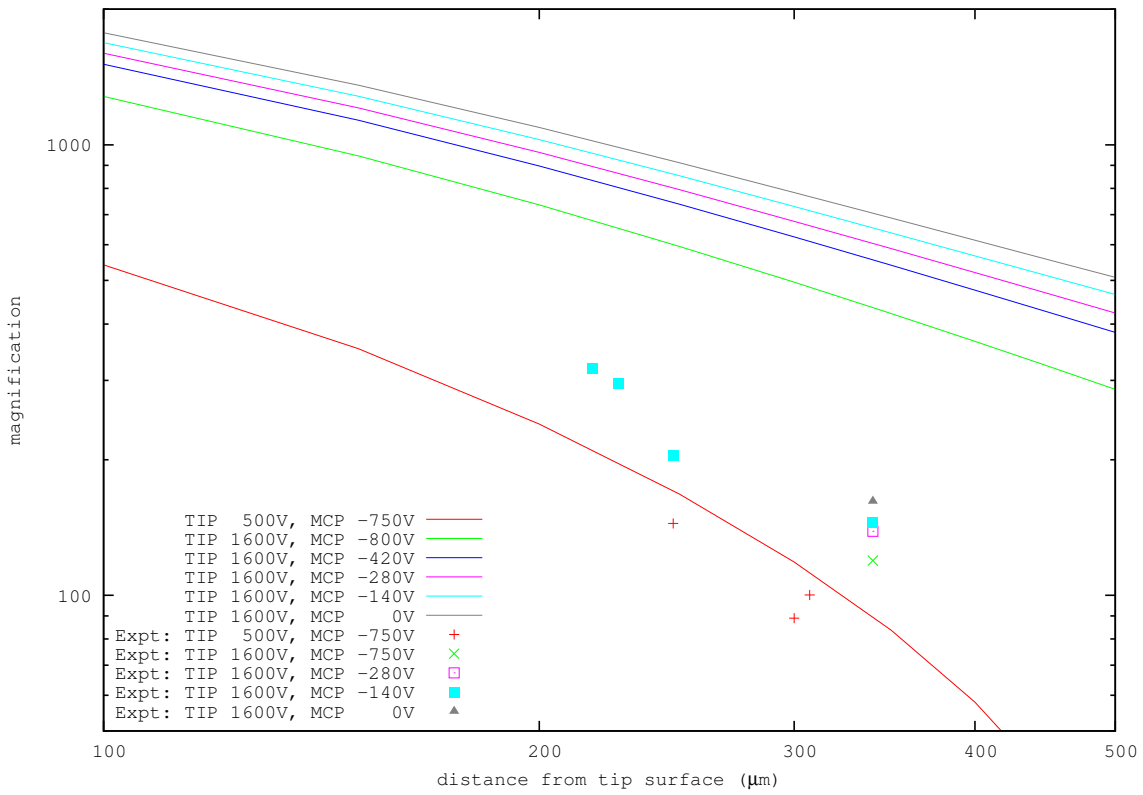

Figure 5.7: Magnification as a function of excitation region position (distance above the TIP), for different TIP and MCP voltage settings. Simulation results are shown as curves; experimental data is shown as points.

the magnification actually scales inversely with distance from the *center of the hemispherical cap* on the TIP, which is $\gtrsim 60$ μm below the TIP surface; see Figure 5.1. (This holds when there are no refocusing effects from the MCP, e.g. for 1600 V on the TIP and 0 V on the MCP.)

The simulations shown in Figure 5.7 capture how the magnification depends on all these parameters. The distance is plotted from the TIP surface, rather than the center of the hemispherical cap, for easy comparison with experiment; experimental magnification measurements are also shown. Experimental data (points) and simulation results (lines) share the same color if they have identical voltage conditions. In the simulation, reducing the MCP potential and increasing the TIP voltage helps the magnification drastically. However, the gains shown in the simulation were not

completely realized experimentally.

There is reasonable agreement between simulation and experiment for the voltage conditions of 500 V on the TIP and -750 V on the MCP. This holds for a range of distances from the TIP. However, all other measured magnifications are about a factor of 3.5x lower than simulations predict. It is particularly troubling that the cases for (TIP, MCP) = (1600V, 0V) and (1600V, -140V) do not agree with simulation, since with such a low voltage on the MCP the ions have straight trajectories. Thus, the only geometry that matters is that near the TIP and merely the distance to the MCP, not the geometry of the MCP guard tube (which is harder to measure, as noted above). The TIP dimensions are known, and recently we have been able to measure the distance from the TIP to the excitation plane with an accuracy of 10 to 20 μm by shadow imaging of an optical dipole trap (see Chapter VI). This leads one to suspect that the potential generated by the TIP is not as expected. In Section 5.2.3 we checked the hyperrelaxation algorithm against analytical results, so the problem is not obvious. Another guess might be that the discrepancy is due to time dynamics of the $\sim$ 50ns-rise-time field ionization pulse. However, the cluster of data in Figure 5.7 that was taken at 340 μm above the TIP for a variety of voltage conditions (including 1600V, 0V) was measured using a high-voltage power supply connected directly to the TIP, with no high-voltage switch, giving a constant voltage over time. The time-dynamics of the field ionization therefore cannot be the source of disagreement.

5.3.3 Sources of discrepancy

In the preceding sections, I have proposed and rejected a number of possible sources for the discrepancy between the simulated and experimental results. Here I collect a few of the most likely candidates.

First I address the case of (TIP = 500 V, MCP = -750 V), shown in Figure 5.5b and the left of Figure 5.6. The refocusing of the ion trajectories is primarily caused by the fringe fields at the transition from the guide tube to the MCP guard tube. The geometry of this transition region is critical. I varied the size of the guide tube in test simulations to see the effect on magnification. All simulations presented so far used a guide tube diameter of $2 \times \mathrm{ra} = 14.1$ cm, as marked in Figure 5.1. If instead I change the simulation's guide tube diameter to match the side length of the experiment's square guide tube ($2 \times \mathrm{ra} = 12.5$ cm), the simulated magnification can be reduced by $\sim 30\%$.

The sensitivity shown by this calculation suggests another potential source of discrepancy. In the experiment, there is a gap between the guide tube and the guard tube. The end of the guide tube is offset from the end of the guard tube both in r and in z. (The r offset is roughly known based on radial dimensions; the z offset is unknown.) In the simulation, the guide tube and guard tube are assumed to meet at the same z, and the gap between them in r is filled by a ring with voltage set to ground. This will change the fringe fields that focus the ions near the MCP.

For the case of (TIP = 1600 V, MCP $\approx$ 0 V), there is no significant voltage step between the guide tube and MCP guard tube. There are therefore no fringe fields which could cause trouble in the model. For this case, it is unclear at this date where the discrepancy between simulations and experiments comes from.

Given the discrepancies, I am inclined to believe the experimental calibrations. It is unlikely that the experimental calibration could be a factor of 3.5 low, as this would suggest the blockade radius is a factor of 3.5 smaller than that measured in Chapter IV.

5.4 Ion interactions and autocorrelations

In using ion imaging to measure a Rydberg blockade, there is legitimate concern that ion-ion repulsion during the time of flight to the MCP could cause an anticorrelation in ion positions on the MCP, independent of the dynamics of the original Rydberg atoms. This would lead to a false blockade signal. In this section, we establish that we could not have seen effects from ion-ion repulsion in our early experiments, and we discover under what conditions we would be more likely to see these effects.

Despite the difficulty in properly predicting magnification ratios, we proceed to simulate the experiment more completely, adding the Rydberg excitation blockade as a hard-sphere non-quantum effect and adding Coulomb repulsion during ion flight.

For realistic experimental count rates and excitation volumes (6-10 Rydberg atoms in a $9 \times 9 \times 50$ μm volume), we find that in the simulation Coulomb repulsion effects do appear in the autocorrelation function (Figure 5.8). The central void (white) shows no ions detected within some minimum distance of each other. This feature, which is due to the ion repulsion, is not present in our data.

Our experimental autocorrelations, as described in Chapter IV and shown in Figure 4.2, have a central black spot due to the autocorrelation of a blip with itself. We called this the "self-term." This feature is not present in the simulations because the simulations treat ions as point-sized objects, which are detected at a point-sized location on the MCP. In the experiment the blips on the MCP (fitted to a Gaussian) have a radius (σ) of 1.8 pixels as detected by the camera, which is 1.8 pixels $\times$40.4 (μm on MCP)/(pixel on camera) = 72 μm on the MCP. This sets the resolution of the MCP as discussed in Chapter III. The autocorrelation of this Gaussian will give a "self-term" with radius $\sqrt{2}$ larger, or $\sim$ 100 μm in distance units at the MCP. To be visible, a void from Coulomb repulsion would have to be larger than this on the

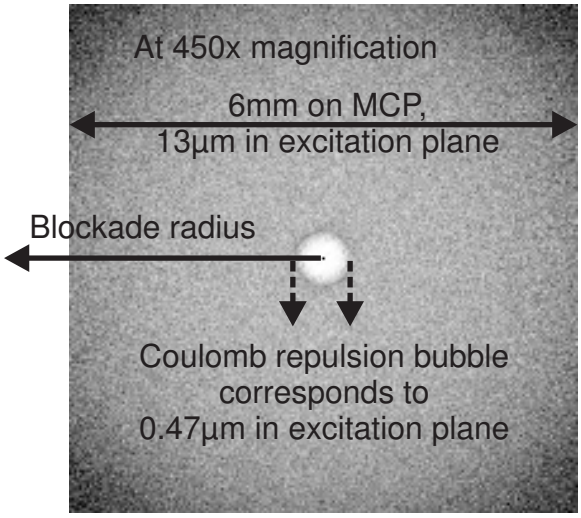

Figure 5.8: Autocorrelation of ion positions on MCP, from simulation. Imaging conditions are 1600 V on the tip and -280 V on the MCP. Note at this magnification the blockade radius now covers the entire image, and the excitation region is larger still. Also note the lack of a large "self-term" (black dot) in middle, which is present in the experimental data (see text). Its presence (and size) in experiment will make the Coulomb effect difficult to see.

MCP.

For a fixed TIP voltage, the Coulomb feature's size in the autocorrelation scales with magnification. With the TIP at 1600 V, as simulated here, a magnification of 220x would be required to make the Coulomb feature the same size as the "self-term." We have exceeded this magnification factor experimentally, but not by enough to clearly see the Coulomb feature. Alternatively, reducing the TIP voltage would increase the relative effect of the Coulomb repulsion in the initial ion cloud expansion and make the Coulomb bubble visible at lower magnification. Other simulations show 500 V on the TIP (and 0 V on the MCP) would give a requirement of $\sim$ 130x magnification to make the Coulomb bubble the same size as the "self-term." This may be feasible.

Other considerations may make the Coulomb feature more difficult to see, indicating that the required magnifications quoted above are lower limits. Not all Rydberg atoms ionize simultaneously in the ionization field, for several reasons. First, the

electric field from the TIP during field ionization is inhomogeneous, which leads to the ionization field being reached by different atoms at different times. Second, the ionization process is due to tunneling and thus has a random component to its timing. If ions are produced at different times, they will have larger initial separations and thus smaller Coulomb repulsion. In the extreme case they will stream one-by-one to the MCP, rather than traveling as an ion-bunch, completely eliminating the Coulomb effect. We do not expect this extreme case, but in general we would expect the Coulomb bubble to be harder to see than quoted above.

In the end, we have not made an attempt to see this Coulomb bubble as ultimately it is scientifically uninteresting. The most important result of these simulations is that the Coulomb effect is not significantly affecting our experimental measurements of the Rydberg-Rydberg correlation function, because it is largely obscured by the "self-term".

CHAPTER VI

Optical Dipole Trap Implementation and Characterization

6.1 Motivation

As seen in Chapter V, moving the Rydberg excitation position closer to the TIP is an effective way to increase magnification in the ion imaging system. In the experiments described in Chapter IV we could not move the excitation position closer due to lack of atomic density in this region. The solution we implemented was two-fold. First, we added an optical dipole trap (ODT) to collect denser atom samples near the TIP. Second, we removed the wire mesh that originally covered the electrode apertures.[1] The wire mesh was preventing the implementation of the ODT [2] , and it also turned out that MOT performance itself improved considerably when the mesh was removed.

In this chapter I describe the implementation of the ODT in the experiment, as well as the lineshape of the resulting Rydberg excitation spectrum which is peculiar to this experimental setup.

[1] Removing the mesh did not increase the effect of residual static or dynamic stray electric fields.

[2] Actually, initial attempts to find the ODT using a 7 W beam caused the wire mesh to glow like a light-bulb filament, depositing metal on the inside of the vacuum chamber windows and also partially melting the inside of the window. This setback led to the removal of the mesh.

6.2 Optical dipole traps (ODTs)

Typically an optical dipole trap is realized for an atomic species by focusing a high intensity laser beam that is far detuned from any atomic transition. The large detuning reduces scattering of the laser beam by the atoms. This nonconservative part of the electric dipole interaction is thus minimized, and the conservative part becomes dominant [66].

6.2.1 Shift of ground state

An optical dipole trap operates based on the electric-dipole interaction between an optical electric field and an induced atomic dipole moment [67]. To calculate the interaction strength we can use complex notation and take the electric field as[3]

$$\mathbf{E}(\mathbf{r},t) = Re\left\{\tilde{\mathbf{E}}(\mathbf{r},t)\exp(-i\omega t)\right\} \quad . \tag{6.1}$$

We can write the induced dipole as

$$\tilde{\mathbf{p}} = \alpha\tilde{\mathbf{E}} \tag{6.2}$$

where α is the complex polarizability, which depends on the driving frequency ω. The interaction energy is then

$$U_{dip} = -\frac{1}{2}\langle \mathbf{p}\cdot\mathbf{E}\rangle = -\frac{1}{2\epsilon_0 c} Re\left\{\alpha\right\} I(\mathbf{r},t) \quad , \tag{6.3}$$

where the angular brackets denote the time average over the rapidly oscillating terms, the field intensity is $I = \frac{1}{2}\epsilon_0 c|\tilde{\mathbf{E}}|^2$, and the factor $\frac{1}{2}$ takes into account that the dipole is induced, not permanent. If the light intensity is not uniform in space, as in the case of a focused laser beam, then the atoms can be trapped in this conservative potential.

[3] Grimm et al. [67] does not use this convention and thereby disagrees with Jackson [65] and Berman and Malinovsky [66], leading to his different equation for the intensity I.

6.2.2 Shift of excited states

A semiclassical treatment shows that the above energy shift of the atomic ground state is caused by a coupling to excited states by the laser field. In a two-state system ($|1\rangle$, $|2\rangle$), the ground state energy is shifted by

$$U = \frac{|\Omega(\mathbf{r},t)|^2}{2\Delta} \tag{6.4}$$

where $\Omega(\mathbf{r},t) = \wp\tilde{E}(\mathbf{r},t)/\hbar$ is the transition Rabi frequency (with $\wp$ the atomic dipole moment operator), and $\Delta = \omega - \omega_0$ is the detuning of the laser from the atomic resonance. For a z-polarized light field, the atomic dipole moment operator is $\wp = e\langle 1|\hat{z}|2\rangle$ (with $\hat{z}$ the z-component of the position operator). For negative (red) detuning in Equation 6.4, an attractive potential is formed. This is equivalent to the shift in Equation 6.3, and simply represents a different method for calculating the same thing (assuming the applicability of the two-state semiclassical model). In the two-state model, the excited state is shifted by the same energy as the ground state but with opposite sign.

The excited state shift is important in shadow imaging directly out of a dipole trap with the trapping light still on.[4] Other experiments in the Raithel lab have historically turned off the ODT trapping light in order to do shadow imaging, so that the $5S \rightarrow 5P$ transition imaged by the probe beam is not shifted in frequency by the trapping light. Due to space constraints [5] I do not switch the ODT light and therefore probe a shifted $5S \rightarrow 5P$ transition. Resonance with the transition is then determined by tuning the probe frequency to achieve the strongest absorption. An additional benefit here is that the MOT atoms are not in resonance with the probe,

[4] It is worth noting that in a system with more than two states (such as Rb), the shift of the ground and excited states will no longer be equal; for ^{85}Rb, the shift of the $5P_{3/2}$ state is approximately 2/3 of the shift of the $5S_{1/2}$ ground state.

[5] There is no room on the laser table for an AOM to switch a 10 W 1064 nm laser beam.

so they do not need to be removed before shadow imaging in order to see the dipole trap. An example shadow image is shown in Figure 6.1.

6.2.3 Shift of Rydberg states

An ODT also shifts the energies of Rydberg states, though through an entirely different mechanism. Rydberg electrons are sufficiently loosely bound to the atomic core that for the interaction with a laser field far from any atomic transition the electrons can be considered quasi-free. In this case, the electron experiences a ponderomotive potential due to the laser field [6]. The ponderomotive potential is the time-averaged kinetic energy of a free electron oscillating in an electric field. It results from the quiver motion of the electron at the optical frequency. For the electric field defined in Equation 6.1 the ponderomotive (quiver) energy of an electron is

$$U_Q = \frac{e^2|\tilde{E}|^2}{4m_e\omega^2} \tag{6.5}$$

where $-e$ and m_e are the electron charge and mass, respectively.

In general, the ponderomotive energy shift of a Rydberg level must be calculated by averaging the ponderomotive shift over the Rydberg electron wavefunction. This is important if the laser field has spatial intensity variations on a scale comparable to the Rydberg wavefunction. This is the case for a high-n Rydberg atom (recall $n = 60$ has $\langle r \rangle = 0.29$ μm; see Table 1.1) in an optical lattice (period 0.532 μm for 1064 nm trapping light). However, for a dipole trap focused to a Gaussian beam parameter of $w_0 = 22.5$ μm as in my experiment, one can assume the Rydberg atoms are point-sized compared to the spatial variation of the free-electron ponderomotive shift.

Recognizing that in general one can write the energy level shift of an object in

terms of its polarizability,

$$U = -\frac{1}{2}\alpha|E_{rms}|^2 \tag{6.6}$$

one can write the polarizability of a Rydberg atom as [68]

$$\alpha_{Ryd} = -\frac{e^2}{m_e\omega^2} \tag{6.7}$$

Note the negative polarizability means the Rydberg atom has a higher energy in an oscillating electric field, so it is repelled from e.g. the focus of a laser beam.

6.2.4 Shift of the ground to Rydberg transition

When laser-exciting Rydberg states in an ODT, the transition frequency is shifted due to the ground state and Rydberg state energy level shifts.[6] At a given position we can calculate the shift of the transition energy by using the polarizabilities of the ground and Rydberg states. Here I give calculations for ^{85}Rb for 1064 nm trapping light.

One can estimate the dynamic polarizability of the ground state based on the static polarizability. [69] states the dynamic polarizability $\alpha_0(\omega)$ of the ground state is related to its static polarizability α_0 by

$$\alpha_0(\omega) = \frac{\omega_0^2\alpha_0}{\omega_0^2 - \omega^2} \quad , \tag{6.8}$$

where ω_0 is the resonant frequency of the lowest-energy transition from the ground state (the D_1 line). This approximate expression is valid for light detuned far to the red of the D_1 line. Using the static polarizability [69], [70] $\alpha_0 = h \times 0.079389\frac{\text{Hz}}{(\text{V/cm})^2}$ yields $\alpha_0(1064nm) = h \times 0.1801\frac{\text{Hz}}{(\text{V/cm})^2}$.

Alternatively, one can use a value for the Rubidium ground state polarizability that is theoretically calculated especially for 1064 nm light [71]: $4\pi\epsilon_0 \times 711.4a_0^3$ in SI

[6] For off-resonant two photon excitation to the Rydberg state we do not need to consider the shift of the 5P state. We used off-resonant excitation for all experiments with the ODT; see Chapter VII. For resonant excitation through the 5P state one would need to tune the lower transition laser to the shifted $5S \rightarrow 5P$ transition.

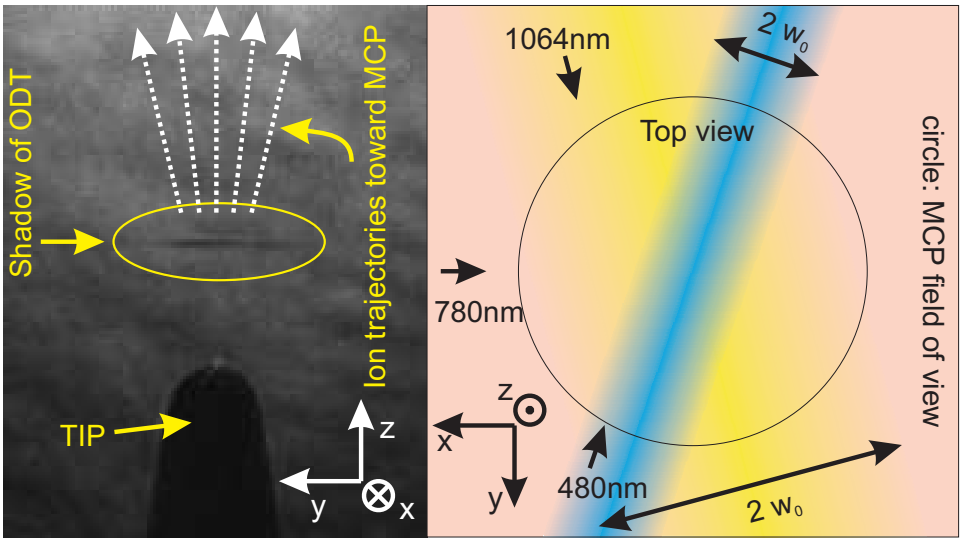

Figure 6.1: Experimental geometry after the introduction of the ODT. *At right* is a top view showing the crossing of the 780 nm, 480 nm, and 1064 nm beams as well as relative focal spot sizes. The $2 \times w_0$ widths are marked for the 480 nm and 1064 nm beams. The black circle shows an estimate of the field of view of the MCP in the excitation plane (radius 25 μm), based on simulation results in section 6.4.2. *At left* is a shadow image showing the position of the ODT above the TIP, as well as a sketch of the first few hundred microns of the ion trajectories toward the MCP.

(MKSA) units. Then, $\alpha_0(1064nm) = h \times 0.1766 \frac{\text{Hz}}{(\text{V/cm})^2}$ The Steck estimate is quite close.

For the polarizability of the Rydberg state, we plug in ω for 1064 nm trapping light and rewrite in a form like that for the ground state: $\alpha_{Ryd} = 4\pi\epsilon_0 \times 545 a_0^3$.

Using these polarizabilities we can calculate the shift of the ground-to-Rydberg transition:

$$\Delta U \equiv U_{Ryd} - U_{5S} = -\frac{1}{2}\Delta\alpha \frac{I}{c\epsilon_0} \tag{6.9}$$

where

$$\Delta\alpha \equiv \alpha_{Ryd} - \alpha_0 = -4\pi\epsilon_0(545a_0^3) - 4\pi\epsilon_0(711a_0^3) \quad . \tag{6.10}$$

Note that $\Delta\alpha < 0$, so $\Delta U > 0$: the transition is blue-shifted in the ODT.

6.3 Experimental implementation

With the addition of the ODT, the experimental geometry has changed somewhat from that used in Chapter IV. The new geometry is shown in Figure 6.1.

As in the experiments of Chapter IV, we start with a MOT of ^{85}Rb atoms and produce Rydberg atoms via a two-step photoexcitation using 780 nm and 480 nm laser pulses. Now, however, we use a crossed excitation scheme, bringing the 780 nm beam[7] in from $+x$ (see the directions labeled in Figure 6.1). The 780 nm beam has a Gaussian beam parameter of $w_0 = 0.75$ mm while the 480 nm beam is focused to $w_0 \lesssim 8$ μm. Each has vertical ($\hat{z}$) polarization, to have a consistent atomic quantization axis and achieve maximum count rates. The excitation is detuned from the intermediate $5P_{3/2}$ state by 1 GHz and has a two-photon Rabi frequency of $2\pi \times 2.5$ MHz for the $59S_{1/2}$ Rydberg state.

The ODT beam comes into the chamber at an angle of 15$\pm$2 degrees from the y axis, as depicted in Figure 6.1. The angle between the ODT and 480 nm beams is 34$\pm$3 degrees. The ODT has 4 W of power and a focal spot of $w_0 = 23$ μm, overlapped with the 480nm beam focus.

Bringing the 780 nm beam in from $+x$ allows us to use the 780 nm beam for both shadow imaging as well as the lower excitation. For shadow imaging we place a camera at an imaging port at $-x$ which is relatively close to the atoms. We use an adaptation of a 2-f imaging system, with a 20 cm and a 15 cm lens between the atoms and camera. This demagnifies the image of the ODT onto the camera CCD. With the 6.7 μm pixel size of the Pixelfly camera we then have a resolution of 8.9 μm at the position of the atoms. The ODT shadow is then only a few pixels wide in the

[7] It should be noted that in Chapter IV the 780 nm excitation beam was derived from the MOT laser. Here, we use a separate laser for the 780 nm beam in order to detune 1 GHz from the $5S \rightarrow 5P$ resonance, allowing off-resonant excitation. The frequency flexibility of this laser also allows tuning to resonance with the $5S \rightarrow 5P$ transition for shadow imaging.

CCD image.

The 780 nm probe is frequency shifted with a double-pass AOM setup in order to obtain a frequency that will be resonant with the light-shifted $5S \rightarrow 5P$ transition in the ODT, while still allowing a convenient lock point using saturated absorption. This AOM is also used to pulse the beam; because the beam is not focused through the AOM, the minimum pulse length is relatively long ($\sim 1.4\ \mu$s). This puts a lower limit on the usable excitation pulse lengths.

Also shown in Figure 6.1 is the approximate size of the MCP field of view in the excitation plane. This is relevant to the detected ODT excitation spectrum described in section 6.4.

6.4 ODT spectrum in the TIP experiment

When performing laser excitation of Rydberg states out of an ODT loaded from a MOT, one generally expects to see two spectral features: the first from excitation of atoms still in the MOT, and the second from excitation of atoms in the ODT. The second feature will be spectrally blue-shifted from the first, as per the discussion in section 6.2.4. An example calculated spectrum is shown by the solid blue curve of Figure 6.2. (The details of the simulation will be addressed in Section 6.4.2.) The shape of the spectral feature from the ODT is explained as follows. The spatial distribution of atoms in the ODT is determined by a Maxwell-Boltzman distribution in the ODT potential. Since the probability of occupation of a position varies exponentially with its $5S$ energy shift, and the ground-Rydberg transition is proportional to the $5S$ shift, the spectral feature from the ODT will approximately be a rising exponential up to the ground-Rydberg frequency at the center of the trap.[8] To the blue of this the

[8]Note that one also must account for the number of states at a given energy, based on 1) the geometry and 2) the trapping potential. Specifically for a cylindrical geometry and a harmonic trapping potential (i.e. an ODT near trap center), the spatial factors cancel to give the above result. See Appendix B.

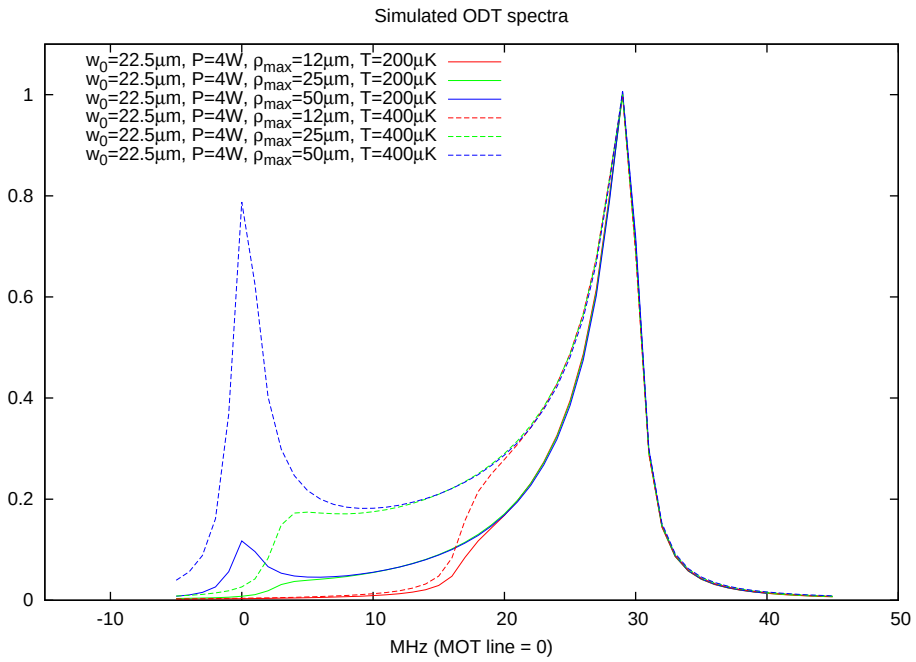

Figure 6.2: Simulated ODT spectra for different excitation volumes and temperatures. Solid lines are $200\mu K$, dashed are $400\mu K$. The frequency at which the ODT spectrum cuts off (on the red side) depends on the excitation volume. Radii of 12μm, 25μm, and 50μm lead to cutoffs at roughly 18MHz, 3MHz, and no cutoff, respectively. All use an ODT with $w_0 = 22.5$ μm.

spectrum falls off continuously due to the finite laser linewidth used for excitation.

In my experiment, we see the MOT line disappear any time the ODT is on. Example experimental spectra are shown in Figure 6.3. In order to eliminate the spectral feature from atoms in the MOT, one normally needs to e.g. turn off the MOT and let the atoms fall away due to gravity, or use a "depumper" beam to pump atoms outside the ODT from the $5S_{1/2}$ $F = 3$ ground state to the $5S_{1/2}$ $F = 2$ dark state. The depumper beam would only be resonant with atoms in the MOT, and would have minimal effect on atoms in the ODT. In our case, the MOT-line disappearance is due to the ODT roughly filling the field of view of the MCP, as depicted in Figure 6.1 and as established below. In essence, Rydberg atoms excited outside of the ODT will not hit the MCP upon field ionization.

In section 6.4.1 I estimate the field of view to show it should have an effect on the

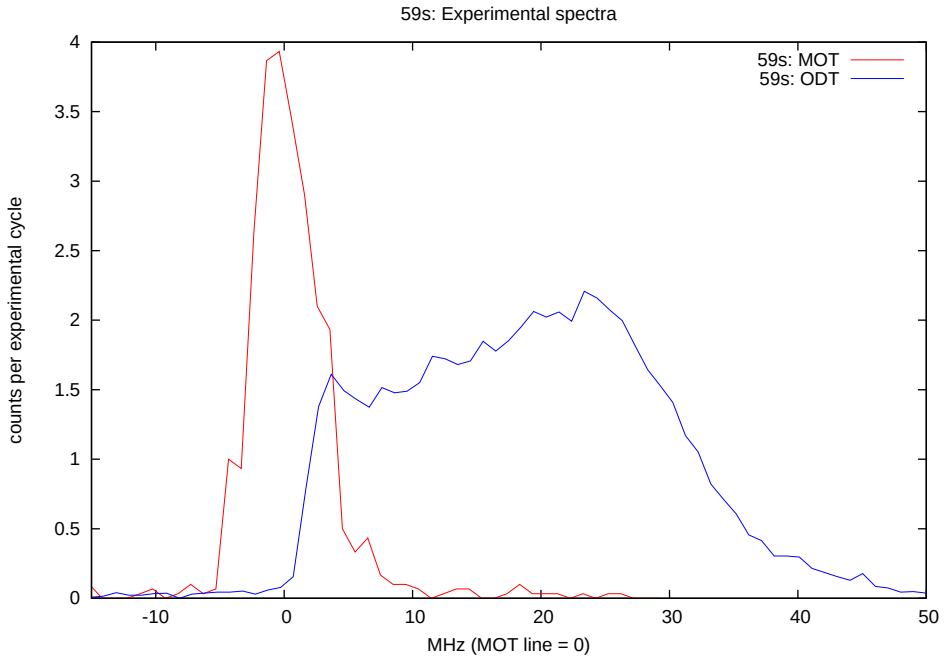

Figure 6.3: Experimental spectra. The red line is the MOT spectrum (with ODT off). The blue line is the excitation spectrum from the ODT. Note that when the ODT is turned on, the MOT peak disappears. Also, the ODT peak does not have an exponential rise from left to right (red to blue) as theoretically expected (see text and Figure 6.2); rather, there is a sharp cutoff on the red side.

Rydberg excitation spectrum out of the ODT. In section 6.4.2 I present simulations that attempt to reproduce the experimental spectra.

6.4.1 Field of view from ion trajectories

Here, I present estimates for the MCP field of view based on ion trajectory simulations. In the experiment giving rise to the excitation spectra shown in Figure 6.3, the TIP voltage was switched to 1600 V and the MCP front plate voltage was -140 V. The excitation position was $\sim$ 200 to 250 μm above the TIP. Ion trajectory simulations for these conditions suggest that an ion more than 10-12 μm off the imaging axis will clip on the guide tube walls and thus will not reach the MCP. This suggests a field of view with radius $\sim$ 11 μm.

We have seen in Chapter V that the trajectory simulations consistently overestimate the magnification in the experiment. We therefore expect the experimental field

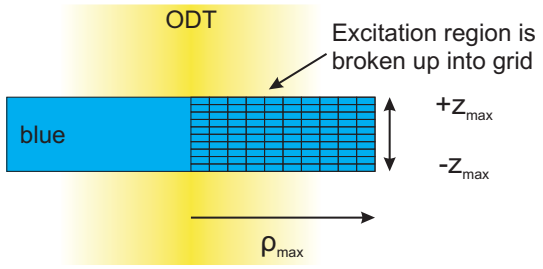

Figure 6.4: The geometry used in the simulation. Excitation from the ODT is done on a grid defined by the parameters ρ_{max} and z_{max}.

of view to be a factor of ~ 3 larger.

It should be noted that this expectation assumes that the ions do have relatively straight trajectories on their way to the MCP, as suggested by the trajectory shown in Figure 5.6 for the above voltage conditions. This assumption seems to be borne out by the results below.

6.4.2 ODT spectrum simulations

To calculate the Rydberg excitation spectrum in the ODT, our simulation breaks up the excitation region into a 2D grid as depicted in Figure 6.4. (Limitations of the 2D geometry are discussed in section 6.4.3.) Transverse to the ODT the grid is set off-center, with radius between zero and ρ_{max}; while longitudinally it is centered running from $-z_{max}$ to $+z_{max}$. We let the width of the 480 nm excitation beam define the width of the excitation region ($z_{max} = w_0$) as shown in Figure 6.4. The dimension ρ_{max} is varied as decribed below.

For each laser frequency, the excitation probability for a grid point is calculated using the light shift of the transition for that location and a Lorentzian spectral profile for the laser. The laser is taken to have a linewidth of 2 MHz (FWHM). Each grid point is additionally weighted by a Maxwell-Boltzman factor, accounting for the relative population of atoms at different points in the trap.

A given field of view in the imaging system can be approximated by adjusting the size of the excitation region ρ_{max} in the simulation. I calculate spectra for ρ_{max} = 12 μm, 25 μm, and 50 μm. To set the temperature I choose values between the Doppler cooling limit (140 μK) and the trap depth. The depth of the dipole trap for parameters of 4 W and $w_0 = 22.5\ \mu m$ is 16.7 MHz (the shift of the $5S$ state), which corresponds to 800 μK. Simulation results for a temperature of $T = 200\ \mu K$ are shown in Figure 6.2 as solid curves. Results for $T = 400\ \mu K$ are shown as dashed curves. All curves are scaled to make their maximum value ≈ 1.

It is clear from Figure 6.2 that the red side of the excitation spectrum is cut off at a frequency that sensitively depends on the size of the excitation volume, ρ_{max}. By comparing this cutoff frequency to the experimental spectra, I can determine the field of view of the MCP in the experiment.

Comparison with experimental spectra are shown in Figure 6.5. The simulated spectra have been rescaled vertically to approximately match with the left side of the experimental ODT spectra. Each simulated temperature has been rescaled independently, but curves of the same temperature have the same scaling. A simulated excitation volume of $\rho_{max} = 25\ \mu$m gives good agreement with the cutoff of the ODT spectrum on the red side, removing the MOT peak. This value of ρ_{max} is about a factor of 2 to 3 higher than predicted by ion trajectory simulations, as we expected based on the discussion of Section 6.4.1. It is also close to the w_0 of the ODT, which is expected as a physical necessity for cutting off the MOT from the field of view.

We do not expect good agreement between simulations and experiment at all frequencies in the spectrum because the simulation completely neglects Rydberg-Rydberg interactions, which lead to saturation of the excitation spectrum. This saturation has been measured for the ODT spectrum. There was little to no saturation

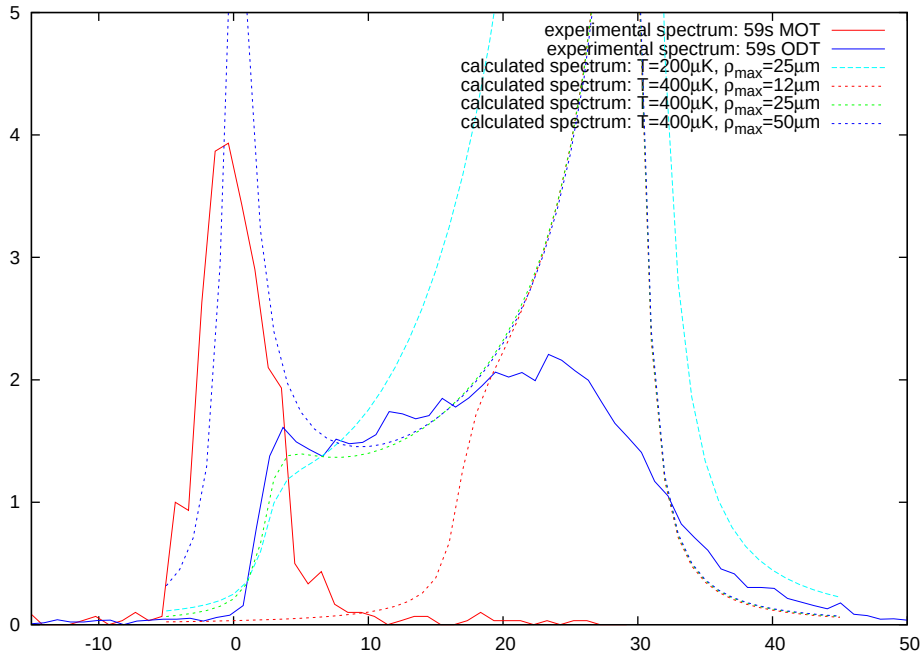

Figure 6.5: Comparison of simulated and experimental ODT spectra. The experimental ODT spectrum is best matched by the simulation with parameters $T = 400\ \mu K$ and $\rho_{max} = 25\ \mu$m.

to the red of the highest point on the experimental ODT spectrum (the "shoulder"), but considerable saturation to the blue of the shoulder.[9] Therefore I expect the simulated spectra to be able to match the slope to the left of the shoulder, but not to the right.

It appears that 400 μK gives better agreement with the slope of the experimental ODT spectra. This temperature is considerably higher than the Doppler cooling limit, but is reasonable based on the following consideration. Since there is no separate laser cooling step in the experiment to cool atoms deeper into the ODT, we can generally expect the temperature of the atoms to be about half of the depth of the trap, due to dynamic loading from the MOT and balancing evaporation from the ODT. The trap depth (as mentioned above) is 800 μK, so half of this agrees with the spectrum-indicated 400 μK. This temperature is thus reasonable.

[9]Here I refer to the shoulder as a convenient reference point; this measurement of the location of onset of saturation is not precise.

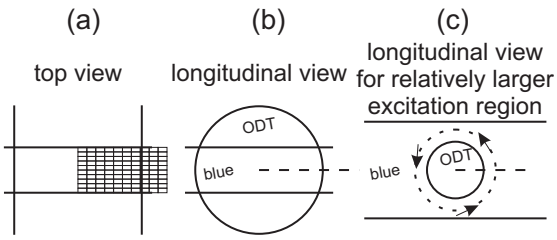

Figure 6.6: The simulation geometry in (a) is a simplified drawing of Figure 6.4, showing the excitation geometry from the top. Fig (b) shows the same in a longitudinal view, along the ODT propagation direction. The dashed line is the planar grid of the excitation region. In (c) the relative sizes of the ODT and excitation region are adjusted. The 2D approximation of using a planar excitation region is now not as good. We should weight grid points by their radius from the ODT axis, in order to account for equivalent positions on a cylindrical shell around the ODT axis all being inside the excitation region. This cylindrical shell is depicted with a dotted circle, with arrows indicating the azimuthal integration required.

6.4.3 Limitations of the simulation

Since the simulation uses a 2D grid, it does not account for the whole 3D excitation volume in the experiment. It is a reasonable approximation if the excitation volume is defined by a beam focused much smaller than the ODT, as in my experiment and as depicted in Figure 6.6(a) and (b). Otherwise, one must account for the larger number of 3D points at larger distances from the ODT axis. Failure to do so will change the shape of the spectrum, overemphasizing points at low radius and undercounting points at large radius. This makes the spectrum appear to be for a lower-temperature gas than that simulated. Attempting to match a simulated spectrum to data will then suggest a higher-than-accurate experimental temperature.

The opposite geometric limit is suggested by Figure 6.6(c). If the 3D excitation volume is much larger in radius than the ODT, and especially if it fills the whole field of view of the MCP, then one can simply weight each 2D grid point by its distance from the ODT axis (in addition to the Maxwell-Boltzman weighting already used) to account for a cylinder of 3D points around the axis.

In general, however, the simulation should be done in 3D and the excitation probability should be weighted by assuming a Gaussian excitation beam. Then the sim-

ulation volume can be set larger than the excitation volume and will not bias the result.

6.5 Conclusion

In this Chapter I have described the implementation of an optical dipole trap in my experiment, for the purposes of increasing ground state atom density and increasing magnification in the Rydberg imaging system. I have also reproduced the basic features of the experimental ODT spectrum in a set of simulations.

By comparing to simulation, I have used the experimental ODT spectrum to make an estimate of the MCP field of view, which corroborates experimental measurements of the magnification factor presented in Chapter V. The experimental field of view is a factor of 2 to 3 higher than in simulations; just as (correspondingly) the experimental magnification measurements are a factor of ~ 3 lower than in simulations from Chapter V. The source of the disagreement is still unknown, but the factor difference is consistent.

Finally, I have used the shape of the ODT spectrum to estimate the temperature of the atoms in the ODT.

The stage is now set for Rydberg imaging experiments in the ODT.

CHAPTER VII

Blockade in an ODT

7.1 Motivation

Having implemented an ODT as described in Chapter VI and improved the experimental magnification as described in Chapter V, my eventual goal is to create and detect a Rydberg crystal (described in Chapter VIII). For present purposes: The production of a Rydberg crystal depends on an adiabatic frequency sweep of the excitation laser across the ground to Rydberg transition, and the dimensions of the crystal lattice depend on the Rydberg-Rydberg interactions. In Chapter VI we have seen that the Rydberg transition frequency is affected by the ODT light, which I cannot turn off during an experimental cycle. It therefore seems prudent to investigate the effect of the ODT on the blockade, before attempting to create a Rydberg crystal.

Before starting this investigation, it is useful to check an even simpler phenomenon. In Section 2.2.3 (and Figure 2.5) I discussed the prediction of Robicheaux and Hernández [47] that the Rydberg-Rydberg correlation function depends quite impressively on the detuning of the excitation laser from the Rydberg transition. It is useful to check the effect of laser detuning because it should be a cleaner implementation of the same underlying physics as light-shifts in an ODT. In the first case we detune the laser from a fixed Rydberg transition frequency; in the second the ODT causes a detuning

of the Rydberg transition (but with spatial variation) from a fixed laser frequency.

In this Chapter I therefore present experimental studies of laser detuning and optical potentials on the Rydberg blockade. Our experimental setup is as described in Section 6.3. To study the effect of laser detuning alone, we do not use the ODT laser.[1]

7.2 Comparison to previous experimental parameters

The excitation region is still surrounded by an electrode package for electric field control. The wire mesh which covered the electrode apertures for the experiments of Chapter IV has been removed, as mentioned in Section 6.1. This has caused a loss of electric field control in the y-direction, due to the large apertures in the y-electrodes (see Figure 3.1b). Despite loss of electric field control in the y-direction, Stark spectroscopy still shows electric fields below the ~ 20 mV/cm level (as discussed in Section 5.2.2) so residual fields have not affected our experiments.

The photoexcitation region is ~ 200 μm above the TIP (rather than the ~ 300 μm used in Chapter IV). After excitation, we perform spatially resolved detection of the the Rydberg atom positions using field ionization, as described in Chapters III through V.

Based on the results of the ion trajectory simulations and the magnification measurements in Chapter V, I now use 1600 V on the TIP and -140 V on the MCP front plate. This reduces refocusing effects and thereby increases the magnification by a factor of ~ 2, compared to the voltage settings of 500 V on the TIP and -750 V on the MCP used for the experiments of Chapter IV. This voltage change, as well as now being able to move the excitation region closer to the TIP, results in a magnifi-

[1] The removal of the mesh, as described in Section 6.1, sufficiently improved the MOT density close to the TIP that the ODT is ironically not needed to improve count rates in blockade studies.

cation of $m \approx 320$, which is ≈ 3.5 times higher than in Chapter IV. The resolution in my sytem is now comparable to the diffraction-limited optical detection schemes mentioned in Chapter II, as described in Section 2.3.3.

7.3 Peak detection algorithm and coarse-graining

To measure the Rydberg-Rydberg correlation function, I first acquire 10 000 CCD images of the MCP phosphor screen, each image showing ion impact positions for a single experimental cycle of Rydberg excitation and ionization. I calculate the Rydberg pair-correlation for each experimental cycle and then average these results, using the general method described in Chapter IV.

In Chapter IV, I calculated autocorrelations of the MCP images directly, with minimal preprocessing to remove noise. An obvious alternative is to use image processing algorithms to detect individual ion positions in the images, and then to calculate the pair-correlation using these discrete positions.[2] This was not done previously because in some cases ions would be detected with separations too small to be resolved by our peak detection algorithm (e.g. see near the top of Figure 4.1a). Higher magnification has now made this limitation unimportant, as the blockade radius is much larger than the minimum detectable ion separation. I now use this peak detection method, as it has the advantage of giving equal weight to each detected ion, regardless of variations in signal intensity on the MCP phosphor due to variabilities in MCP channel or phosphor efficiency. The peak-finding algorithm also allows detection of ions whose signals are only barely above the image noise floor, which effectively doubles the ion count rates in the images, giving much better statistics in the Rydberg-Rydberg correlation.

I have also improved the statistics of the Rydberg-Rydberg correlation measure-

[2]Here I again bring attention to the difference between the autocorrelation and pair-correlation functions, as described in Chapter IV, footnote 2. Calculating the pair-correlation of particles requires distinguishing between separate particles, to remove the self-term.

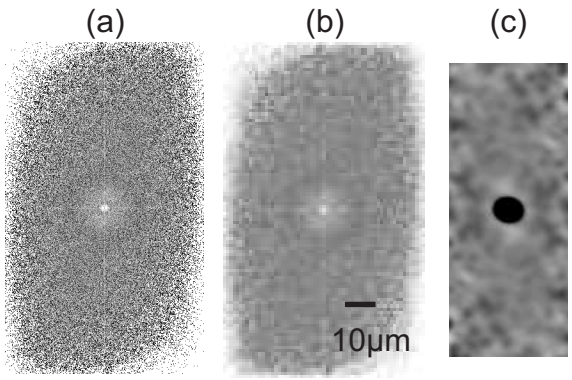

Figure 7.1: (a): Rydberg-Rydberg correlation function ($\bar{A}^1$) measured for the excitation of state $59S_{1/2}$ from the MOT, using the peak detection algorithm to find Rydberg atom positions. (White indicates a value of 0 and black a value of 2, where < 1 indicates anticorrelation and > 1 indicates correlation.) (b): Result of the coarse-graining operation applied to the correlation function in (a). The coarse-graining greatly reduces noise. (c): For comparison: correlation function $\bar{A}^1$ for state $70D_{5/2}$ from the data and the analysis method of Chapter IV. All subfigures share the same physical scale marked by the 10 μm scale bar.

ment by recognizing that the MCP has a lower resolution than the CCD camera. As discussed in Chapter III, blips on the MCP have a Gaussian radius (σ) of 1.8 pixels on the camera. Individual blips therefore cover a region of size roughly 5×5 pixels. We can essentially consider the Gaussian radius to be the size of the measurement error in determining blip locations. In the pair-correlation, then, the displacement between blips is uncertain to about 5 pixels. I therefore calculate a coarse-grained average of the pair-correlation, reducing the linear scale by a factor of 5. This operation is shown in Figure 7.1 (a) and (b). Each pixel in the fine-grained pair-correlation (a) is projected onto the nearest four pixels in the coarse-grained pair-correlation (b) using a pyramid function that preserves normalization. Note that this coarse-graining was inherent in the previous method of calculating the autocorrelation of the image directly, because of the point spread function of each detected ion (the blip radius). With peak-detection, I account for the MCP resolution by coarse-graining. Coarse-graining greatly reduces the noise in the correlation image.

I now describe the specific structures in the correlation function shown in Fig-

ures 7.1 (a) and 7.1 (b), for comparison to the data from Chapter IV shown in Figure 7.1(c). As described in Chapter IV, correlation values indicate the likelihood of finding Rydberg atoms with a given separation vector. A value of 1 indicates no correlation, i.e. the equivalent of random Rydberg positions. Values < 1 indicate anticorrelation, and > 1 positive correlation. The grayscale in Figure 7.1 (and for all other correlation functions in this chapter) is set such that white is 0, and black is 2.[3] With the peak detection algorithm, there is zero probability of finding two different blips within one blip radius σ. In Figure 7.1(a) there is therefore a small central white region of size equal to the blip radius, which is mapped onto a single central white pixel in (b). Outside of this there is a large grey/white region (radius $\lesssim 10$ μm) of reduced probability to detect a second Rydberg atom, due to the blockade effect. Surrounding this there is a dark ring of slightly enhanced probability to detect a second Rydberg atom, beyond which the correlation function goes roughly to 1.

The correlation function for state $70D_{5/2}$ from the data and methods of Chapter IV, shown in Figure 7.1(c), is quite different. The first thing to notice is that the center is black, due to the self-term (which is eliminated via peak detection in (a) and (b)). Second, the self-term in (c) appears much larger than the white blip radius in (a,b). This is due to the factor of ≈ 3.5 less magnification in the experiments of Chapter IV (see Section 7.2). The self-term is so large that it nearly obscures the surrounding white region of depressed probability to detect a second Rydberg atom, which is the signal of the blockade.[4] Outside of this white ring, the correlation function in (c) becomes somewhat noisy due to low count rates. The noisiness of the correlation

[3]Note for comparison that in Chapter IV, Figure 4.2, the grayscale is arbitrary because the autocorrelations pictured there are $\bar{A}$ (see Equation 4.2), not the normalized $\bar{A}^1$ used here (see Equation 4.5). For the data displayed in Chapter IV, only the $I(r)$ curves and Figure 4.1(f) are normalized.

[4]Note that the $70D_{5/2}$ data is the *best*-looking data from Chapter IV.

function has been reduced since the experiments of Chapter IV by: increasing ground-state atom density, increasing 480 nm laser power (by using a different laser), and using the more-sensitive peak detection algorithm to find peaks that are near the noise floor. Comparing Figures 7.1(b) and (c), the benefits are apparent.

7.4 Correlation measurements

Using the above procedure, I measure the Rydberg-Rydberg correlation function for excitation to states $59S_{1/2}$, $66S_{1/2}$, $74S_{1/2}$, $57D_{5/2}$, $64D_{5/2}$, and $72D_{5/2}$. Laser excitation pulse lengths were 5 μs for S-states and 1 μs for D-states, to account for the difference in oscillator strength and make count rates comparable. For some states, excitation rates are low enough that up to half the pictures show fewer than two counts, thereby not contributing to any correlation measurement. I thus use the 5 000 pictures with the highest number of counts for calculating each average pair-correlation. I do this for all states, so that correlation functions can be compared between different states.

For each state, I adjust the 480 nm laser frequency to excite at various frequency points on the MOT spectrum and ODT excitation spectrum. Rydberg-Rydberg correlations are measured at these frequencies.

7.4.1 Excitation from MOT

Typical excitation points on the MOT spectrum are indicated by vertical black lines on the spectrum in Figure 7.2. The excitation frequencies are chosen to be at the peak of the spectrum and the half-max points for red and blue detuning. The spectrum shown is for an S-state. It is asymmetric due to Rydberg-Rydberg interactions; broadening is to the blue, due to repulsive van der Waals interactions.

As mentioned in Section 2.2.3, a laser detuning in the direction of the van der

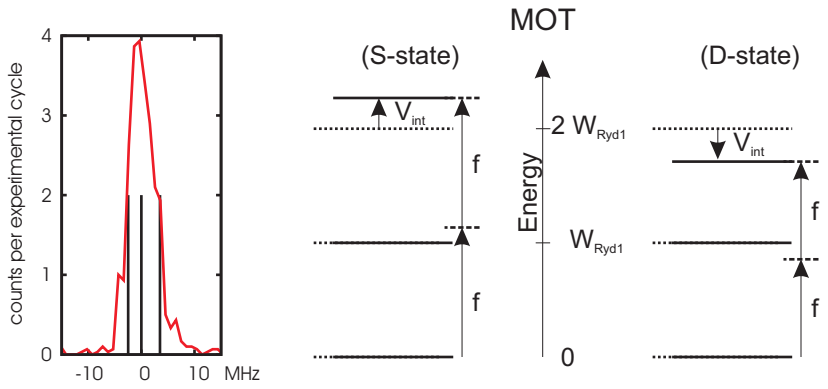

Figure 7.2: *At left:* MOT excitation spectrum for $59S_{1/2}$. The vertical black lines show frequencies at which correlation functions were typically measured: the peak, and the half-max points. *At right:* Level diagrams for off-resonant excitation from MOT. The laser frequency is f, and the energy to excite one Rydberg atom is W_{Ryd1}. Dotted lines indicate energy levels without interactions. Solid lines are energy levels with interactions. Dashed lines show the laser frequency. The diagrams show the directions of detuning of f from W_{Ryd1} which will give a "two-photon resonance" (direct excitation of two Rydbergs) for S and D states. (See text.)

Waals shift can preferentially excite atoms at a given separation. This is depicted in the level diagrams on the right of Figure 7.2. The energy of a single Rydberg atom is labeled W_{Ryd1}. For S-states, the $(N, k = 2)$ energy level (two Rydberg excitations) is higher than $2 \times W_{Ryd1}$ due to repulsive interactions. A detuning of the laser frequency f to the blue of W_{Ryd1} can cause a "two-photon"[5] excitation to the $(N, k = 2)$ state, off resonant past the $(N, k = 1)$ state. For larger laser detuning, a larger interaction energy is needed to tune the $(N, k = 2)$ state into resonance; therefore the two Rydberg excitations will be found closer to each other. The case for D-states is identical, except that the direct $(N, k = 0) \rightarrow (N, k = 2)$ excitation should happen for red detuning of f from W_{Ryd1}.

Normalized pair-correlations $\bar{A}^1$ (see Figure 4.1(f) and Equation 4.5) for excitation to S-states are shown in Figure 7.3. I excite states $59S_{1/2}$, $66S_{1/2}$, and $74S_{1/2}$ using laser frequencies that are on-resonant, red-detuned, and blue detuned. In the figure, we see some dramatic trends. First, the blockade radius is in all cases very well re-

[5] See footnote 5, Chapter II.

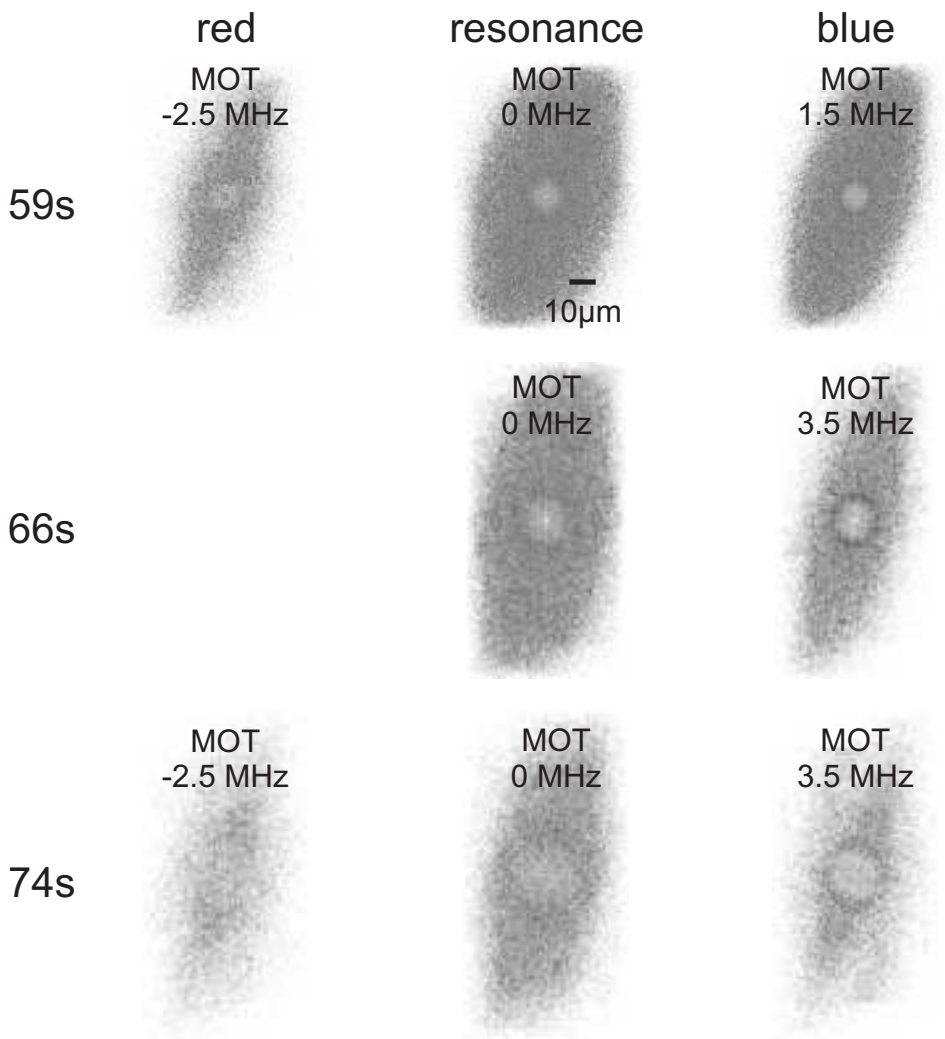

Figure 7.3: Rydberg-Rydberg correlation functions for excitation to S-states from the MOT. The states excited are $59S_{1/2}$, $66S_{1/2}$, and $74S_{1/2}$ (see labels at left). The detuning direction from the MOT resonance is labeled above, and the precise detuning value is labeled on each image. The physical scale is marked on the correlation function for $59S_{1/2}$, on-resonant excitation. The scale is common for all correlation functions. No data was taken for state $66S_{1/2}$ with red detuning.

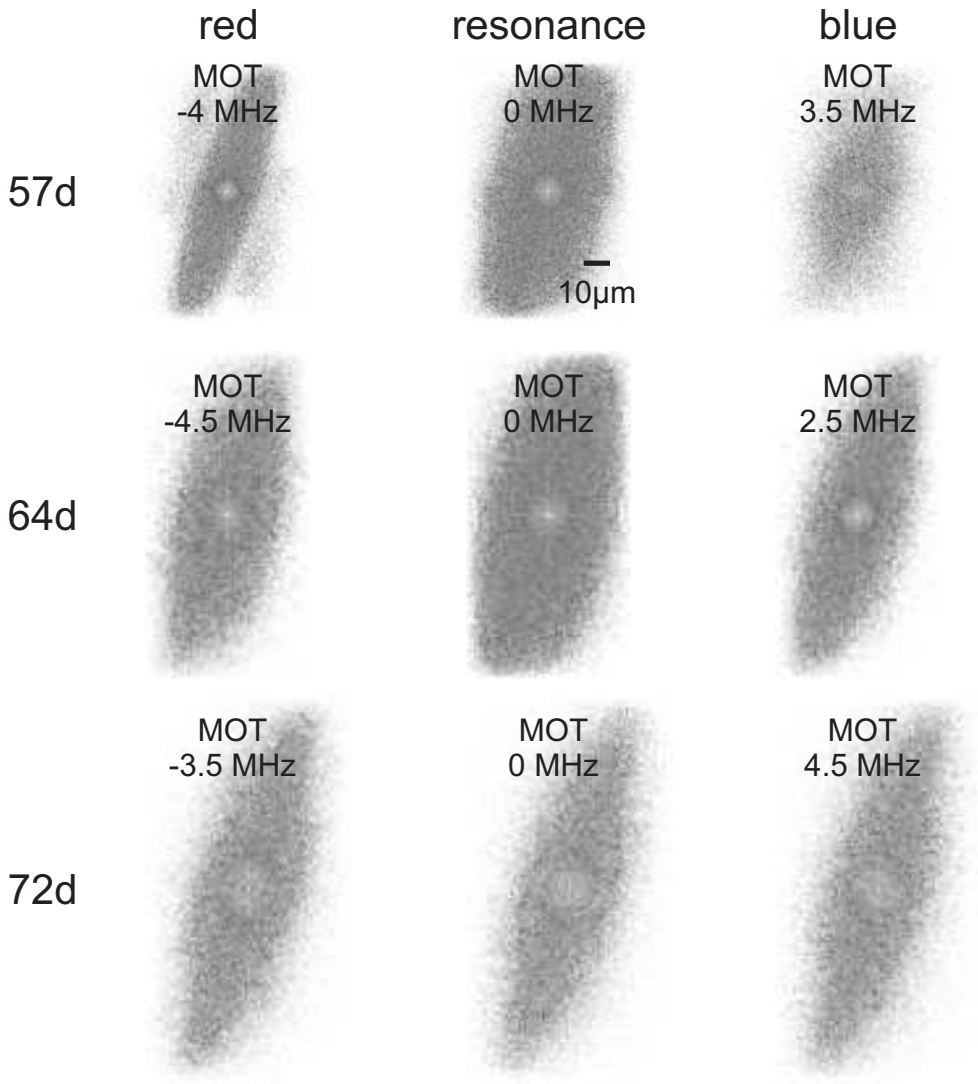

Figure 7.4: Rydberg-Rydberg correlation functions for excitation to D-states from the MOT. The states excited are $57D_{5/2}$, $64D_{5/2}$, and $72D_{5/2}$ (see labels at left). The detuning direction from the MOT resonance is labeled above, and the precise detuning value is labeled on each image. The physical scale is marked on the correlation function for $57D_{5/2}$, on-resonant excitation. The scale is common for all correlation functions.

solved (as compared to the data of Chapter IV). Second, for on-resonant excitation, increasing the n quantum number drastically increases the blockade radius. (Quantitative statements about this will be made in Section 7.5.) Third, we see for blue detuning that there is a dark ring around the blockaded region, indicating enhanced probability for a second Rydberg excitation at this radius. This is in accordance with the predictions of Robicheaux and Hernández [47] described in Section 2.2.3 and above. The ring is not as prominent for state $59S_{1/2}$ as for the other states because the blue detuning is less; this is the one correlation measurement for which I did not excite at the half-max point, but rather about halfway between the half-max point and the peak of the spectrum. Otherwise, the asymmetry between blue and red detunings chosen show the asymmetry of the MOT spectrum, mentioned above.

Figure 7.4 shows similar correlations for the excitation of D-states. Again we see the trend of increasing blockade radius with increasing n. However, there is no clear, consistent trend with respect to laser detuning. Red detuning gives a darker ring for $57D_{5/2}$, as I would expect. But for states $64D_{5/2}$ and $72D_{5/2}$ there is no strong difference between red and blue detuning. Blue detuning may in fact show stronger rings for $64D_{5/2}$. First, I note that Robicheaux and Hernández [47] only make predictions of the correlation functions for repulsive interactions, not attractive interactions. Nonetheless, it makes sense based on the energy level diagram of Figure 7.2 to expect rings for attractive interactions with red detunings. I believe the absence of rings (at red detuning) for states $64D_{5/2}$ and $72D_{5/2}$ is due to electric field control problems during the collection of this data. The $57D_{5/2}$ data was taken later, after these electric field problems were solved. An electric field can cause the excitation of a variety of m_j sublevels in the Rydberg state, due to the quantization axis defined by the electric

field not lining up with the quantization axis defined by the laser polarizations ($\hat{z}$).[6] The different m_j states have different interaction strengths as shown in Figure 2.2, leading to a variety of blockade radii in the system, washing out the expected ring structure for red detuning. Indeed, the $72D$ data may show faint multiple rings for on-resonant excitation, indicating the presence of multiple m_j states.

We have thus seen the "two-photon resonance" predicted by Robicheaux and Hernández [47] for S-states, which is a direct excitation of two Rydberg atoms at a separation that depends on laser detuning. Experimentally, it is interesting to note that this is a four-photon transition, because each Rydberg transition involves both a 780 nm and a 480 nm photon. I will use the evidence of this effect in the interpretation of my data for excitation from the ODT, below.

7.4.2 Excitation from ODT

In a similar set of experiments, I excite Rydberg atoms out of the ODT at different frequency points on the ODT spectrum. A few of these correlation functions for excitation of $59S_{1/2}$ are shown in Figures 7.5(b-d). These correlation functions correspond to the frequency points indicated in Figure 7.5(e) by the vertical black lines at 24 MHz, 32 MHz, and 40 MHz. For comparison, the result for resonant excitation out of the MOT is shown in Figure 7.5(a). The resonant MOT excitation frequency is marked by a vertical black line at 0 MHz in Figure 7.5(e).

With larger detunings, the ring in the pair-correlation both shrinks in radius and grows in intensity. This can be seen both in the images (a-d) and in the plot of the angular averages, (f). At 40 MHz detuning there is a clear second ring in Figure 7.5(d). This is especially clear as the second peak in Figure 7.5(f). I believe this is due to exciting a string of three equally-spaced Rydbergs, with the center Rydberg at

[6] See the discussion in Section 7.5 for the expected selection rules without an electric field.

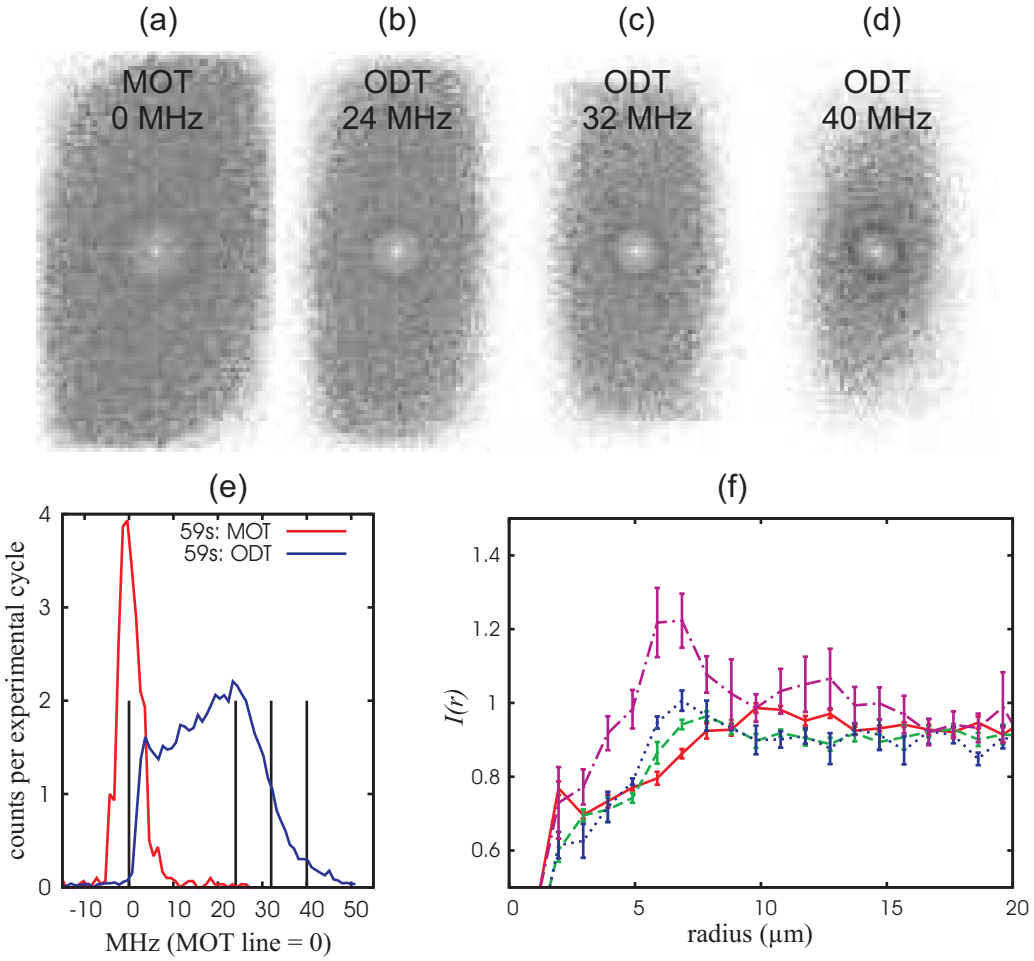

Figure 7.5: (a): Correlation function for resonant excitation out of the MOT, for comparison with ODT correlation functions. (b-d): Correlation functions for excitation out of the ODT, at the indicated detunings from the MOT peak. (e): Spectra for excitation of $59S_{1/2}$ from the MOT (red curve) and ODT (blue curve). Black vertical lines indicate the excitation frequencies used to acquire the correlation functions presented in (a-d). The 0 MHz line is an excitation from the MOT with the ODT off; the other lines are excitation from the ODT. (f): Angular averages of the correlation functions in (c-f), with error bars calculated by the standard deviation of the mean (see text). The curves correspond to correlation functions as follows. Red: (a) MOT; Green: (b) ODT 24 MHz; Blue: (c) ODT 32 MHz; Purple: (d) ODT 40 MHz.

the deepest part (the three-dimensional center) of the ODT. My model for these trends will be presented in Section 7.5, once I show our slightly changed method for measuring the blockade radius in this chapter.

To measure the blockade radius, as in Chapter IV we use curves like those shown in Figure 7.5(f). These are essentially the angular averages of the pair-correlations in Figure 7.5(a-d). More precisely, in the notation of Chapter IV, these curves are

$$I(r_k) = \frac{\int_{S_k} \bar{A} d\phi}{N_p \int_{S_k} B d\phi} \tag{7.1}$$

where ϕ is the angle around the center of the picture, N_p is the number of pictures in the dataset (for normalization), and $\bar{A}$ and B are calculated without coarse-graining. The coarse-graining step is achieved by doing each integral on an annulus (denoted S_k) of width 5 pixels centered at r_k. Note this is similar to the angular average of $\bar{A}^1$ but not identical, due to dividing *after* integration. Locations in B outside the cigar shaped beam have lower count rate (and therefore lower values of $\bar{A}$, B) and are therefore weighted less in this angular average in Eqn 7.1. This will tend to reduce noise by minimizing the influence of pixels at large radius (e.g. $\sim 15\mu m$) outside the excitation beam, without diminishing the influence of pixels at the same radius but still within the excitation beam.

I estimate the error on these $I(r)$ curves for 5 000 pictures by testing the variability of the results for subsets of the dataset. I break the 10 000 picture dataset into subsets of 2 000 pictures, calculate $I(r_k)$ for each, and measure the standard deviation of the mean for each point r_k. This calculation yields the error bars shown in Figure 7.5(f). Because I did not throw out the 5 000 pictures with low count rate when forming these subsets, this standard error of the mean is an overestimate of the error of the points in the plot. The error increases dramatically at large laser detunings due to reduced count rates.

7.5 Blockade radius measurements

I measure the blockade radius r_b for each $I(r)$ curve using the point closest to the origin where $I(r)$ crosses its asymptotic value for large r. (In most cases this is the expected value of ≈ 1, but there is sometimes a deviation from 1 due to low count rates at certain excitation frequencies.) This method is different from that used in Chapter IV, where I measured r_b as the inflection point of $I(r)$. The difference arises due to the new method of peak detection for calculating the correlation function, which slightly changes the shape of the correlation function; an inflection point can no longer be identified on most $I(r)$ curves. The new asymptote-crossing method is suggested by results of a stochastic non-quantum simulation of the excitation-blockade process, similar to that described in Chapter IV. The simulation uses a hard-sphere blockade of specified radius r_b as input. The resulting $I(r)$ curves have asymptote crossings which agree to within $\pm 1 \mu m$ of the input r_b.

Before moving to the ODT, I first measure and predict the blockade radius for each state as excited from the MOT. The predictions are based on van der Waals interactions as described in Chapters II and IV. For the calculations I use interaction strengths from Figures 2.2 and 2.3 (originally from [37]). For D-states I pick $\tilde{W}^{(2)}$ as appropriate for the excitation geometry and laser polarizations described in Section 6.3 for the current experimental setup. With $\hat{z}$-polarized excitation beams I drive π transitions, to excite $5S_{1/2} \rightarrow |nD_{5/2}, m_j = \pm 1/2\rangle$, so I use interaction strengths for $m_j = 1/2$ states. I have an interaction angle of $\theta = \pi/2$ due to the quantization axis being perpendicular to the direction of propagation of the excitation beams, along which the Rydberg excitations will be roughly lined up. Laser linewidths, for use in calculating r_b via Equation 2.10, are chosen to be the inverse of the excitation pulse length. The predicted and measured blockade radii shown in Figure 7.6 agree quite

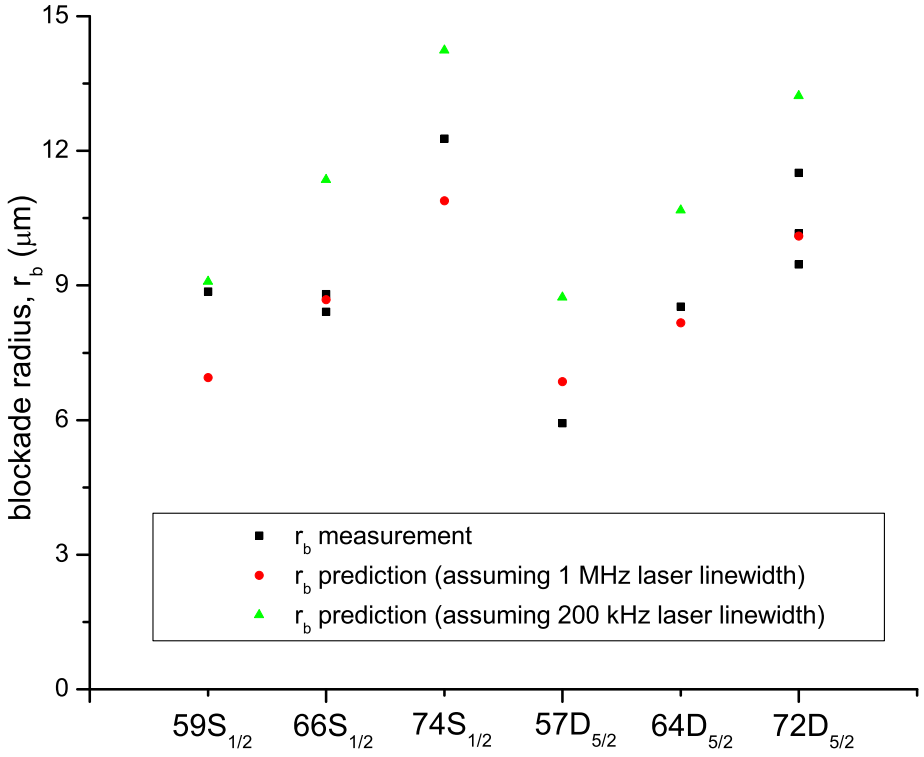

Figure 7.6: Measurements and predictions of the blockade radius r_b for several $nS_{1/2}$ and $nD_{5/2}$ states. Predictions are based on excitation linewidths that are assumed to be equal to the inverse of the excitation pulse time. For S-states with 5 μs excitation pulses this is 200 kHz; while for D-states with 1 μs pulses this is 1 MHz. Predictions using both linewidths are plotted for each state in order to show an expected range for r_b.

well.

I now move to measuring the blockade radius when exciting from the ODT. Measurements are shown in Figure 7.7, as a function of laser detuning from the MOT line, denoted f.[7] Predictions in the figure are calculated using a one-dimensional model which I explain here. In this model I must account for spatially-dependent light shifts of the Rydberg transition in addition to the interaction energy between the Rydberg atoms to correctly predict the blockade radius. The light shifts of the two Rydberg atoms, f_1 and f_2, are determined by the dynamic polarizability of both the $5S_{1/2}$ ground state and the Rydberg state for 1064nm laser light, as described in Chapter VI. For the ground state this is $\alpha_{5S} = 4\pi\epsilon_0 \times 711.4 a_0^3$. [71] The polarizability of the

[7]Note that this is a change in notation from earlier in the chapter where I used f for the absolute frequency of the laser, not the detuning from the MOT line. See e.g. Figure 7.2.

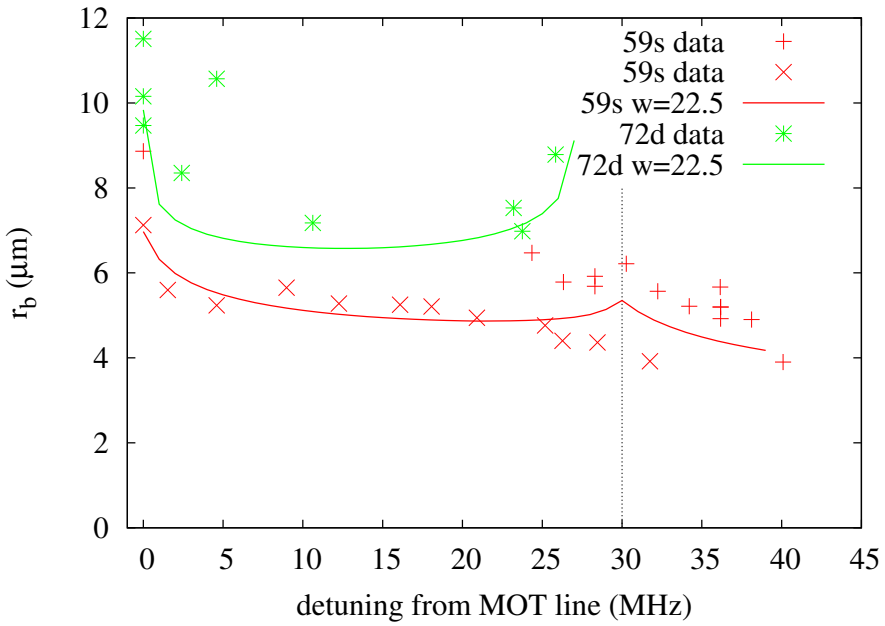

Figure 7.7: Blockade radius (r_b) as a function of laser detuning (f) from the MOT line. Measurements are for exciting states $59S_{1/2}$ (data set 1 (+), data set 2 ($\times$)) and $72D_{5/2}$ ($*$). Solid lines are predictions based on solving Equations 7.2 and 7.3. The vertical dotted line indicates the maximum light-shift of the ground-Rydberg transition (f_{max}), at the 3D center of the ODT.

Rydberg state is calculated via the ponderomotive effect to be $\alpha_{Ryd} = -4\pi\epsilon_0 \times 545 a_0^3$. For energy conservation in the excitation process we have

$$f_1 + f_2 + V_{int}/h = 2f \pm \Delta f \tag{7.2}$$

where Δf is the laser linewidth, and the Rydberg-Rydberg interaction energy is

$$V_{int} = \frac{E_{hartree} \times \tilde{W}^{(2)}(n^*)^{11}}{((x_1 - x_2)/a_0)^6} \tag{7.3}$$

where x_1 and x_2 are the positions of the Rydberg atoms. In this one-dimensional model, the positions are measured transverse to the ODT focus so that the optical potential varies with position x.

We first consider a step-wise excitation of two Rydberg atoms, as shown in Figure 7.8. The first Rydberg is resonantly excited at a position r_1 in the ODT such that the light shift of the transition, f_1, equals the laser detuning, f, from the transition with zero light shift. The position of the second Rydberg is determined by balancing

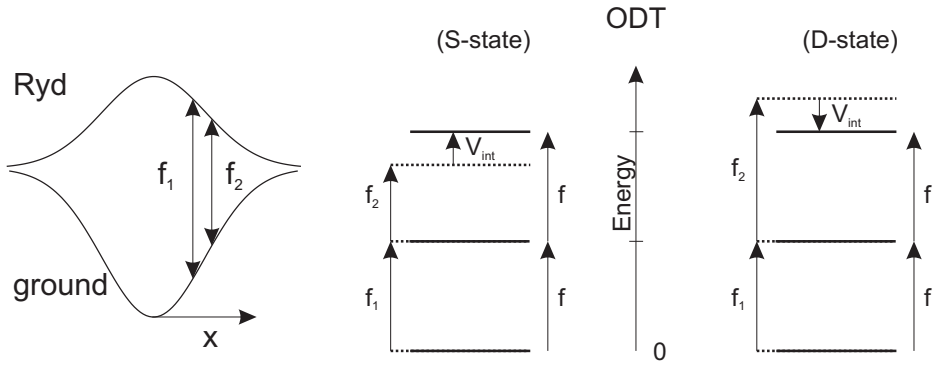

Figure 7.8: *At left:* Light shifts of the Rydberg and ground states in the ODT, as a function of transverse position x. The transition light shifts of two atoms are labeled f_1 and f_2. *At right:* Level diagrams showing stepwise excitation of Rydberg atoms in an ODT, for S-states and D-states. The laser detuning from the MOT line is f. The detuning of the ground-Rydberg transition due to the ODT is f_1 for atom 1, and f_2 for atom 2. For both excitation steps to be resonant with the laser f, for S-states the second atom must be at a location of lower light intensity (so $f_2 < f_1$), as shown at left. For D-states the second atom must be at higher light intensity ($f_2 > f_1$).

its light shift f_2 and the interaction energy V_{int} to yield a second on-resonant transition, solving equation 7.2. There are four solutions, corresponding to $x_2 < x_1$ and to $x_2 > x_1$ for each of the signs in Equation 7.2. In the experiment, only the smallest of these will be apparent in the pair-correlation data. I therefore pick the smallest of the values for $|x_1 - x_2|$ as the predicted blockade radius. My model uses ODT parameters as described for the experimental setup, and has no free parameters.

Intuitively, if the light shift varies rapidly with position near x_1 then the blockade radius will be smaller: it is analogous to having a large laser linewidth. Thus the minimum blockade radius is expected for x_1 at roughly the inflection point of the transverse ODT intensity profile. This explains the variation of r_b with detuning for D-states, shown for $72D$ in Figure 7.7. There is an initial drop in r_b and and an eventual rise when exciting near the center of the trap. We note that exciting a D state at the center of the trap leads to a perfect blockade (only one Rydberg excitation), since a second Rydberg would see a reduced light shift which cannot be compensated by a negative interaction energy; here r_b diverges. This is shown by

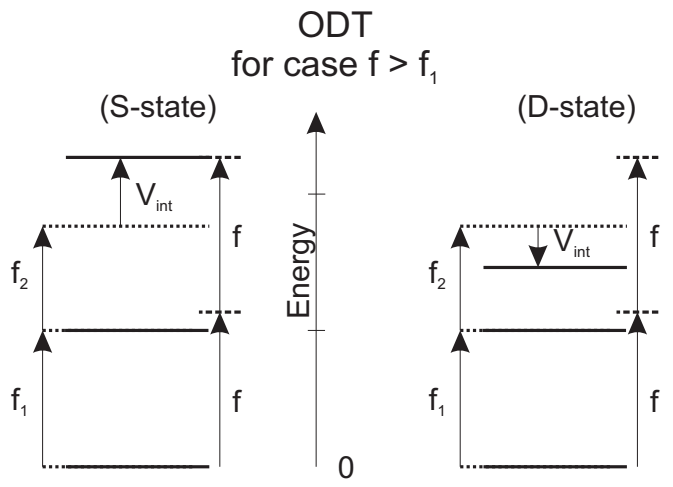

Figure 7.9: Level diagrams for direct two-Rydberg excitation from the ODT, using detuning $f > f_{max}$.

both the data and predictions in Figure 7.7; it is not possible to measure a blockade radius near the trap center, indicated by the vertical dotted line at $f_{max} = 30$ MHz.

For S-states we see that excitation is possible at much larger detunings, and even beyond the expected maximum light shift of the Rydberg transition in the ODT ($f_{max} = 30$ MHz). This is shown in the excitation spectrum in Figure 7.5(e), the correlation functions obtained at 32 MHz and 40 MHz (each > 30 MHz), as well as in Figure 7.7. We model this domain by placing the first Rydberg at the center of the ODT and continuing the calculation as before. The positive V_{int} still admits a solution for equation 7.2, with increased V_{int} and thus reduced r_b. A level diagram for this process is shown at the left of Figure 7.9. Here there is an off-resonant transition directly to the two-Rydberg state, as we saw earlier for excitation from the MOT (Figure 7.2). This process cannot occur in the ODT for D-states, as shown in Figure 7.9.

The cusp in our prediction for S-states (red curve in Figure 7.7) is due to the model's piecewise nature, assuming that off-resonant excitation occurs only when resonant excitation is impossible. In the experiment we expect a smoother transition

between these cases. Thus the rings in Figure 7.5(a-d) smoothly shrink in radius and increase in height, qualitatively shifting in appearance from the on-resonant MOT case in Figure 7.3(middle column) to the off-resonant case (right column, blue detuned).

Our 1-dimensional model captures the essential physics. Despite the fact that there is a dimension in the experiment along which there should be no light shift, there is no obvious anisotropy in the 2-d pair-correlations.

7.6 Summary and conclusion

In this chapter, first I showed the effect of the improvements made to the Rydberg imaging system as well as the data analysis process. The Rydberg-Rydberg correlation measurements now look drastically better. I then measured Rydberg-Rydberg correlations for on-resonant and and off-resonant excitation from the MOT. I thereby verified the predictions of Robicheaux and Hernández [47] (Section 2.2.3), at least for S-states. Finally, I have quantitatively measured and explained the dependence of the blockade radius on the excitation frequency in an ODT. In the process, I have discovered the interesting fact that an off-resonant excitation is possible for S-states, but suppressed by the light shift for D-states, leading to a "perfect blockade" (single Rydberg excitation) in the latter case.

In this last part, I have shown that spatially-dependent light shifts in an optical trap always cause a decrease in the blockade radius (with the exception of the "perfect blockade" case). This may have implications in quantum information processing using neutral atoms in an optical lattice. The depth of each lattice site depends on the distance from the optical focus, so the same variation in light shift will be present. This could decrease the fidelity of gate operations based on long-range entanglement using the blockade. Of course, this effect will be minimized by the use of a "magic

wavelength" lattice for which the Rydberg state shift and ground state shifts are equal in magnitude and sign. This type of lattice is beneficial in quantum information for other reasons, having to do with reduction of decoherence caused by entanglement of the internal atomic state with the atomic center of mass motion [28].

CHAPTER VIII

Future Work and Conclusion

There are a number of possible experiments one could do with a general purpose Rydberg imaging apparatus as described in this thesis. In Section 8.1, I give an example for which I have done some of the initial setup work, and which has inspired considerable recent activity in the Rydberg community. In the more distant future, other experiments could be done that would benefit from the imaging apparatus. As examples, one could study Rydberg state hopping (as mentioned in Chapter I) or plasma dynamics. I will discuss the feasibility of state-hopping experiments in Section 8.2.

8.1 Exciting a Rydberg crystal

As mentioned in previous chapters, an eventual goal for this experiment is to excite a Rydberg crystal. A Rydberg crystal is a crystal-like ordered arrangement of Rydberg atoms, as I will describe below. The proposal for excitation of a Rydberg crystal is relatively recent [64], so not many applications have been proposed yet, to my knowledge. One reason a Rydberg crystal is interesting is that an ordered arrangement of Rydberg atoms can be produced from a disordered arrangement of ground state atoms. One possible application is to produce ultracold plasmas, by using microwaves to force the ionization of Rydberg atoms at their crystal-lattice

positions. The ions thus produced have much lower initial potential energy than randomly placed ions, and so will not undergo rapid heating by conversion of potential to kinetic energy.

I will try to give an evocative description of a Rydberg crystal here; detailed theory has been published in many places, for example in references [64, 72–74]. First I use a simple three-atom model to describe the general structure of the many-atom energy levels that are involved in the creation of a Rydberg crystal. Then I explain in what sense it is a crystal.

We describe the system of ground state atoms coupled to Rydberg states by the same dressed-state Hamiltonian as given in Equations 2.17 and 2.18. I repeat it here for convenience, with slightly different notation:

$$\hat{H} = \sum_j \Big\{ -\Delta\ \hat{\sigma}_{11}^{(j)} + \frac{\Omega}{2}(\hat{\sigma}_{01}^{(j)} + \hat{\sigma}_{10}^{(j)}) \Big\} \tag{8.1}$$

$$+ \sum_{j<k} V_{jk} \hat{\sigma}_{11}^{(j)} \hat{\sigma}_{11}^{(k)} \tag{8.2}$$

Here, the differences are that the laser detuning from resonance is now labeled Δ and the states are labeled $|0\rangle = |g\rangle$ and $|1\rangle = |r\rangle$. The $\hat{\sigma}$ operators are

$$\hat{\sigma}_{11}^{(i)} = |r_i\rangle\langle r_i| \tag{8.3}$$

$$\hat{\sigma}_{01}^{(i)} = |g_i\rangle\langle r_i| \tag{8.4}$$

$$\hat{\sigma}_{10}^{(i)} = |r_i\rangle\langle g_i| \tag{8.5}$$

Figure 8.1 shows the energy level structure of a three-atom system, using the dressed state picture. The case for $\Omega = 0$ is shown in Figure 8.1(a), while the case for $\Omega = 2\pi \times 1$ MHz is shown in (b). First consider figure (a). The slopes of the energy levels with respect to detuning Δ are determined by the number of atoms excited, $\sum_j \hat{\sigma}_{11}^{(j)}$. There is only one line with zero slope, for state $|000\rangle$. For a slope

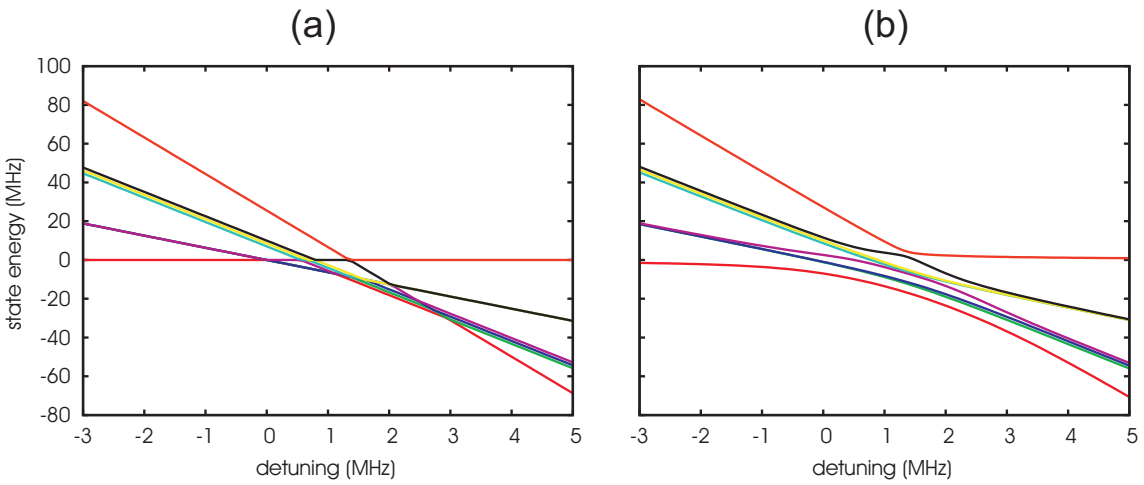

Figure 8.1: Level diagram for 3 atoms in the dressed state picture. (a) $\Omega = 0$ MHz. (b) $\Omega = 2\pi \times 1$ MHz.

of 1 there are three states with a single Rydberg excitation; they are all degenerate. For two Rydberg excitations we now have three states which are nondegenerate due to interactions.[1] The interactions also cause a nonzero state energy at $\Delta = 0$. Higher excitation numbers will have higher slopes and generally higher interaction energies.

Following the ground state (lowest energy state) of the system as a function of detuning Δ, we see that at $\Delta = 0$ it transitions from having zero excitations to one excitation. At higher detunings the slope increases further, indicating a higher number of excitations (k). Note that the ground state at a given detuning will be the state with the corresponding number of excitations and the lowest Rydberg-Rydberg interaction energy. In a 3-atom case with two excitations this means that the pair that is furthest apart is excited. However, in a more general many-atom gas, this will be the state with k excitations distributed in a crystal-like structure to minimize energy. This is called a Rydberg crystal.

To produce this crystal state from a ground state gas, one first starts at negative

[1]The interaction strengths for the three atoms in this calculation are $V_{12} = 10$ MHz, $V_{23} = 8.5$ MHz, and $V_{13} = 7$ MHz so that there is some variation in strengths to slightly remove degeneracies in the state diagram.

detuning Δ and $\Omega = 0$. The laser amplitude is then increased to cause anticrossings in the state diagram, as shown in Figure 8.1(b). The detuning Δ is adiabatically swept to a positive value, and the laser amplitude is then adiabatically turned off. The crystal will have a number of excitations determined by the final detuning Δ.

No experimental group has yet observed a Rydberg crystal of the type described above. Schauß et al. [56] have observed very nice ordered structures in a Rydberg gas, but in their experiment there is no adiabatic sweep of any kind. Their observation of structures with different excitation number k was done by post-selection of the excitation number. For the adiabatic-production method, the bird is still in the bushes.

8.1.1 Practical considerations

In order for the adiabatic production method to work, one must have sufficiently large state splittings (as shown in Figure 8.1b) to prevent non-adiabatic transitions (Landau-Zener tunneling) during the sweep. This requires a Rabi frequency larger than the inverse of the sweep time. As mentioned in Section 6.3, we have a two-photon Rabi frequency of $2\pi \times 2.5$ MHz. This should be sufficient to allow the sweep times of 5-10 μs suggested by theorists [72].

There are a few differences between our possible experimental implementation and the theoretical descriptions. The first is a non-uniformity of the Rabi frequency in space, due to the focused laser beam being smaller than the atom sample. One would hope this would simply produce a Rydberg crystal within the excitation beam, but the details of the effect have not yet been considered. Secondly, the use of an ODT to increase density and reduce the experimental volume will cause spatial variation of the transition frequency, and therefore of Δ. This effect has also not yet been considered.

8.1.2 Experimental implementation

I have attempted to implement an adiabatic frequency sweep in my experiment but was not yet successful. Due to the details of the single-pass AOM setup for the 480 nm excitation beam, a frequency sweep caused multiple orders from the AOM to couple into the optical fiber that brings the beam to my experiment. The multiple orders interfered with a 60 MHz beat note, which was not useful.

There are other possibilities for implementing the frequency sweep. Another idea is to implement an electric field sweep to tune the atomic resonance through the laser frequency, rather than vice versa. This would likely involve an inhomogeneous electric field at the position of the atoms, which would have the disadvantage of a non-uniform atomic frequency within the excitation volume. This case was not treated by published theory, which assumes all atoms have the same transition frequency. A second disadvantage is the limited available tuning range for the atomic transition. With an electric-field-induced frequency shift, the maximum frequency shift achievable for $60S_{1/2}$ is ≈ 50 MHz before the $60S_{1/2}$ state meets the Stark-shifted hydrogenic manifold. This may not be a sufficient tuning range, especially considering the ≈ 30 MHz frequency width of the ODT excitation spectrum itself. One should start the frequency sweep from the red side of the spectrum in order to prevent any resonant excitation of multiple Rydberg atoms before the start of the sweep; and one should sweep some 10's of MHz past the blue side of the spectrum to generate the crystal. The available 50 MHz range therefore seems limiting.

Another, more obvious, idea for the frequency sweep is to use the double-pass AOM on the 780 nm excitation beam. This method has not been considered in detail yet, but has some promise. One point to consider is the response speed of the AOM; as mentioned in Chapter VI the minimum pulse time is 1.4 μs, and we are looking

for frequency sweeps and pulses on the order of 5 μs. This will have to be tested.

In summary, although initial attempts to implement the required pulses and frequency sweep were not successful, prospects seem good for an implementation in the near future.

8.2 State-hopping experiments

Initial proposals for the TIP experiment included the idea of studying Rydberg state-hopping, similar to the excitation transport referenced in Section 1.1. In this section I give a brief explanation of the physics, and outline a method by which the TIP experiment might be reconfigured to allow study of such phenomena.

In the context of many-body physics, the strong interactions between Rydberg atoms can lead to significant coupling between atoms at several-μm separations in an atomic vapor, without atomic motion being required. This situation is referred to as a "frozen Rydberg gas" when atomic motion is negligible on the experimental timescale ($\sim \mu$s). The interactions can lead to state changing "collisions" (where one Rydberg atom gains energy and the other loses energy) and the diffusion of an atomic state from a "reaction center" throughout the gas, without atomic motion [8–10]. This can be represented schematically as the excitation of Rydberg $|p\rangle$ states[2] and the following state-changing and state-hopping reactions:

$$|pp\rangle \rightarrow |ss'\rangle \quad \text{(where } s' \text{ has higher and } s \text{ lower energy)} \tag{8.6}$$

$$|sp\rangle \rightarrow |ps\rangle \tag{8.7}$$

$$|s'p\rangle \rightarrow |ps'\rangle \quad . \tag{8.8}$$

When the interaction strengths are much larger than difference in energy between the "reactant" and "product" multi-Rydberg states, the state changing collisions can

[2]These are the states used by reference [8]; in the TIP experiment, with two-photon excitation starting from the $5S_{1/2}$ ground state, I would excite to perhaps $|ss'\rangle$ states as in [9] and have state diffusion starting from here.

occur on timescales much faster than one can explain using only pairwise interactions, and many-body interactions must be considered [15].

This coherent energy transport in Rydberg systems is similar in spirit to energy transport in photosynthetic systems [12]. However, the timescales are slower and the distance scales are larger for Rydberg atom systems (μs vs. fs, and μm vs. nm), which makes them experimentally easier to probe [11].

To my knowledge, no studies of this phenomenon have been done with spatial resolution of the Rydberg atom positions. The TIP experiment could potentially accomplish this.

The difficult feature of this experiment is that it requires both state selectivity in the Rydberg atom detection (e.g. the ability to detect state $|s\rangle$ as distinct from state $|s'\rangle$) as well as spatial sensitivity. This combination has been demonstrated with *one*-dimensional spatial sensitivity by Ditzhuijzen et al. [75]. The authors use state selective field ionization with electron detection (as opposed to the ion detection used in the TIP experiment), and they detect the one-dimensional position of the Rydberg atoms using the electron time of flight to the MCP. The position resolution is then along the axis leading toward the MCP. The state sensitivity is accomplished by switching the electric field to be larger than the ionization field of the state they wish to detect, but smaller than the ionization field of other states. Only the desired state is then ionized.

The implementation of similar state-selective field ionization (SSFI) in the TIP experiment would be difficult, if I intend to retain 2D spatial resolution. This is due to technical reasons, having to do with the detection efficiency of the MCP. In order to be detected by the MCP, ions need a minimum impact energy of ~ 500 eV. This requires a high potential difference between the TIP and the MCP front plate. We

have seen in Chapter V that a large voltage on the MCP causes significant refocusing of the ion trajectories near the MCP. Good imaging characteristics therefore require instead a large voltage on the TIP, e.g. $\geqslant$500 V. A voltage of 500 V on the TIP will produce an electric field of (8.5 V/cm per V) $\times$ 500 V = 4250 V/cm at 200 μm above the TIP (see Section 5.2.2). This is to be compared with the field ionization threshold of the Rydberg states I typically work with: 30 V/cm for $60S_{1/2}$. With the electric field this much higher than the typical ionization threshold, it is completely impossible to perform SSFI. This limitation ultimately comes from the MCP detection efficiency for ions.

In contrast, the MCP can detect electrons with energies of 20-50 eV, with the detection efficiency climbing to a maximum around energies of a few hundred eV. If I changed from detecting ions to detecting electrons[3] I could turn the MCP front plate down to near 0 V and I would still only need a small voltage on the TIP (slightly larger in magnitude than -20 to -50 V) to have efficient detection by the MCP. With no refocusing from the MCP voltage[4], the imaging should be largely independent of the TIP voltage. We could thus select the TIP voltage based on the desired state we wish to detect. The electric field is chosen to be strong enough to ionize the desired state, and smaller than what would ionize other states. A TIP switched to -20 to -50 V will give an electric field (at $\sim$ 200 μm above the TIP) of appropriate strength for SSFI of states in the vicinity of n = 25 to 35, as used in [9]. If the excitation region is moved further from the TIP, somewhat compromising the spatial resolution, and the TIP potential is increased appropriately, one can boost the electron kinetic energy without compromising the SSFI. I will use this in calculations below.

[3]Theoretically, the electron trajectories would be the same as the ion trajectories, if the signs of all voltages are flipped and there are no magnetic fields.

[4]Note: I'm assuming there will be no refocusing from the MCP when the MCP is set to 0 V. It is possible there may be a voltage gradient across the MCP front plate, due to electron conduction within the MCP to the middle/back plates as well as the non-zero resistance of the plates themselves. Such a voltage gradient *would* cause a refocusing of electrons, and could be problematic.

There are several disadvantages for electron detection, however. These considerations are why the TIP experiment has previously only used ion detection. One is the possibility of field emission of electrons from the TIP, if the TIP is switched to a high negative voltage. This would send spurious electrons to the MCP and could create significant noise. Second, electrons are easily deflected by magnetic fields due to their small mass. The cyclotron radius (trajectory's radius of curvature) R for a charged particle in a magnetic field, given an accelerating potential of V_a (and therefore a kinetic energy of qV_a), is

$$R^2 = \frac{2V_a}{\frac{q}{m}B^2} \tag{8.9}$$

where q is the charge, m is the mass, and B is the magnetic field strength.

An electron with energy 1000 eV in a magnetic field of 10 Gauss (typical for MOT operation) has a radius of curvature of 10 cm, which is smaller than the distance to the MCP.[5] The deflection gets even stronger with lower electron energies. In contrast, an ion has insignificant deflection.

To achieve good imaging characteristics with electrons, especially at low energies used for SSFI, would require minimizing the magnetic field. One would need to turn off the MOT magnetic field, as well as zero out the field of the earth and any other stray fields with the Helmhotz bias coils on the experiment. In this case the ground state rubidium atoms could be collected in the MOT and then transferred to the ODT before switching to a zero magnetic field configuration. The ODT could then hold the atoms during the excitation and ionization process.

If the radius of curvature is large compared to the distance to the MCP ($D \approx$ 16 cm), the lateral deflection d of the particle on the MCP will be

$$d = \frac{D^2}{2R} \tag{8.10}$$

[5]Note this is a worst-case estimate, as the magnetic field from the MOT coils should be near zero if the electrons are near the experiment's imaging axis.

Suppose we can zero the magnetic field to 0.1 Gauss, and that we wish to distinguish between $24P_{1/2}$ and $34P_{3/2}$ (with respective ionization fields 1550 and 330 V/cm) as used in [9]. If we apply -1000 V to the TIP, at an excitation position of 1 to 3 mm above the TIP we will have a field of between 1500 and 400 V/cm (see Figure 5.3) as appropriate for SSFI. The electrons produced there will have energies of $\sim$ 120 to 280 eV. The deflection of 200 eV electrons in a 0.1 Gauss field over a distance of 16 cm (to the MCP) will be about 3 mm. Compared to the 18 mm diameter of the MCP, this deflection is acceptable.[6] Moving the excitation region a factor of 10 further from the TIP (as compared to the current working distance of 200 μm) will reduce the resolution from about 1 μm to about 10 μm, comparable to the resolution of Ditzhuijzen et al. [75] in one dimension.

Thus, in order of magnitude, combining spatial resolution with state selective detection is feasible. This could enable a number of interesting studies, but in particular studies of state-hopping dynamics.

8.3 Conclusion

In this thesis I have described an experimental apparatus for direct spatial imaging of Rydberg atom positions. In Chapter II, I have detailed some of its advantages over other Rydberg imaging systems. In Chapters V and VI, I presented its optimization via characterization of the ion trajectories in the chamber, and via an increase in ground state atom density at the desired excitation region near the TIP.

I have used this apparatus to perform measurements of the Rydberg-Rydberg correlation function in a cold atomic gas. In Chapter IV, I presented the first-ever direct spatial images of the Rydberg excitation blockade. In Chapter VII, I investigated

[6] I am assuming a uniform magnetic field, which only shifts the image on the MCP. Magnetic field inhomogeneities could distort the imaging considerably, which *would* be a problem.

the effects of laser detuning and optical potentials on the blockade effect. With the understanding of this physics in hand, the next step is to attempt to excite a Rydberg crystal, which is currently a topic of considerable interest in the Rydberg atom community.

APPENDICES

APPENDIX A

Shadow Imaging

For shadow imaging[1], a laser beam with an intensity profile $I_0(x, y)$ is incident on trapped atoms, and the profile of the beam after passing through the trap $I(x, y)$ is measured with a camera.

A change in intensity can be written as:

$$\Delta I = \frac{\Delta E}{A \cdot T} \tag{A.1}$$

where

$$\Delta E = \text{energy difference} \tag{A.2}$$

$$A = \text{surface area} \tag{A.3}$$

$$T = \text{time} \tag{A.4}$$

$$\tag{A.5}$$

The effect on the two-dimensional intensity profile $I(x, y)$ is:

$$dI = -h\nu\gamma N_V(x, y, z)dz \tag{A.6}$$

where the negative sign is a result of the intensity decrease as light is scattered out of the beam. The change in energy due to a single photon is $h\nu$, γ is the photon

[1]Most of the following was taken from a document by Brenton Knuffman and Kelly Younge, but I have reproduced it in order to correct some errors.

scattering rate which depends on the intensity and frequency of the probe light (the average time for a single photon to be scattered is $T = 1/\gamma$), and $N_V(x, y, z)$ is the volume density of the atomic sample. The atom cloud is divided into slices of thickness dz, and multiplying by the number density gives the number of atoms per unit area in the x-y plane.

We therefore have $-h\nu\gamma = \Delta E/T$ for a single atom, and $N_V \cdot dz = N/A$ where N is the number of atoms. Multiplying these together, we have:

$$\Delta I = \frac{N\Delta E}{A \cdot T} \tag{A.7}$$

The factor of N results from the fact that there are N atoms in the sample.

On resonance, $\gamma = \frac{\Gamma}{2}\frac{I}{I_{sat}}$ where Γ is the natural linewidth of the transition and I_{sat} is the corresponding saturation intensity. (This holds for low intensities, $I < I_{sat}$.) Then,

$$dI = -h\nu\gamma N_V(x, y, z)dz \tag{A.8}$$

$$= -h\nu\frac{\Gamma}{2}\frac{I}{I_{sat}}N_V(x, y, z)dz \tag{A.9}$$

$$dI/I = -\frac{\Gamma h\nu}{2I_{sat}}N_V(x, y, z)dz \tag{A.10}$$

$$\ln(I(x, y)/I_0(x, y)) = -N_A(x, y)\frac{\Gamma h\nu}{2I_{sat}} \tag{A.11}$$

$$N_A(x, y) = \frac{2I_{sat}}{\Gamma h\nu}\ln(I_0(x, y)/I(x, y)) \tag{A.12}$$

This area density is what one measures directly using absorption imaging on a CCD. From this, the total atom number, N, can be calculated:

$$N = \int_{-\infty}^{\infty}\int_{-\infty}^{\infty} N_A(x, y)dxdy \tag{A.13}$$

The central volume density can be calculated by assuming a Gaussian distribution of atoms,

$$N_A(x, y) = N_A(0, 0)\exp\left(-\frac{x^2 + y^2}{\sigma^2}\right) \quad . \tag{A.14}$$

The characteristic width, σ, and the central area density can be calculated by fitting the shadow image data to a 2D Gaussian function. For the volume density we then have:

$$N_V(x,y,z) = N_V(0,0,0)\exp\left(-\frac{x^2+y^2+z^2}{\sigma^2}\right) \tag{A.15}$$

and since

$$N_A(x,y) = \int_{-\infty}^{\infty} N_V(x,y,z)dz \tag{A.16}$$

we finally have

$$N_V(0,0,0) = \frac{N_A(0,0)}{\sigma\sqrt{\pi}} \quad . \tag{A.17}$$

When shadow imaging an asymmetric MOT (as contrasted with a symmetric dipole trap), one must make an assumption about the z-depth L_z of the cloud based on the size in other axes. Then a volume density estimate could be

$$N_V(0,0,0) = \frac{N_A(0,0)}{L_z} \quad . \tag{A.18}$$

APPENDIX B

Analytical Calculations of Excitation Spectra from a Variety of Trapping Potentials

Here I calculate the shape of an excitation spectrum for an atomic gas in a trap.

I assume a Maxwell Boltzman distribution of particles in the trapping potential. I also assume that the spectral shift of an atom in the trap is proportional to the potential of the atom in the trap. (This is true, e.g., in an optical dipole trap or in a magnetic trap.)

To be mathematically precise with the above paragraph, I label the energy of the particle in the trap as ϵ. I take the excitation frequency to be $f = \frac{\epsilon}{h} \times \xi$ where ξ is the proportionality constant between the energy in the trap (ϵ) and the energy shift of the transition being probed (hf). I will calculate the spectrum in terms of ϵ, which can be scaled at the end to get the result in terms of f.

Now let's calculate the spectrum. I start with some definitions to state the problem precisely. Take S to be the integral of the excitation spectrum, which is proportional to the number of atoms N. The spectral density per atom is α, so that

$$S = \alpha N \tag{B.1}$$

The spectral density in energy $s_\epsilon(\epsilon)$ we define as

$$S = \int s_\epsilon(\epsilon) d\epsilon \tag{B.2}$$

So $s_\epsilon(\epsilon)$ is what we normally refer to as the excitation spectrum. (Except we normally measure it in terms of the frequency f. It is more convenient here to use energy.)

The spectral density in energy is the product of the number of atoms with that energy and the spectral density per atom:

$$s_\epsilon = \alpha N_\epsilon \tag{B.3}$$

The number of atoms with energy ϵ is

$$N_\epsilon = n_\epsilon g_\epsilon \tag{B.4}$$

where n_ϵ is the number of atoms in a given state with energy ϵ, and g_ϵ is the number of states with energy ϵ (i.e. the degeneracy).

So we have thus far

$$s_\epsilon = \alpha n_\epsilon g_\epsilon \tag{B.5}$$

For a Maxwell Boltzman distribution,

$$n_\epsilon = e^{-\frac{\epsilon}{kT}} \tag{B.6}$$

The degeneracy of states g_ϵ is based on the trapping potential and the trapping geometry. We can calculate this from the physical volume of an energy shell. Suppose that $V(\epsilon)$ is the physical volume with an enegy ϵ at its surface.[1] The degeneracy of states is then

$$g_\epsilon(\epsilon) = \frac{dV}{d\epsilon} \tag{B.7}$$

B.1 2D harmonic potentials

Now we have to get specific about our trap to determine $\frac{dV}{d\epsilon}$. Let's assume a harmonic trapping potential with a cylindrical geometry. (This is an optical dipole

[1] I will assume that the potential is monotonically increasing from the trap center, so all points inside $V(\epsilon)$ have energy $< \epsilon$. This is so I can easily relate volume and energy shells. If a trap has multiple minima, we're looking only inside a local minimum.

trap, near trap center.) We have

$$\epsilon = ar^2 \tag{B.8}$$

$$V = \pi r^2 Z \tag{B.9}$$

where a is a trap constant, r is the radial position from the center, and Z is the length of the trap in the z-dimension (some constant). Then we have

$$g_\epsilon = \frac{dV}{d\epsilon} = \frac{\frac{dV}{dr}}{\frac{d\epsilon}{dr}} = \frac{\pi Z}{a} \tag{B.10}$$

Since g_ϵ is a constant, the spectrum has an exponential shape due to the Maxwell Boltzman distribution:

$$s_\epsilon = \left(\frac{\alpha \pi Z}{a}\right) \times e^{-\frac{\epsilon}{kT}} \tag{B.11}$$

This is the result mentioned in Section 6.4.

B.2 3D harmonic potentials

If instead we assume a 3D harmonic potential, we have

$$\epsilon = ar^2 \tag{B.12}$$

$$V = \frac{4}{3}\pi r^3 \tag{B.13}$$

where r is now measured in 3D. The degeneracy is now

$$g_\epsilon = \frac{\frac{dV}{dr}}{\frac{d\epsilon}{dr}} = \frac{2\pi r}{a} = \frac{2\pi}{a^{3/2}}\sqrt{\epsilon} \tag{B.14}$$

This time the factors of r don't cancel, and we need to plug in for r in terms of ϵ.

(B.15)

The spectrum is now not quite exponential in energy (frequency):

$$s_\epsilon = \left(\frac{2\pi\alpha}{a^{3/2}}\right) \times \sqrt{\epsilon}\, e^{-\frac{\epsilon}{kT}} \tag{B.16}$$

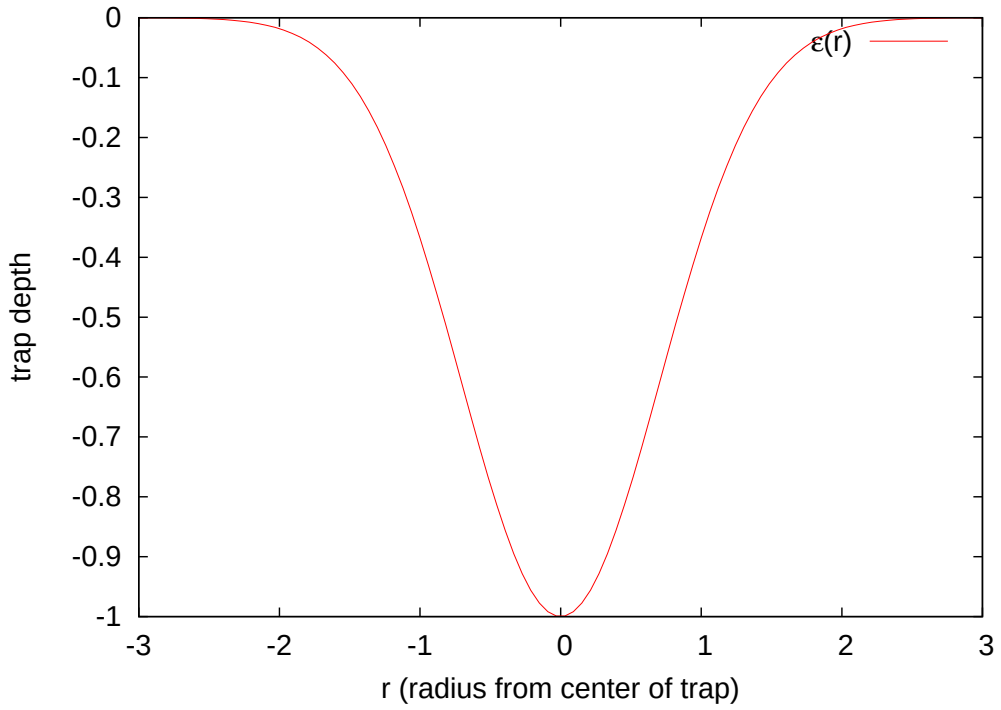

Figure B.1: ODT potential, for $a = 1$ and $\sigma = 1$.

B.3 2D gaussian potential

This is *really* the shape of an optical dipole trap, including regions away from the trap center. This will give a spectrum similar in shape to that calculated in Section 6.4.2, by the spectrum simulation.

Here we have

$$\epsilon = -ae^{-\left(\frac{r}{\sigma}\right)^2} \tag{B.17}$$

$$V = \pi r^2 Z \tag{B.18}$$

Note the negative sign in front for the energy equation. This is so we have a trap for $a > 0$. Note this now means the energy ϵ is negative, and the bottom of the trap is at energy $-a$. For clarity, in Figure B.1 I show a plot of the potential (with $a = 1$ and $\sigma = 1$).

In this case we have

$$g_\epsilon = \frac{\frac{dV}{dr}}{\frac{d\epsilon}{dr}} \tag{B.19}$$

$$= \frac{2\pi r Z}{(-a)\left(-\frac{2r}{\sigma^2}\right) e^{-\left(\frac{r}{\sigma}\right)^2}} \tag{B.20}$$

$$= \frac{\pi Z \sigma^2}{a\ e^{-\left(\frac{r}{\sigma}\right)^2}} \tag{B.21}$$

$$= \frac{\pi Z \sigma^2}{-\epsilon} \tag{B.22}$$

The spectrum is

$$s_\epsilon = \left(\alpha \pi Z \sigma^2\right) \times \frac{1}{-\epsilon}\ e^{-\frac{\epsilon}{kT}} \tag{B.23}$$

where the relevant energy range is $\epsilon = -a$ up to $\epsilon = 0$. The spectrum blows up for $\epsilon \to 0$ because $\epsilon = 0$ is outside the trap, where there is infinite volume.

We typically excite transitions that are blue-shifted in an ODT. This includes both $5S \to 5P$ and $5S \to$ Rydberg transitions. So a negative energy ϵ corresponds to a positive frequency f. I therefore take the scale factor ξ to be negative.

I scale the frequency in terms of the trap depth a for sensible plotting. To do so I define a normalized frequency shift in terms of the trap depth:

$$x = -\frac{\epsilon}{a} \tag{B.24}$$

The negative sign accounts for the sign of ξ, and the $1/a$ scales the frequency to units of trap depth. To compare with experiment, one can scale the x-axis (frequency axis) of the plot. Now $x = 0$ is outside the trap and $x = 1$ is the center of the trap.

The spectrum is

$$s_\epsilon = \frac{(\alpha \pi Z \sigma^2)}{a} \times \frac{1}{x}\ e^{\frac{x}{kT/a}} \tag{B.25}$$

For plotting in Figure B.2 I ignore the constants out front, which just give the amplitude. I take $kT = 0.5a$ for the temperature being half the trap depth, as

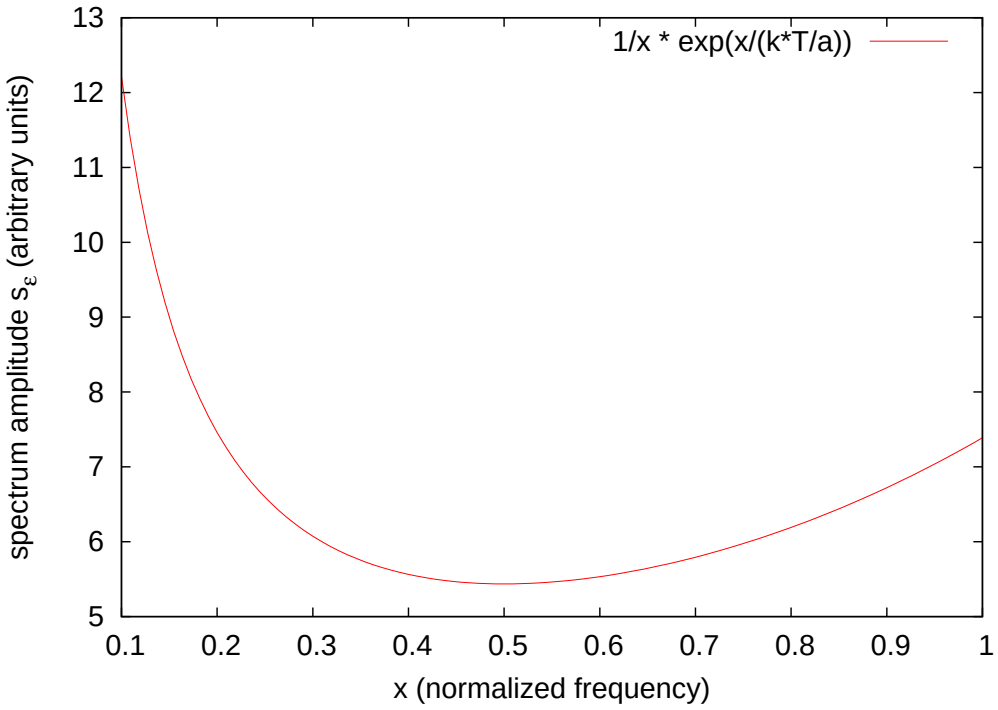

Figure B.2: ODT spectrum, calculated analytically from Equation B.25.

in Section 6.4.2. (The choice of temperature greatly affects the spectrum, and the presence/absence of the MOT/ODT peaks, as one might imagine.) On the left of the spectrum is the MOT peak, and on the right is the ODT peak.

BIBLIOGRAPHY

BIBLIOGRAPHY

[1] Thomas F. Gallagher. *Rydberg Atoms*. Cambridge University Press, 1994.

[2] G. Nogues, A. Rauschenbeutel, S. Osnaghi, M. Brune, J. M. Raimond, and S. Haroche. Seeing a single photon without destroying it. *Nature*, 400(6741):239–242, July 1999. ISSN 0028-0836. doi: 10.1038/22275. URL http://www.nature.com.proxy.lib.umich.edu/nature/journal/v400/n6741/full/400239a0.html.

[3] Sébastien Gleyzes, Stefan Kuhr, Christine Guerlin, Julien Bernu, Samuel Deléglise, Ulrich Busk Hoff, Michel Brune, Jean-Michel Raimond, and Serge Haroche. Quantum jumps of light recording the birth and death of a photon in a cavity. *Nature*, 446(7133):297–300, March 2007. ISSN 0028-0836. doi: 10.1038/nature05589. URL http://www.nature.com.proxy.lib.umich.edu/nature/journal/v446/n7133/full/nature05589.html.

[4] J. Hare, A. Nussenzweig, C. Gabbanini, M. Weidemuller, P. Goy, M. Gross, and S. Haroche. Toward a rydberg constant measurement on circular atoms. *IEEE Transactions on Instrumentation and Measurement*, 42(2):331 –334, April 1993. ISSN 0018-9456. doi: 10.1109/19.278576.

[5] Robert Lutwak, Jeffrey Holley, Pin Peter Chang, Scott Paine, Daniel Kleppner, and Theodore Ducas. Circular states of atomic hydrogen. *Physical Review A*, 56(2):1443–1452, 1997. doi: 10.1103/PhysRevA.56.1443. URL http://link.aps.org/doi/10.1103/PhysRevA.56.1443.

[6] S. K. Dutta, J. R. Guest, D. Feldbaum, A. Walz-Flannigan, and G. Raithel. Ponderomotive optical lattice for rydberg atoms. *Physical Review Letters*, 85(26):5551–5554, December 2000. doi: 10.1103/PhysRevLett.85.5551. URL http://link.aps.org/doi/10.1103/PhysRevLett.85.5551.

[7] Georg Raithel. Measurement of the rydberg constant in a magic-wavelength optical lattice. NIST Precision Measurement Grant Award, http://www.nist.gov/pml/div684/fcdc/upload/Current-Awardees-2012-3.pdf, 2012.

[8] I. Mourachko, D. Comparat, F. de Tomasi, A. Fioretti, P. Nosbaum, V. M. Akulin, and P. Pillet. Many-body effects in a frozen rydberg gas. *Physical Review Letters*, 80(2):253, January 1998. doi: 10.1103/PhysRevLett.80.253. URL http://link.aps.org.proxy.lib.umich.edu/doi/10.1103/PhysRevLett.80.253.

[9] W. R. Anderson, J. R. Veale, and T. F. Gallagher. Resonant dipole-dipole energy transfer in a nearly frozen rydberg gas. *Physical Review Letters*, 80(2):249, January 1998. doi: 10.1103/PhysRevLett.80.249. URL http://link.aps.org.proxy.lib.umich.edu/doi/10.1103/PhysRevLett.80.249.

[10] V. M. Akulin, F. de Tomasi, I. Mourachko, and P. Pillet. Level-band problem and many-body effects in cold rydberg atoms. *Physica D: Nonlinear Phenomena*, 131(1-4):125–140, July 1999. ISSN 0167-2789. doi: 10.1016/S0167-2789(98)00224-3. URL http://www.sciencedirect.com/science/article/B6TVK-41CR5CF-B/2/66ae6f8229b84e1310eb145a7bce38d7.

[11] C. S. E. van Ditzhuijzen, A. F. Koenderink, J. V. Hernández, F. Robicheaux, L. D. Noordam, and H. B. van Linden van den Heuvell. Spatially resolved observation of dipole-dipole interaction between rydberg atoms. *Physical Review Letters*, 100(24):243201, June 2008. doi: 10.1103/PhysRevLett.100.243201. URL http://link.aps.org/doi/10.1103/PhysRevLett.100.243201.

[12] Gregory S. Engel, Tessa R. Calhoun, Elizabeth L. Read, Tae-Kyu Ahn, Tomáš Man?al, Yuan-Chung Cheng, Robert E. Blankenship, and Graham R. Fleming. Evidence for wavelike energy transfer through quantum coherence in photosynthetic systems. *Nature*, 446(7137):782–786, April 2007. ISSN 0028-0836. doi: 10.1038/nature05678. URL http://www.nature.com.proxy.lib.umich.edu/nature/journal/v446/n7137/full/nature05678.html.

[13] Thomas J. Carroll, Shubha Sunder, and Michael W. Noel. Many-body interactions in a sample of ultracold rydberg atoms with varying dimensions and densities. *Physical Review A*, 73(3):032725, March 2006. doi: 10.1103/PhysRevA.73.032725. URL http://link.aps.org.proxy.lib.umich.edu/doi/10.1103/PhysRevA.73.032725.

[14] Paul J. Tanner, Jianing Han, E. S. Shuman, and T. F. Gallagher. Many-body ionization in a frozen rydberg gas. *Physical Review Letters*, 100(4):043002, January 2008. doi: 10.1103/PhysRevLett.100.043002. URL http://link.aps.org.proxy.lib.umich.edu/doi/10.1103/PhysRevLett.100.043002.

[15] K. C. Younge, A. Reinhard, T. Pohl, P. R. Berman, and G. Raithel. Mesoscopic rydberg ensembles: Beyond the pairwise-interaction approximation. *Physical Review A*, 79(4):043420, April 2009. doi: 10.1103/PhysRevA.79.043420. URL http://link.aps.org/doi/10.1103/PhysRevA.79.043420.

[16] L. Isenhower, E. Urban, X. L. Zhang, A. T. Gill, T. Henage, T. A. Johnson, T. G. Walker, and M. Saffman. Demonstration of a neutral atom controlled-NOT quantum gate. *Physical Review Letters*, 104(1):010503, January 2010. doi: 10.1103/PhysRevLett.104.010503. URL http://link.aps.org/doi/10.1103/PhysRevLett.104.010503.

[17] T. Wilk, A. Gaëtan, C. Evellin, J. Wolters, Y. Miroshnychenko, P. Grangier, and A. Browaeys. Entanglement of two individual neutral atoms using rydberg blockade. *Physical Review Letters*, 104(1):010502, January 2010. doi: 10.1103/PhysRevLett.104.010502. URL http://link.aps.org/doi/10.1103/PhysRevLett.104.010502.

[18] D. Jaksch, J. I. Cirac, P. Zoller, S. L. Rolston, R. Côté, and M. D. Lukin. Fast quantum gates for neutral atoms. *Physical Review Letters*, 85(10):2208, 2000. doi: 10.1103/PhysRevLett.85.2208. URL http://link.aps.org/doi/10.1103/PhysRevLett.85.2208.

[19] M. D. Lukin, M. Fleischhauer, R. Cote, L. M. Duan, D. Jaksch, J. I. Cirac, and P. Zoller. Dipole blockade and quantum information processing in mesoscopic atomic ensembles. *Physical Review Letters*, 87(3):037901, June 2001. doi: 10.1103/PhysRevLett.87.037901. URL http://link.aps.org/doi/10.1103/PhysRevLett.87.037901.

[20] Rainer Blatt and David Wineland. Entangled states of trapped atomic ions. *Nature*, 453(7198):1008–1015, June 2008. ISSN 0028-0836. doi: 10.1038/nature07125. URL http://www.nature.com.proxy.lib.umich.edu/nature/journal/v453/n7198/full/nature07125.html.

[21] John Clarke and Frank K. Wilhelm. Superconducting quantum bits. *Nature*, 453(7198):1031–1042, June 2008. ISSN 0028-0836. doi: 10.1038/nature07128. URL http://www.nature.com.proxy.lib.umich.edu/nature/journal/v453/n7198/full/nature07128.html.

[22] M. D. Reed, L. DiCarlo, S. E. Nigg, L. Sun, L. Frunzio, S. M. Girvin, and R. J. Schoelkopf. Realization of three-qubit quantum error correction with superconducting circuits. *Nature*, 482(7385):382–385, February 2012. ISSN 0028-0836. doi: 10.1038/nature10786. URL http://www.nature.com.proxy.lib.umich.edu/nature/journal/v482/n7385/full/nature10786.html.

[23] Pieter Kok, W. J. Munro, Kae Nemoto, T. C. Ralph, Jonathan P. Dowling, and G. J. Milburn. Linear optical quantum computing with photonic qubits. *Reviews of Modern Physics*, 79(1): 135–174, January 2007. doi: 10.1103/RevModPhys.79.135. URL http://link.aps.org/doi/10.1103/RevModPhys.79.135.

[24] Xiaoqin Li, Yanwen Wu, Duncan Steel, D. Gammon, T. H. Stievater, D. S. Katzer, D. Park, C. Piermarocchi, and L. J. Sham. An all-optical quantum gate in a semiconductor quantum dot. *Science*, 301(5634):809–811, August 2003. ISSN 0036-8075, 1095-9203. doi: 10.1126/science.1083800. URL http://www.sciencemag.org.proxy.lib.umich.edu/content/301/5634/809.

[25] J. R. Petta, A. C. Johnson, J. M. Taylor, E. A. Laird, A. Yacoby, M. D. Lukin, C. M. Marcus, M. P. Hanson, and A. C. Gossard. Coherent manipulation of coupled electron spins in semiconductor quantum dots. *Science*, 309(5744):2180–2184, September 2005. ISSN 0036-8075, 1095-9203. doi: 10.1126/science.1116955. URL http://www.sciencemag.org.proxy.lib.umich.edu/content/309/5744/2180.

[26] C. Barthel, D. J. Reilly, C. M. Marcus, M. P. Hanson, and A. C. Gossard. Rapid single-shot measurement of a singlet-triplet qubit. *Physical Review Letters*, 103(16):160503, October 2009. doi: 10.1103/PhysRevLett.103.160503. URL http://link.aps.org/doi/10.1103/PhysRevLett.103.160503.

[27] Immanuel Bloch. Quantum coherence and entanglement with ultracold atoms in optical lattices. *Nature*, 453(7198):1016–1022, June 2008. ISSN 0028-0836. doi: 10.1038/nature07126. URL http://www.nature.com.proxy.lib.umich.edu/nature/journal/v453/n7198/full/nature07126.html.

[28] M. Saffman, T. G. Walker, and K. Mølmer. Quantum information with rydberg atoms. *Reviews of Modern Physics*, 82(3):2313, 2010. doi: 10.1103/RevModPhys.82.2313. URL http://link.aps.org.proxy.lib.umich.edu/doi/10.1103/RevModPhys.82.2313.

[29] D. Tong, S. M. Farooqi, J. Stanojevic, S. Krishnan, Y. P. Zhang, R. Côté, E. E. Eyler, and P. L. Gould. Local blockade of rydberg excitation in an ultracold gas. *Physical Review Letters*, 93(6):063001, 2004. doi: 10.1103/PhysRevLett.93.063001. URL http://link.aps.org/doi/10.1103/PhysRevLett.93.063001.

[30] E. Urban, T. A. Johnson, T. Henage, L. Isenhower, D. D. Yavuz, T. G. Walker, and M. Saffman. Observation of rydberg blockade between two atoms. *Nat Phys*, 5(2):110–114, February 2009. ISSN 1745-2473. doi: 10.1038/nphys1178. URL http://dx.doi.org.proxy.lib.umich.edu/10.1038/nphys1178.

[31] Alpha Gaetan, Yevhen Miroshnychenko, Tatjana Wilk, Amodsen Chotia, Matthieu Viteau, Daniel Comparat, Pierre Pillet, Antoine Browaeys, and Philippe Grangier. Observation of collective excitation of two individual atoms in the rydberg blockade regime. *Nat Phys*, 5(2): 115–118, February 2009. ISSN 1745-2473. doi: 10.1038/nphys1183. URL http://dx.doi.org.proxy.lib.umich.edu/10.1038/nphys1183.

[32] T. G Walker and M. Saffman. Entanglement of two atoms using rydberg blockade. *Advances in Atomic, Molecular, and Optical Physics*, 61:81–115, 2012. URL http://books.google.com/books?hl=en&lr=&id=HjwXOxoOtMgC&oi=fnd&pg=PA81&dq=%22system+to+be+viable+in+the+long+run,+it+must+exhibit+most+or+all+of%22+%22elements+(DiVincenzo,+2000):+well-de%EF%AC%81ned+qubits+that+allow%22+%22into+well-characterized,+long-lived+quantum+states+with%22+&ots=qSbjlM85wP&sig=g4xcB2OeHcdIBchW_lk6DdsLI3Y.

[33] M. Saffman and T. G. Walker. Creating single-atom and single-photon sources from entangled atomic ensembles. *Physical Review A*, 66(6):065403, December 2002. doi: 10.1103/PhysRevA.66.065403. URL http://link.aps.org/doi/10.1103/PhysRevA.66.065403.

[34] Y. O. Dudin and A. Kuzmich. Strongly interacting rydberg excitations of a cold atomic gas. *Science*, 336(6083):887–889, May 2012. ISSN 0036-8075, 1095-9203. doi: 10.1126/science.1217901. URL http://www.sciencemag.org.proxy.lib.umich.edu/content/336/6083/887.

[35] Hans A. Bethe and Edwin E. Salpeter. *Quantum Mechanics of One- and Two-Electron Atoms*. Dover, 1957.

[36] Aaron Reinhard. *Cold Rydberg-atom interactions*. PhD thesis, University of Michigan, 2008.

[37] A. Reinhard, T. Cubel Liebisch, B. Knuffman, and G. Raithel. Level shifts of rubidium rydberg states due to binary interactions. *Physical Review A*, 75(3):032712, March 2007. doi: 10.1103/PhysRevA.75.032712. URL http://link.aps.org/doi/10.1103/PhysRevA.75.032712.

[38] A. Reinhard, T. Cubel Liebisch, K. C. Younge, P. R. Berman, and G. Raithel. Rydberg-rydberg collisions: Resonant enhancement of state mixing and penning ionization. *Physical Review Letters*, 100(12):123007, March 2008. doi: 10.1103/PhysRevLett.100.123007. URL http://link.aps.org/doi/10.1103/PhysRevLett.100.123007.

[39] A. Reinhard, K. C. Younge, T. Cubel Liebisch, B. Knuffman, P. R. Berman, and G. Raithel. Double-resonance spectroscopy of interacting rydberg-atom systems. *Physical Review Letters*, 100(23):233201, June 2008. doi: 10.1103/PhysRevLett.100.233201. URL http://link.aps.org/doi/10.1103/PhysRevLett.100.233201.

[40] Thibault Vogt, Matthieu Viteau, Jianming Zhao, Amodsen Chotia, Daniel Comparat, and Pierre Pillet. Dipole blockade at förster resonances in high resolution laser excitation of rydberg states of cesium atoms. *Physical Review Letters*, 97(8):083003, 2006. doi: 10.1103/PhysRevLett.97.083003. URL http://link.aps.org.proxy.lib.umich.edu/doi/10.1103/PhysRevLett.97.083003.

[41] Wenhui Li, Paul J. Tanner, and T. F. Gallagher. Dipole-dipole excitation and ionization in an ultracold gas of rydberg atoms. *Physical Review Letters*, 94(17):173001, May 2005. doi: 10.1103/PhysRevLett.94.173001. URL http://link.aps.org/doi/10.1103/PhysRevLett.94.173001.

[42] T. Amthor, M. Reetz-Lamour, S. Westermann, J. Denskat, and M. Weidemüller. Mechanical effect of van der waals interactions observed in real time in an ultracold rydberg gas. *Physical Review Letters*, 98(2):023004, January 2007. doi: 10.1103/PhysRevLett.98.023004. URL http://link.aps.org.proxy.lib.umich.edu/doi/10.1103/PhysRevLett.98.023004.

[43] Thomas Amthor, Markus Reetz-Lamour, Christian Giese, and Matthias Weidemüller. Modeling many-particle mechanical effects of an interacting rydberg gas. *Physical Review A*, 76(5):054702, November 2007. doi: 10.1103/PhysRevA.76.054702. URL http://link.aps.org/doi/10.1103/PhysRevA.76.054702.

[44] T. Cubel Liebisch, A. Reinhard, P. R. Berman, and G. Raithel. Atom counting statistics in ensembles of interacting rydberg atoms. *Physical Review Letters*, 95(25):253002, December 2005. doi: 10.1103/PhysRevLett.95.253002. URL http://link.aps.org/doi/10.1103/PhysRevLett.95.253002.

[45] C Ates, T Pohl, T Pattard, and J M Rost. Strong interaction effects on the atom counting statistics of ultracold rydberg gases. *Journal of Physics B: Atomic, Molecular and Optical Physics*, 39(11):L233–L239, June 2006. ISSN 0953-4075. doi: 10.1088/0953-4075/39/11/L02. URL http://iopscience.iop.org.proxy.lib.umich.edu/0953-4075/39/11/L02.

[46] T. Cubel Liebisch, A. Reinhard, P. R. Berman, and G. Raithel. Erratum: Atom counting statistics in ensembles of interacting rydberg atoms [phys. rev. lett. 95, 253002 (2005)]. *Physical Review Letters*, 98(10):109903, March 2007. doi: 10.1103/PhysRevLett.98.109903. URL http://link.aps.org/doi/10.1103/PhysRevLett.98.109903.

[47] F. Robicheaux and J. V. Hernández. Many-body wave function in a dipole blockade configuration. *Physical Review A*, 72(6):063403, December 2005. doi: 10.1103/PhysRevA.72.063403. URL http://link.aps.org/doi/10.1103/PhysRevA.72.063403.

[48] C. Ates, T. Pohl, T. Pattard, and J. M. Rost. Many-body theory of excitation dynamics in an ultracold rydberg gas. *Physical Review A*, 76(1):013413, July 2007. doi: 10.1103/PhysRevA.76.013413. URL http://link.aps.org.proxy.lib.umich.edu/doi/10.1103/PhysRevA.76.013413.

[49] J V Hernández and F Robicheaux. Simulation of a strong van der waals blockade in a dense ultracold gas. *Journal of Physics B: Atomic, Molecular and Optical Physics*, 41 (4):045301, February 2008. ISSN 0953-4075. doi: 10.1088/0953-4075/41/4/045301. URL http://iopscience.iop.org.proxy.lib.umich.edu/0953-4075/41/4/045301/.

[50] M. H. Anderson, J. R. Ensher, M. R. Matthews, C. E. Wieman, and E. A. Cornell. Observation of bose-einstein condensation in a dilute atomic vapor. *Science*, 269(5221):198–201, July 1995. ISSN 0036-8075, 1095-9203. doi: 10.1126/science.269.5221.198. URL http://www.sciencemag.org.proxy.lib.umich.edu/content/269/5221/198.

[51] Michael Fleischhauer, Atac Imamoglu, and Jonathan P. Marangos. Electromagnetically induced transparency: Optics in coherent media. *Reviews of Modern Physics*, 77(2):633–673, July 2005. doi: 10.1103/RevModPhys.77.633. URL http://link.aps.org/doi/10.1103/RevModPhys.77.633.

[52] G. Günter, M. Robert-de Saint-Vincent, H. Schempp, C. S. Hofmann, S. Whitlock, and M. Weidemüller. Interaction enhanced imaging of individual rydberg atoms in dense gases. *Physical Review Letters*, 108(1):013002, January 2012. doi: 10.1103/PhysRevLett.108.013002. URL http://link.aps.org/doi/10.1103/PhysRevLett.108.013002.

[53] Dieter Meschede and Arno Rauschenbeutel. Manipulating single atoms. In G. Rempe and M.O. Scully, editors, *Advances In Atomic, Molecular, and Optical Physics*, volume Volume 53, pages 75–104. Academic Press, 2006. ISBN 1049-250X. URL http://www.sciencedirect.com/science/article/pii/S1049250X06530034.

[54] Waseem S. Bakr, Jonathon I. Gillen, Amy Peng, Simon Fölling, and Markus Greiner. A quantum gas microscope for detecting single atoms in a hubbard-regime optical lattice. *Nature*, 462 (7269):74–77, November 2009. ISSN 0028-0836. doi: 10.1038/nature08482. URL http://www.nature.com.proxy.lib.umich.edu/nature/journal/v462/n7269/full/nature08482.html.

[55] Jacob F. Sherson, Christof Weitenberg, Manuel Endres, Marc Cheneau, Immanuel Bloch, and Stefan Kuhr. Single-atom-resolved fluorescence imaging of an atomic mott insulator. *Nature*, 467(7311):68–72, September 2010. ISSN 0028-0836. doi: 10.1038/nature09378. URL http://www.nature.com.proxy.lib.umich.edu/nature/journal/v467/n7311/full/nature09378.html.

[56] P. Schauß, M. Cheneau, M. Endres, T. Fukuhara, S. Hild, A. Omran, T. Pohl, C. Gross, S. Kuhr, and I. Bloch. Observation of mesoscopic crystalline structures in a two-dimensional rydberg gas. *arXiv preprint arXiv:1209.0944*, 2012. URL http://arxiv.org/abs/1209.0944.

[57] F. Sorrentino, G. Ferrari, N. Poli, R. Drullinger, and G. M. Tino. Laser cooling and trapping of atomic strontium for ultracold atoms physics, high-precision spectroscopy and quantum sensors. *Modern Physics Letters B*, 20(21):1287–1320, September 2006. ISSN 0217-9849, 1793-6640. doi: 10.1142/S0217984906011682. URL http://www.worldscientific.com/doi/abs/10.1142/S0217984906011682?journalCode=mplb.

[58] P. McQuillen, X. Zhang, T. Strickler, F. B. Dunning, and T. C. Killian. Imaging the evolution of an ultracold strontium rydberg gas. *Physical Review A*, 87(1):013407, January 2013. doi: 10.1103/PhysRevA.87.013407. URL http://link.aps.org/doi/10.1103/PhysRevA.87.013407.

[59] T.C. Killian, T. Pattard, T. Pohl, and J.M. Rost. Ultracold neutral plasmas. *Physics Reports*, 449(4–5):77–130, September 2007. ISSN 0370-1573. doi: 10.1016/j.physrep.2007.04.007. URL http://www.sciencedirect.com/science/article/pii/S0370157307001937.

[60] D. A. Anderson, A. Schwarzkopf, and G. Raithel. Magnetic trapping of circular Rydberg atoms. in preparation, 2013.

[61] Thomas J. Carroll, Katharine Claringbould, Anne Goodsell, M. J. Lim, and Michael W. Noel. Angular dependence of the dipole-dipole interaction in a nearly one-dimensional sample of rydberg atoms. *Physical Review Letters*, 93(15):153001, October 2004. doi: 10.1103/PhysRevLett.93.153001. URL http://link.aps.org.proxy.lib.umich.edu/doi/10.1103/PhysRevLett.93.153001.

[62] Thad G Walker and Mark Saffman. Zeros of Rydberg–Rydberg föster interactions. *Journal of Physics B: Atomic, Molecular and Optical Physics*, 38(2):S309–S319, January 2005. ISSN 0953-4075. doi: 10.1088/0953-4075/38/2/022. URL http://iopscience.iop.org.proxy.lib.umich.edu/0953-4075/38/2/022/.

[63] F Robicheaux. Ionization due to the interaction between two rydberg atoms. *Journal of Physics B: Atomic, Molecular and Optical Physics*, 38(2):S333–S342, January 2005. ISSN 0953-4075. doi: 10.1088/0953-4075/38/2/024. URL http://iopscience.iop.org/0953-4075/38/2/024/.

[64] T. Pohl, E. Demler, and M. D. Lukin. Dynamical crystallization in the dipole blockade of ultracold atoms. *Physical Review Letters*, 104(4):043002, January 2010. doi: 10.1103/PhysRevLett.104.043002. URL http://link.aps.org/doi/10.1103/PhysRevLett.104.043002.

[65] J.D. Jackson. *Classical Electrodynamics*. John Wiley and Sons, 1999.

[66] P.R. Berman and V.S. Malinovsky. *Principles of Laser Spectroscopy and Quantum Optics*. Princeton University Press, 2010. ISBN 9781400837045. URL http://books.google.com/books?id=0gLI5hZRw48C.

[67] Rudolf Grimm, Matthias Weidemüller, and Yurii B. Ovchinnikov. Optical dipole traps for neutral atoms. In Benjamin Bederson and Herbert Walther, editors, *Advances In Atomic, Molecular, and Optical Physics*, volume Volume 42, pages 95–170. Academic Press, 2000. ISBN 1049-250X. URL http://www.sciencedirect.com/science/article/pii/S1049250X0860186X.

[68] S. E. Anderson, K. C. Younge, and G. Raithel. Trapping rydberg atoms in an optical lattice. *Physical Review Letters*, 107(26):263001, December 2011. doi: 10.1103/PhysRevLett.107.263001. URL http://link.aps.org/doi/10.1103/PhysRevLett.107.263001.

[69] Daniel A. Steck. *Rubidium 85 D Line Data*. 2012. available online at http://steck.us/alkalidata (revision 2.1.5, 19 September 2012).

[70] W. M. Haynes, editor. *CRC Handbook of Chemistry and Physics, 92nd Edition (Internet Version 2012)*. CRC Press/Taylor and Francis, Boca Raton, FL, 2012.

[71] M. Marinescu, H. R. Sadeghpour, and A. Dalgarno. Dynamic dipole polarizabilities of rubidium. *Physical Review A*, 49(6):5103–5104, June 1994. doi: 10.1103/PhysRevA.49.5103. URL http://link.aps.org/doi/10.1103/PhysRevA.49.5103.

[72] R M W van Bijnen, S Smit, K A H van Leeuwen, E J D Vredenbregt, and S J J M F Kokkelmans. Adiabatic formation of rydberg crystals with chirped laser pulses. *Journal of Physics B: Atomic, Molecular and Optical Physics*, 44(18):184008, September 2011. ISSN 0953-4075, 1361-6455. doi: 10.1088/0953-4075/44/18/184008. URL http://iopscience.iop.org/0953-4075/44/18/184008.

[73] J Schachenmayer, I Lesanovsky, A Micheli, and A J Daley. Dynamical crystal creation with polar molecules or rydberg atoms in optical lattices. *New Journal of Physics*, 12 (10):103044, October 2010. ISSN 1367-2630. doi: 10.1088/1367-2630/12/10/103044. URL http://iopscience.iop.org/1367-2630/12/10/103044.

[74] Igor Lesanovsky. Many-body spin interactions and the ground state of a dense rydberg lattice gas. *Physical Review Letters*, 106(2):025301, January 2011. doi: 10.1103/PhysRevLett.106.025301. URL http://link.aps.org/doi/10.1103/PhysRevLett.106.025301.

[75] C. S.E. van Ditzhuijzen, A. F. Koenderink, L. D. Noordam, and H.B. van Linden van den Heuvell. Simultaneous position and state measurement of rydberg atoms. *The European Physical Journal D - Atomic, Molecular, Optical and Plasma Physics*, 40(1):13–17, October 2006. ISSN 1434-6060, 1434-6079. doi: 10.1140/epjd/e2006-00140-1. URL http://link.springer.com.proxy.lib.umich.edu/article/10.1140/epjd/e2006-00140-1.